Citation for published version

Cole, Alex J. (2018) Wireless Chipless Liquid Sensing using a Slotted Cylindrical Resonator. Doctor of Philosophy (PhD) thesis, University of Kent,.

DOI

Link to record in KAR

https://kar.kent.ac.uk/71577/

Document Version

UNSPECIFIED

Wireless Chipless Liquid Sensing using a Slotted Cylindrical Resonator

Alex J. Cole

A thesis presented for the degree of
Doctor of Philosophy

School of Engineering & Digital Arts
University of Kent
United Kingdom

May 2018

Declaration

I herewith certify that all material in this dissertation which is not my own work has been properly acknowledged.

Alex J. Cole.

Acknowledgements

The undertaking of a PhD can be a rather isolating experience, particularly during the final brain dump that is this thesis. Having friends, family and colleagues help throughout is invaluable, and perhaps an absolute necessity.

To Cody, who kept me grounded and anchored to the real world, but still humoured me during my nonsensical, work-related rants. I only hope that I can repay you going forward, presumably by offering unrelatable and subject-specific advice which is of no use to you or your work, but will make me feel better nonetheless.

To my parents, grandparents and family, for always pushing me to do my best, never with any expectation of particular marks or grades. You instilled in me a desire to always try and understand what I was learning, not selectively extract information in order to pass exams. I should probably mention something about financial support here, but I will avoid it in case you end up paying for the copy you are reading now. I simply could not handle the sarcastic remarks.

To my supervisor, for allowing me creative freedom to pretty much pursue my work at my own pace and in whichever direction I saw fit, while still offering much needed words of wisdom. To Richard, for words of encouragement which you may not have even known you were giving, and the numerous coffee breaks filled with stories around the sheer madness of academia. A special thanks to Simon for the mind-numbing soldering of a great number of sensors, where your skills could have perhaps been utilised in more useful ways. Though it may have seemed minor amongst your workload, your time and effort was invaluable to me.

One final note goes to my brother, Jason. I feel I have met many brilliant minds throughout my education, but not one quite as brilliant as yours. Though I could never hope to reach your level, you have consistently provided me with a source of motivation and a sense of what is possible, for which I will always be grateful. [1]

Oh, and thank you copper-clad Mylar® film. It would have been literally impossible without you.

---

[1] That and teaching me integration by parts back when I was in sixth form, C4 was tough.

Abstract

This thesis presents a comprehensive study on the application of a slotted cylindrical resonator for the wireless assessment of liquids. Using simple geometry and measurement techniques, a method for the sensing of liquids within non-metal pipes is established, allowing for the prospect of non-contact, real-time, wireless monitoring of industrial liquid processes with no requirement for samples. The main contribution of this work is the development of a thorough understanding of the geometry, as well as an extensive presentation of measured data using liquids of wide-ranging properties. A full parametric and sensitivity study obtained through theory, simulation and measurement provides analysis on every aspect of the proposed sensor, including a number of potential future research topics. The slotted cylinder is placed directly on-pipe, requiring no additional circuitry, power or support structure, and is excited wirelessly by an external antenna. Its resonant frequency is very sensitive to the permittivity within the sensor cavity, and is shown to operate well across a relatively large range of ε_r. The structure is highly adaptable, even for fixed pipe dimensions, and simple adjustments provide a method for the tuning of resonant frequency and sensitivity control. Additionally, the placement of multiple sensors in close proximity allows for the measurement of high-loss liquids, which may otherwise not be possible. A number of measurement techniques for level sensing are presented, covering both frequency and amplitude detection methods using single and multiple sensors, where the geometry is shown to be highly sensitive to very small changes in liquid level. Measurements detecting relatively small changes in liquid temperature provide a further potential application of the sensor. The simultaneous monitoring of multiple liquids is easily achieved using a single measurement system, vastly reducing the complexity inherent in large-scale industrial processes. The sensor is shown to be resilient to changes in polarisation and position relative to the measurement antenna, as well larger read distances compared with other passive sensors.

List of Abbreviations

Ae	Effective Aperture
CST	Computer Simulation Technology
DAK	Dielectric Assessment Kit
DUT	Device Under Test
LED	Light-Emitting Diode
LoS	Line of Sight
LP	Log-Periodic
LUT	Liquid(s) Under Test
MWS	Microwave Studio
PEC	Perfect Electric Conductor
PTFE	Polytetrafluoroethylene
RFID	Radio Frequency Identification
RCS	Radar Cross-Section
SG	Savitzky-Golay
SIW	Substrate-Integrated Waveguide
SNR	Signal-to-Noise Ratio
SRR	Split-Ring Resonator
VNA	Vector Network Analyser

List of Terms

a	Metal Thickness
d	Pipe Wall Width
ε'	Real Part of the Permittivity
ε''	Imaginary Part of the Permittivity
ε_0	Free-Space Permittivity
ε_p	Pipe Permittivity
ε_r	Liquid Permittivity
r	Radius
SL	Slot Length
SW	Slot Width

Contents

1 Introduction **1**
  1.1 A Brief Review of Sensors 1
  1.2 Liquid Sensing 2
  1.3 Background Theory 4
    1.3.1 Permittivity 5
    1.3.2 Effect of Permittivity on Wavelength 10
    1.3.3 Resonance 12
  1.4 Literature Review 16
  1.5 Aims and Objectives 25
  1.6 Thesis Outline 27

2 Theory & Simulation **28**
  2.1 Sensor Introduction and Scope 28
  2.2 Theory 38
    2.2.1 General Discussion 38
    2.2.2 Theoretical Model 39
    2.2.3 Limitations 44
  2.3 Device Simulation 47
    2.3.1 Simulation Overview 48
    2.3.2 Parametric Study 54
  2.4 Conclusion 69

3 Experimental Results **71**
  3.1 Liquids Under Test 71
  3.2 Fabrication 76
  3.3 Experimental Environment and Methodology 80
    3.3.1 Measurement Method 80
    3.3.2 Antenna Separation 87
    3.3.3 Sensor Rotation 90

3.3.4 Sensor Vertical Position 91
3.3.5 Antenna Polarisation 93
3.4 Noisy Data Processing 95
3.5 Verification of Simulated Results 98
3.6 Liquid Measurements 105
3.7 Multiple Sensor Measurements 113
3.7.1 Effect of Coupling 113
3.7.2 SNR Improvement 116
3.7.3 Simultaneous Measurement 119
3.8 Measurement Accuracy 121
3.9 Conclusion 122

4 Further Applications 125
4.1 Use of Geometry as a Level Sensor 125
4.1.1 Single Sensor 127
4.1.2 Multiple Sensor 138
4.2 Temperature Sensing 145
4.3 Conclusion 150

5 Conclusion & Future Work 153
5.1 Future Work 157

Research Contributions

A. J. Cole, C. C. H. Ng, F. A. Almalki and P. R. Young, “Chipless RF liquid sensor,” *2015 IEEE MTT-S International Microwave and RF Conference (IMaRC)*, Hyderabad, 2015, pp. 243-245.

S. Swaisaenyakorn, A. J. Cole, C. C. H. Ng and P. R. Young, “Conformal switched beam antenna,” *2016 Loughborough Antennas & Propagation Conference (LAPC)*, Loughborough, 2016, pp. 1-4.

A. J. Cole and P. R. Young, “Chipless liquid sensing using a slotted cylindrical resonator,” *IEEE Sensors Journal*, vol. 18, no. 1, pp. 149-156, Jan, 2018.

A. J. Cole, R. J. Collier and P. R. Young, “Variation of the attenuation constant in the presence of standing waves.” *IEEE Microwave and Wireless Components Letters*, vol. 28, no. 8, pp. 639-641, Jul, 2018

A. J. Cole and P. R. Young, “Non-contact wireless level sensing of pipe contents using a cylindrical split-ring resonator.” In preparation for Microwave Theory and Technique.

Chapter 1

Introduction

1.1 A Brief Review of Sensors

A sensor can be thought of as any device which measures some physical property of the world around us and converts it into a signal which may then be interpreted. The Oxford English Dictionary defines a sensor as [1]:

> A device which detects or measures a physical property and records, indicates, or otherwise responds to it.

The sensing device itself is usually used in conjunction with other electronics which convert the signal into some meaningful format, and it is not uncommon to refer to this resultant system as a sensor. For example, a thermistor changes its resistance based on the temperature of its environment, and this change can be used to light a row of LEDs which correspond to certain temperature intervals. The thermistor is the actual sensing device and the LED circuitry only acts to interpret the signal to provide a meaningful, graphical output, but we may well refer to the entire system as a temperature sensor. Sensor technology has progressed immensely during the past few decades, with emerging fields such as Radio Frequency Identification (RFID) receiving large amounts of interest from academics and industry. Devices can range from the very simple, such as the example of the temperature sensor, to the very complex, where any number of sensing devices are used in combination with powerful central processing units.

Sensors are broadly categorised into two types, passive and active. Passive sensors are capable of providing some form of electronic feedback from an external stimulus without the need for additional circuitry or power. A reflective microwave device, commonly referred to as a tag in sensing terminology, may receive an incoming wave of a certain amplitude and frequency from an interrogative antenna. Based on any number of physical properties around the tag, such as temperature or humidity, the reflected waveform may be modulated in some way, whether in frequency, amplitude or both. Based on the modulation of the reflected wave, the physical property under consideration can be determined by a separate processing device, such as a computer. In this case the system as a whole is clearly not passive, where any sensory operation will require some form of stimulus, but the sensing tag itself does not require power to modulate the incoming wave, and is therefore a passive sensor. For active sensors, as the term implies, this is not the case. This class of sensor requires a power source to operate, the example of the strain gauge is often used to describe a basic active sensing device. The strain gauge sensor features a number of long and thin metal tracks printed onto a flexible substrate and connected to a power source. As the substrate deforms, bending up or down, the resistance of the tracks changes and causes a change in the measured voltage, from which the applied force may be determined.

Both types of sensor operate with the same principle, that a change in their environment or structure should result in a measurable change in the sensor response. The magnitude of the change in the sensor's response relative to the change in the property under consideration provides an indication of the sensitivity of the sensor. A sensor designed to detect temperature over a relatively small range would be expected to be highly sensitive to small variations, whereas the opposite may be true of a sensor intended to detect very large changes in temperature.

1.2 Liquid Sensing

Sensors appear in almost every aspect of modern life, from motion detectors to weight sensors at supermarket checkouts, and it would be impossible to list every application here. However, this thesis only considers a particular subset of sensors, those that detect and measure or characterise liquids and their related properties, such as permittivity, temperature and level or volume. Liquid monitoring is a useful tool for quality control in many industrial environments, including chemical plants, oil refineries and waste water treatment. A number of sensors may be deployed with each monitoring a different process or liquid property, where the resulting group of sensors could be connected to the internet, or bespoke network, to provide a holistic view of an active industrial environment. Sensor networks have received a large amount of attention in recent years, and can be considered as part of the

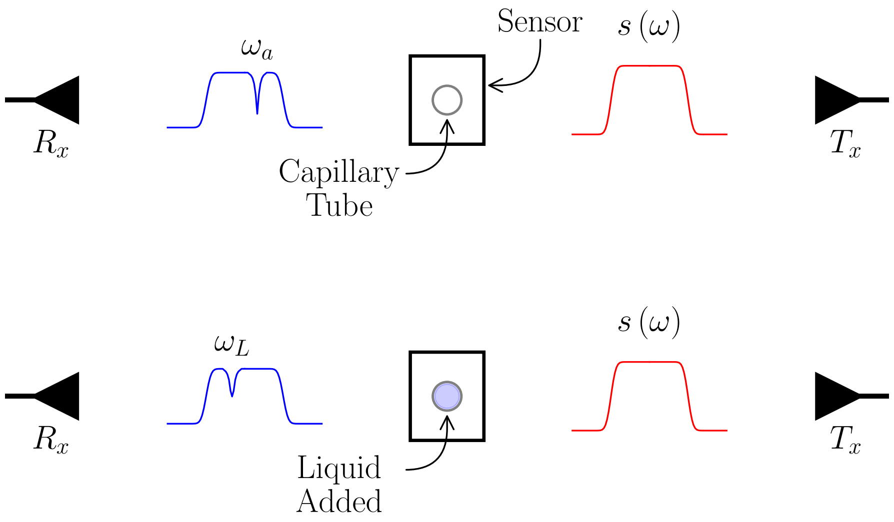

Figure 1.1: Example of a simplified sensing environment.

wider progress towards the internet of things [2][3][4]. The study of liquid sensing methods is highly important for areas of industry and can highlight new sensors potentially capable of improving accuracy or precision, reducing cost and complexity and increasing reliability and robustness.

Liquid sensors generally operate under the same principle, that their performance or behaviour is altered in the presence of a liquid in a way which is measurable and proportional to a property of that liquid. The performance or behaviour of a sensor may refer to an operating frequency, amplitude or bandwidth response, for example. A generic sensor can be seen in Fig. 1.1, where liquid samples are added *via* the capillary tube shown in its centre. The top diagram shows no liquid present, where the broadband transmitted signal $s(\omega)$ of amplitude A_0, over its operating bandwidth, is received by the sensor. The generic sensor pictured here resonates at a particular frequency, and effectively behaves as a bandstop filter, resulting in attenuation or scattering at a frequency equal to ω_a, with the resulting signal travelling away from the sensor towards the receiving antenna, where the subscript a denotes an air-filled capillary tube. The amplitude of the transmitted signal is reduced, due path loss and the losses present in the sensor, where any good sensor should keep this loss to a minimum, as well as from reflections directed away from R_x. The lower diagram in Fig. 1.1 shows the behaviour of the sensor when a liquid sample is added to the tube. The sensor now resonates at a lower frequency of ω_L, where the subscript L denotes a liquid-filled tube. Generally, the signal attenuated by the sensor will not consist of one single frequency, but will be of a certain bandwidth

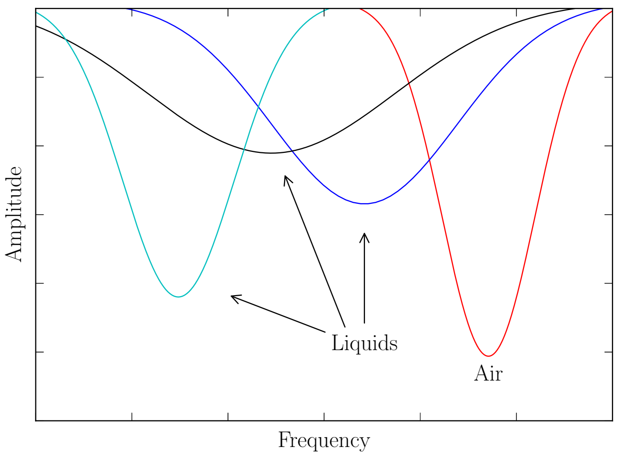

Figure 1.2: Example of results from the sensor shown in Fig. 1.1.

determined by the properties of the sensor and liquid under test (LUT).

By adding a number of different liquids to the capillary tube, we can obtain a set of results describing the amplitude and frequency of the transmitted signals seen at the receiving antenna. For each liquid, we may plot the measured amplitude as a function of frequency, as shown by Fig. 1.2, where the air and liquid results are labelled. The minimum amplitude for each measurement determines the *resonant frequency* f_r of the sensor, and along with the amplitude at f_r we are able to associate sensor results with specific liquids. For example, the minimum amplitudes of the results in Fig. 1.2 may be used to describe the amount of attenuation caused by each LUT. If the sensor is being used to measure an unknown liquid, the minimum amplitude can be compared against known values to determine which liquid is present. Alternatively, the resonant frequency of a measurement could be used to assess the permittivity of the LUT in a similar manner. Both attenuation, worsened by dielectric losses, and permittivity will be discussed in a later section. It should be noted that the sensor and indeed the measurement method shown in Fig. 1.1 are intended as examples only, where there is no requirement to incorporate sensors into strictly wireless systems, although this method will feature heavily throughout this thesis.

1.3 Background Theory

Before undertaking a review of the relevant literature regarding liquid sensors and liquid measurement methods, it is necessary to introduce some of the fundamental theory and concepts which form the foundations of the design and operation of liquid sensors.

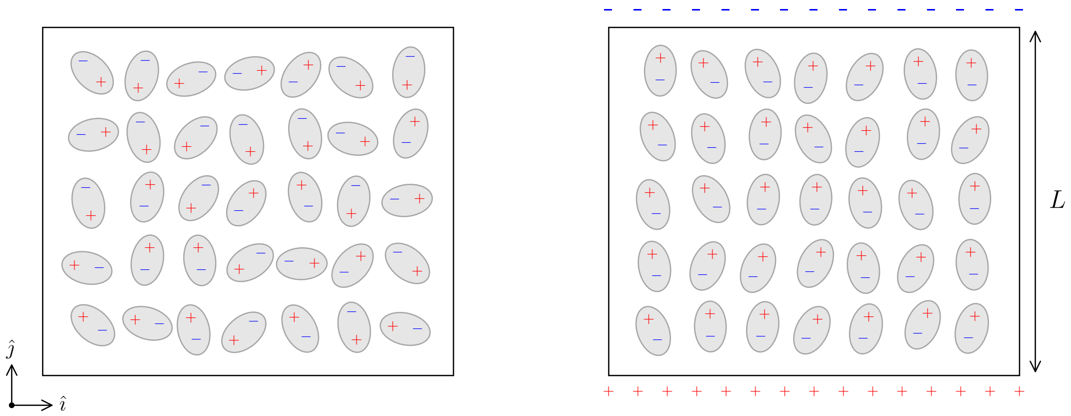

(a) No external field.

(b) External field applied.

Figure 1.3: Diagram of the polarisation of dipoles in the presence of an external electric field.

1.3.1 Permittivity

A vast majority of sensors rely strictly on the electrical properties of materials in order to measure or characterise them, particularly important is the permittivity ε of a medium. Dielectric materials generally consist of charged molecules or particles which have an associated dipole moment. In the absence of any significant external electric field, the dipoles will be effectively randomly orientated throughout the material, as shown in Fig. 1.3a. Once an external electric field is applied, the dipoles act to orientate themselves accordingly, where Fig. 1.3b displays the alignment of dipoles with the external field. It can be seen that the charges cancel within the dielectric, but a net surface charge ρ_s now exists at its boundaries which opposes the external field.

Permittivity provides a measure of how strongly a dielectric or medium resists an external field as a result of the polarisation of its constituent dipoles. In the absence of media there exists a free-space, or vacuum, permittivity, which is defined as:

$$\varepsilon_0 \triangleq \frac{1}{c_0^2\,\mu_0} \approx 8.854 \times 10^{-12} \qquad [\mathrm{F\,m^{-1}}] \qquad (1.1)$$

where c_0 is the speed of light in a vacuum and $\mu_0 \approx 4\pi \times 10^{-7}$ $\mathrm{H\,m^{-1}}$ is the permeability of free-space. All dielectric materials will have a permittivity greater than ε_0 due to the increased resistance to external electric fields caused by the presence of media, as shown in Fig. 1.3b. Generally, permittivity is referred to as a dimensionless value relative to ε_0 to avoid unnecessary confusion, where the absolute permittivity of a dielectric is equal to:

$$\varepsilon = \varepsilon_r \varepsilon_0 \tag{1.2}$$

The term ε_r provides for useful comparison of different media without resorting to impractically small numbers. The absolute permittivity of air is, for most practical purposes, equal to ε_0, where $\varepsilon_r \approx 1.0006$. The relative permittivity values of some common materials are listed in Table 1.1. It should be noted that the permittivity of a medium is not a constant, indeed, it can vary greatly with frequency or temperature and, for some inhomogeneous, anisotropic, time-variant or non-linear materials, with location, direction, time or amplitude. If a material consists of uniform properties throughout its structure, it is said to be *homogeneous*, that it is to say, it does not contain any volumes or pockets of differing media and so its properties do not depend on location. A material which is *isotropic* features the same properties in every direction for travelling waves, which is not true for some types of crystal. Should a material consist of changing properties over time, it is said to be *time-variant*, potentially caused by passing sound waves through it [5], for example. Finally, a medium is said to be *linear* if the ratio of its polarisation to an applied electric field does not depend on amplitude.

Table 1.1: Relative permittivity ε_r of some common materials [6].

Material	ε_r
Air	1.0006
Polystyrene	2.7
Nylon (solid)	3.8
Quartz	5
Marble	8
Germanium	16
Glycerin	50
Water (distilled)	81

The polarisation density P of a medium describes the density of induced dipole moments such as those depicted in Fig. 1.3b, and is equal to [7]:

$$\mathbf{P} = \frac{nqL}{v}\,\hat{\jmath} \qquad [\mathrm{C\,m^{-2}}] \tag{1.3}$$

where n and q refer to the total number of dipoles and their charge, respectively, L is the distance between the induced surface charges shown in Fig. 1.3b and v is the total dielectric volume. The unit vector $\hat{\jmath}$ is in the direction of polarisation. The polarised medium gives rise to the displacement field D defined as [8]:

$$\mathbf{D} = \varepsilon_0 \mathbf{E} + \mathbf{P} \tag{1.4}$$

For a homogeneous, isotropic and linear material:

$$\mathbf{P} = \varepsilon_0 \chi \mathbf{E} \tag{1.5}$$

where χ is the constant of proportionality, known as the electric susceptibility of a medium. A greater value of χ results in greater polarisation in response to an external electric field. Susceptibility is related to permittivity as $\chi = \varepsilon_r - 1$, where Eq. 1.4 now becomes:

$$\begin{aligned} \mathbf{D} &= \varepsilon_0 \mathbf{E} + \varepsilon_0 \chi \mathbf{E} \\ &= \varepsilon_0 \mathbf{E} \left(1 + \chi\right) \\ &= \varepsilon_0 \varepsilon_r \mathbf{E} \end{aligned} \tag{1.6}$$

As the relationship between an applied electric field and dielectric polarisation is causal, there is a finite delay between the applied field $\mathbf{E}$ and the displacement field $\mathbf{D}$. For low frequencies, the phase delay δ between $\mathbf{E}$ and $\mathbf{D}$ will be effectively 0, where the time taken τ for dipoles in a material to polarise will be much smaller than the period T of the applied electric field. Conversely, as the frequency increases we find τ becomes similar in value to T and δ becomes larger, this is shown graphically in Fig. 1.4. This increasing phase delay has two implications for a dielectric material. Firstly, if dipoles within the medium are not polarising quickly relative to the frequency of the external electric field, the surface charge ρ_s which acts to oppose $\mathbf{E}$ begins to lag and does not resist $\mathbf{E}$ as strongly as when $\delta = 0$. Secondly, if polarisation is taking more time per wave cycle, the dipole movement will produce a greater amount of heat, which results in dielectric loss. Permittivity can conveniently take both issues into consideration by making it a complex value, consisting of a real and imaginary part, where:

$$\varepsilon = \varepsilon' - j\varepsilon'' \tag{1.7}$$

and for a relative permittivity:

$$\varepsilon_r = \varepsilon_r' - j\varepsilon_r'' \tag{1.8}$$

The real part is more commonly used to describe materials, and describes the

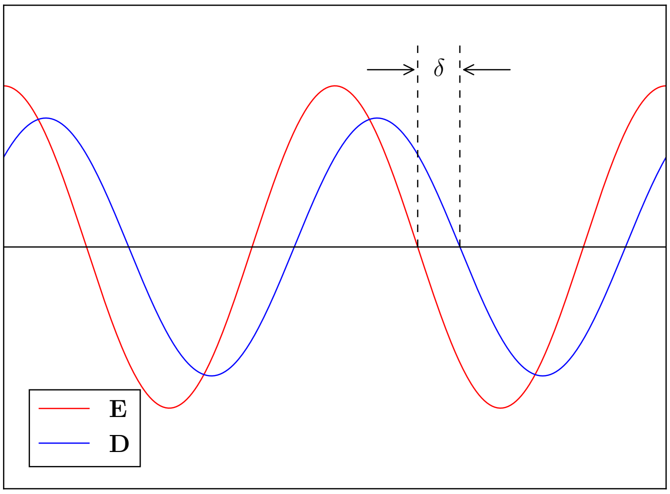

Figure 1.4: Phase delay between applied field **E** and displacement field **D**.

lossless behaviour of a dielectric in the presence of an applied external field. The imaginary part of the permittivity, also known as the dielectric loss factor, appears in Maxwell's curl equation for the magnetic field [9]:

$$\begin{aligned} \nabla \times \mathbf{H} &= \frac{\partial \mathbf{D}}{\partial t} + \mathbf{J} \\ \nabla \times \mathbf{H} &= j\omega \left(\varepsilon' - j\varepsilon'' - j\frac{\sigma}{\omega} \right) \mathbf{E} \end{aligned} \tag{1.9}$$

where the current density $\mathbf{J} = \sigma \mathbf{E}$, and Eq. 1.9 assumes a time dependence $e^{j\omega t}$ and time-invariant permittivity. The dielectric loss factor is used in combination with ε' and conductivity σ to define the loss tangent of a material as:

$$\tan \delta = \frac{\omega\varepsilon'' + \sigma}{\omega\varepsilon'} \tag{1.10}$$

It can be seen that the dielectric loss term $j\varepsilon''$ is indistinguishable from the conductive loss $j\frac{\sigma}{\omega}$ in Eq. 1.9, and results in a simpler definition of the loss tangent of a material by combining ε'' and σ:

$$\tan \delta = \frac{\varepsilon''}{\varepsilon'} \tag{1.11}$$

where the conduction losses would be very low in good insulators. The loss tangent defined in Eq. 1.11 is regularly used to describe a dielectric material, where data sheets will reference values for ε_r and $\tan \delta$, often at specific frequencies. A higher loss tangent generally describes increased attenuation within a medium, where

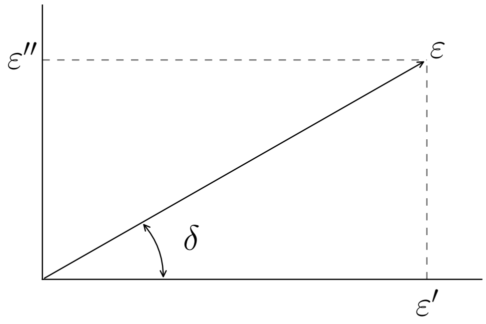

Figure 1.5: Graphical depiction of the relationship between complex permittivity and loss tangent.

a good dielectric would be expected to have a low $\tan\delta$, and *vice versa*. A graphical relationship between complex permittivity and the loss tangent can be seen in Fig. 1.5. In scenarios where we are considering an inhomogeneous region, or one which contains more than one material, it can be beneficial to define an *effective* permittivity ε_e which describes an equivalent, homogeneous region. In simple cases involving two dielectrics ε_e may simply be calculated as the volume average of the two permittivity values, often providing a good approximation. Some well-known expressions [10] are used to approximate an equivalent dielectric region surrounding microstrip lines, for which field lines exist in a substrate below the line and in air above it.

For materials that are homogeneous, isotropic, linear and time-invariant the permittivity is a greatly simplified physical property, but one which still varies, sometimes considerably, with frequency and temperature. The frequency of the applied external field, of period T, is related to the phase delay δ displayed in Fig. 1.4, and the temperature of a material directly impacts the mobility of its constituent dipoles. An example of a permittivity measurement of ethanol (discussed later in this thesis), shown in Fig. 1.6, displays the behaviour of the real and imaginary parts of ε_r against frequency. The real part is shown to decrease with increasing frequency, as T decreases relative to the polarisation time τ and the alcohol provides less resistance to the external field. The dielectric loss reaches a maximum at around 0.8 GHz, the frequency at which ethanol is dissipating the most amount of energy due to dipole movement, before falling in a similar manner to ε_r'. At high microwave frequencies ε_r' will become relatively constant, often referred to as ε_∞, though at even higher optical frequencies materials will exhibit more complicated behaviour.

It is interesting to note that dielectric loss is used advantageously in microwave ovens, which operate at a frequency, 2.45 GHz. The molecules of water within food produce heat as a result of the dipole movement at this frequency and consequently

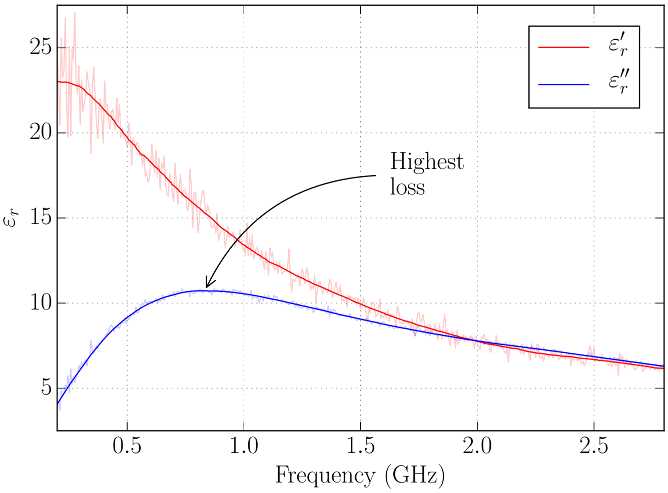

Figure 1.6: Example measurement of the permittivity of ethanol.

warm the food. Using the model presented in [11], Fig. 1.7 shows the complex permittivity of water from 1 to 100 GHz and for varying temperature. The model suggests that maximum heat would be produced at frequencies above 10 GHz, but this would cause much greater attenuation in the outer layers of food rather than heating throughout as is the case at 2.45 GHz, a frequency which exists within the unlicensed $2.4 - 2.5$ GHz ISM band. We also see from Fig. 1.7 the effect of temperature, where the model was used to generate curves for 0 to 30°C for both parts of the permittivity. For lower frequencies the real part decreases as temperature rises, but this trend is reversed as we move towards higher frequencies. Additionally, the peak in the dielectric loss appears to increase in frequency and slightly reduce in amplitude as temperature rises. This is perhaps explained by a reduction in the viscosity of water as temperature rises, allowing greater free-movement of dipoles and therefore a reduced τ. Fig. 1.7 provides some insight into the potentially complicated nature of determining the permittivity of a material, even for those that are homogeneous, isotropic, linear and time-invariant. The widespread usage of the term *dielectric constant*, which refers to the real part of the permittivity, could be considered as a misnomer in this regard. However, for most polymers the permittivity is seen to be considerably more stable over relatively large frequency and temperature ranges, and over practical bandwidths the permittivity may well be near-constant.

1.3.2 Effect of Permittivity on Wavelength

The definition of vacuum permittivity ε_0 from Eq. 1.1 arises from the definition of the speed of light in a vacuum:

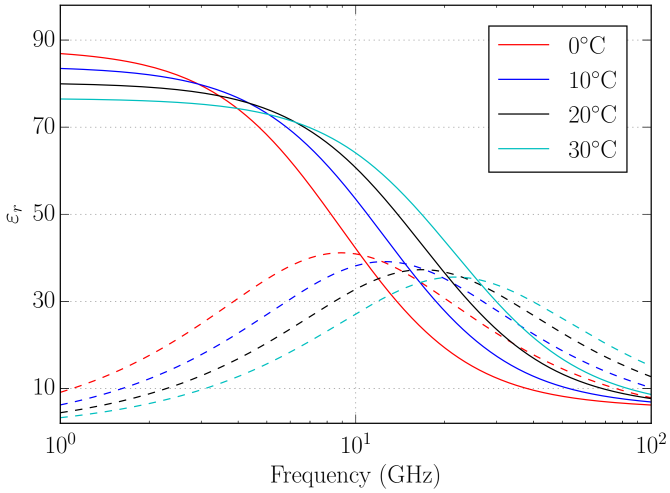

Figure 1.7: Modelled complex permittivity of water [11], showing the real (solid) and imaginary (dashed) parts.

$$c_0 \triangleq \frac{1}{\sqrt{\varepsilon_0 \mu_0}} \qquad [\mathrm{m\,s^{-1}}] \tag{1.12}$$

By generalising for all media we obtain:

$$c \triangleq \frac{1}{\sqrt{\varepsilon\mu}} = \frac{1}{\sqrt{\varepsilon_0\,\varepsilon_r\,\mu_0\,\mu_r}} = \frac{c_0}{\sqrt{\varepsilon_r\mu_r}} \tag{1.13}$$

From Eq. 1.13 it is seen that the speed of light, or any electromagnetic wave, is decreased by a factor of $1/\sqrt{\varepsilon_r}$ when travelling through a medium. Dielectric materials generally have the same magnetic properties as free-space, where $\mu_r \approx 1$, and so the term can be ignored in Eq. 1.13. From the definition of wavelength, we see that it decreases with c:

$$\lambda = \frac{c}{f} = \frac{c_0}{f\sqrt{\varepsilon_r}} \tag{1.14}$$

The value of f in Eq. 1.14 is a constant, and so for a given frequency we see a reduction in wavelength of $1/\sqrt{\varepsilon_r}$ when a wave travels through media. For a dielectric of $\varepsilon_r = 9$, as an example, the wavelength will be a third of that in free-space. This has practical consequences in structures which are sensitive to wavelengths, such as the rectangular waveguide shown in Fig. 1.8. The wide dimension a determines the cut-off frequency f_c of the waveguide, which specifies the lowest frequency at which waves will propagate, where [12]:

$$f_c = \frac{c}{2a} \tag{1.15}$$

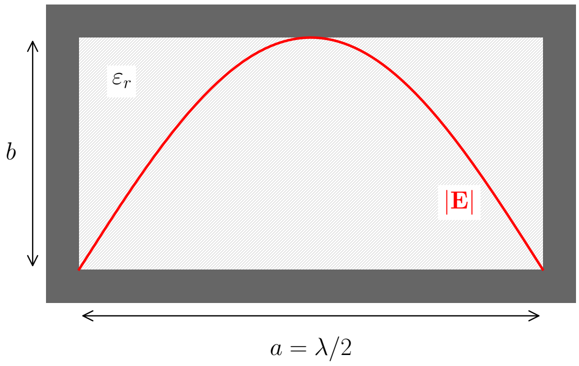

Figure 1.8: Cross-section of a rectangular waveguide.

for the commonly used TE_{10} mode in an air-filled waveguide, the electric field magnitude of which is displayed in Fig. 1.8.

However, if the waveguide is now filled with a dielectric as shown in the diagram, the wavelength will be reduced in accordance with Eq. 1.14. So for a given rectangular waveguide geometry, the presence of a dielectric will reduce the wavelength and therefore *decrease* the cut-off frequency f_c. Alternatively, higher values of ε_r may be used to reduce the necessary waveguide size required for the desired f_c. The required waveguide dimension $a = \lambda/2$ for a number of desired cut-off frequencies is shown in Fig. 1.8, where the miniaturisation of the structure with increasing ε_r is clearly seen.

This type of miniaturisation is widely used to reduce the overall size of microwave devices and antennas for various reasons, with the trend of smaller electronics placing ever-more stringent requirements on product dimensions. Miniaturisation is not necessarily endless where there do exist some fundamental limits on the size of devices, a study on electrically small antennas can be found in [13]. Within the scope of this thesis, it is the reduction in operating frequency caused by the presence of a dielectric of ε_r that is of specific interest. Resonant waveguide cavities form much of the literature on liquid sensing, and the expected values of ε_r are very important in determining the cavity dimensions. The generic sensor shown in Fig. 1.1 produced minima at different frequencies for different liquids, displayed in Fig. 1.2, and it is the identification of these resonant frequencies that form the basis of much of the work in this thesis.

1.3.3 Resonance

In general terms, resonance can be thought of as the frequency, or band of frequencies, at which a system oscillates with a maximum amplitude or produces the greatest

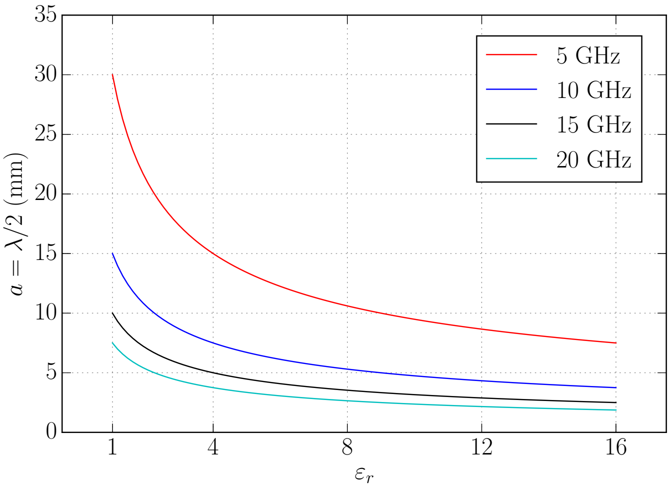

Figure 1.9: Reduction in size of rectangular waveguide as ε_r increases.

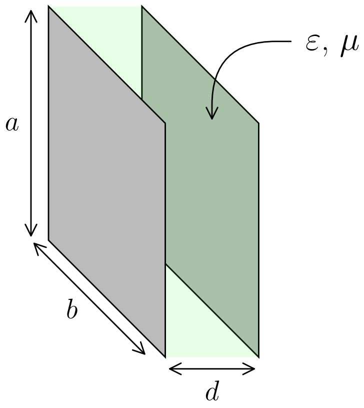

(a) Parallel plate resonator.

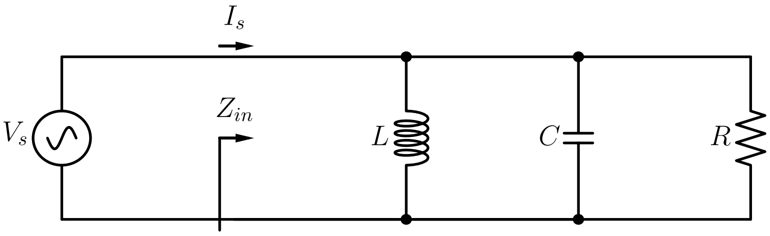

(b) Parallel RLC circuit.

Figure 1.10: Parallel plate resonator and equivalent circuit.

output for a given input. A simple example of this is a person being pushed on a swing, where one can observe a speed at which the swing oscillates with very little input, and this oscillation can be thought of as the resonant frequency of the swing, sometimes referred to as the natural frequency. In electronics terms, consider the dielectric filled parallel plate resonator shown in Fig. 1.10a and its equivalent RLC circuit shown in Fig. 1.10b. The capacitance and inductance are given as $C = \varepsilon ab/d$ and $L = \mu bd/a$, respectively, and the resistor may represent losses within the dielectric. For an ideal inductor and capacitor there is no resistance, and their impedance is purely reactive [14][15]:

$$X_L = 2\pi f L = j\omega L \tag{1.16}$$

$$X_C = \frac{1}{2\pi f C} = \frac{1}{j\omega C} \tag{1.17}$$

where $\omega = 2\pi f$ is the angular frequency. With reference to Eqs. 1.16 and 1.17 we see that the capacitive reactance decreases with frequency, and *vice versa* for the inductive reactance. At a certain frequency the inductive and capacitive reactance will be equal, and so currents flowing through each component will be equal in magnitude but 180° out of phase, thus cancelling. In reality however, there will always exist some energy loss, such as winding resistance in the inductor. The frequency where $X_L = X_C$ is known as the *resonant* frequency f_r of the circuit, and is the point at which the maximum amount of energy is stored, hence the term *tank* circuit often applied to circuits such as in Fig. 1.10b. For arbitrary values of R, L and C, the magnitude of the input impedance is plotted against normalised frequency in Fig. 1.11, showing the resonant frequency and the associated resonant impedance magnitude $|Z_r|$, where for a parallel RLC circuit [16]:

$$Z_{in} = \left(\frac{1}{R} + \frac{1}{j\omega L} + j\omega C \right)^{-1} \tag{1.18}$$

Given the resonance condition $X_L = X_C$, the magnitude of Z_{in} becomes exclusively real, where, using admittance $Y = 1/Z$ for clarity:

$$\begin{aligned} |Y_r| &= \sqrt{\left(\frac{1}{R}\right)^2 + \left(\frac{1}{X_L} - \frac{1}{X_C}\right)^2} = \frac{1}{R} \\ |Z_r| &= R \end{aligned} \tag{1.19}$$

Hence the maximum impedance Z_r observed at resonance is equal to the purely

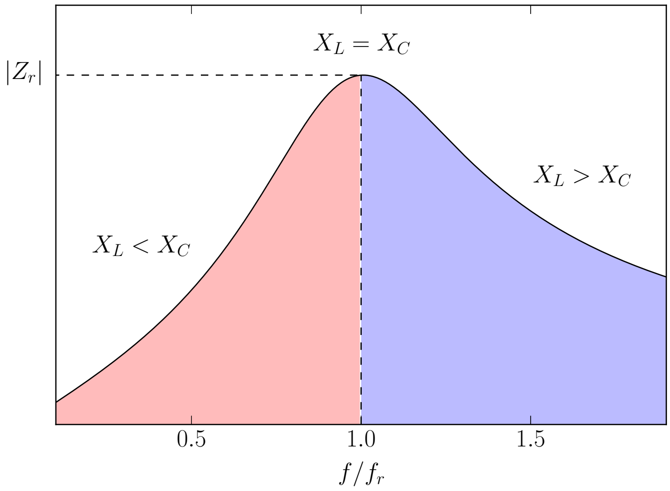

Figure 1.11: The input impedance Z_{in} of the circuit shown in Fig. 1.10b.

real value of the shunt resistor shown in Fig. 1.10b.

The frequency selectivity of a resonant circuit can be qualified through a measure of the sharpness of the response, where a narrow peak displays higher frequency selectivity than a wide peak. For different values of the resistance of R, Fig. 1.12 displays the magnitude of the input impedance. Initial qualitative assessment shows that an increase in R results in a significantly sharper impedance curve, both narrower and taller. The bandwidths Δf_{3dB} refer to the range of frequencies for which $|Z_{in}| > Z_r/\sqrt{2}$, or where the input impedance is a factor of $\sqrt{2}$ below the resonant value. Therefore the damping effect of the resistor can be qualified by an assessment of the Q-factor, which can be defined in terms of a frequency-to-bandwidth ratio as:

$$Q = \frac{f_r}{\Delta f_{3dB}} \tag{1.20}$$

Fig. 1.12 shows an increase in the Q-factor with the resistance of R, which agrees with definitions of the unloaded Q-factor of parallel resonant circuits:

$$Q_0 = \frac{R}{\omega_r L} = \omega_r RC \tag{1.21}$$

Series resonant RLC circuits, from basic circuit theory, result in the inverse of Eq. 1.21 where:

$$Z_{in} = R + j\omega L + \frac{1}{j\omega C} \tag{1.22}$$

$$Q_0 = \frac{\omega_r L}{R} = \frac{1}{\omega_r RC} \tag{1.23}$$

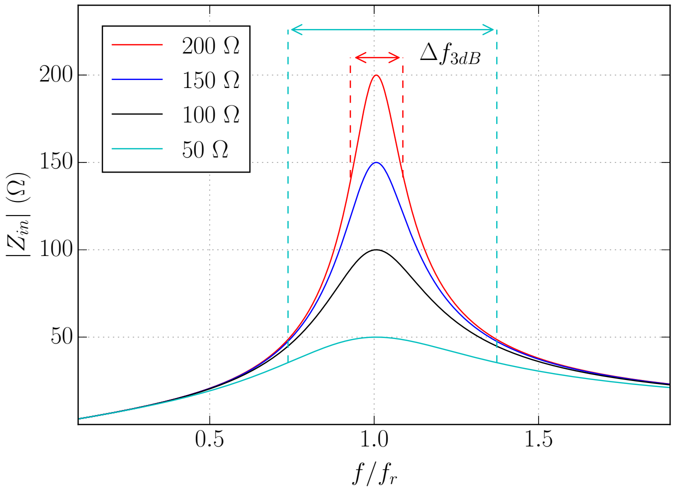

Figure 1.12: Result of changing R in Fig. 1.10b.

The unloaded Q-factor Q_0 refers to behaviour of a resonator without external loading effects. The results given by Eqs. 1.21 and 1.23 arise from the general definition of the Q-factor:

$$Q = \omega \frac{\text{average energy stored}}{\text{energy loss per second}} \tag{1.24}$$

The inverse relationship between Q and energy loss has potential implications for liquid sensing, where higher dielectric losses ε'' may reduce the Q-factor of a sensor response. A resonator, or indeed sensor, whose response displays a high Q-factor may be said to be high-Q, and *vice versa*.

Finally, by equating Eqs. 1.16 and 1.17 as is the case at resonance, and rearranging for f, we obtain the resonant frequency of an LC circuit, where:

$$f_r = \frac{1}{2\pi\sqrt{LC}} \qquad \omega_r = \frac{1}{\sqrt{LC}} \tag{1.25}$$

which is valid for any resonant circuit for which the overall inductance and capacitance are known.

1.4 Literature Review

This section aims to discuss relevant research related to the scope of this thesis. Although a complete, comprehensive study of the literature is not necessarily possible, the work presented here intends to provide insight into relatively recent contributions to the field of liquid sensing, as well as some established methods. The majority of literature focuses on either reflectometric methods which are concerned with the analysis of S_{11}, transmission methods which assess S_{21}, or resonance methods which generally detect changes in the Q-factor. A review of RF and microwave techniques for liquid sensing can be found in [17].

Standard Methods

There exists a number of established methods for the accurate characterisation of the complex permittivity of materials, each with its own advantages and disadvantages. One of the simpler methods at lower frequencies, generally below 1 GHz, is the admittance cell, which in its simplest form consists of two parallel-plate electrodes. The structure may be measured in free-space and when completely immersed in a liquid, resulting in two admittance measurements Y_0 and Y_L, referring to a free-space and liquid admittance, respectively. For a three-terminal admittance cell with guard electrodes Y is given by [18]:

$$Y = j\omega \frac{\varepsilon_0 \varepsilon A}{d} \tag{1.26}$$

where ε is the complex permittivity of the measured liquid, A is the area of either electrode and d is the distance between them. It is then simply a case of dividing Y_L by Y_0 to calculate ε. Another common method is the open-ended, or flared, coaxial probe. This measurement technique makes use of fringing fields which occur at the end of a coaxial probe, as illustrated in Fig. 1.13a, where the lines shown are not intended to be representative of the actual electric field distribution. The reflection coefficient, measured by a VNA or similar, is a function of the permittivity of the LUT and is used to estimate ε. The example shown features a flange which improves the accuracy of analytical models used to describe the behaviour of the probe, and therefore the permittivity calculation. The dielectric 'plug' is positioned at the end of the coaxial line to allow for complete immersion in the LUT. Measurements of liquids using this method typically rely on a calibration process which requires measurements of an open and short-circuit, and of a reference liquid such as distilled water. An example of the use of a flared open-ended coaxial probe liquid measurement is shown in Fig. 1.13b, where this experimental configuration is almost identical to the one used to measure liquids in section 3.1.

In structures that are highly resonant, the introduction of even very small dielectric samples result in a measurable change in the resonant frequency and Q-factor. If these changes, and the sample size, are appropriately small, simplified perturbation techniques may be used to estimate the permittivity of the sample. For an empty

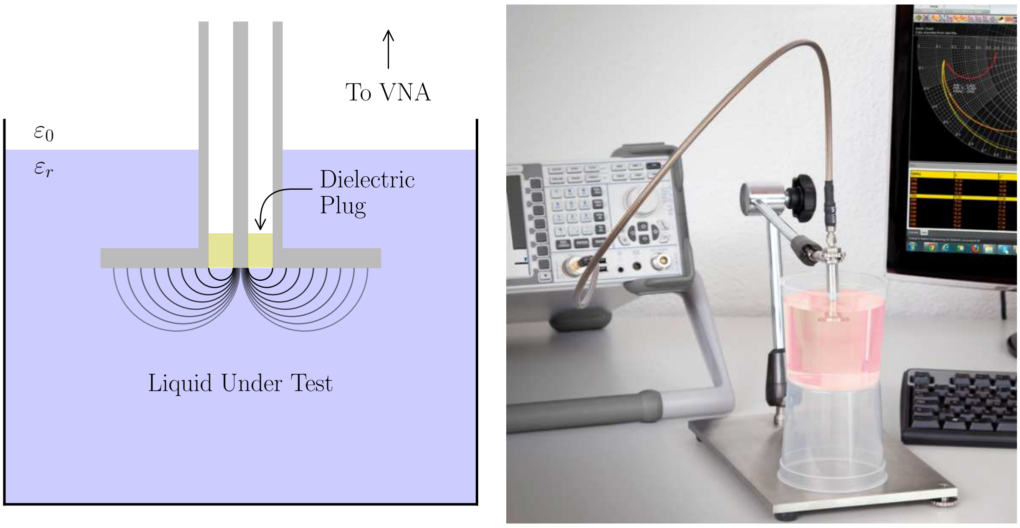

(a) Cross-section of the probe, showing example fringing.

(b) Typical liquid measurement [18].

Figure 1.13: Liquid sensing using an open-ended coaxial probe.

cavity where $f_r = f_0$ and $Q = Q_0$, and the same cavity with a small dielectric, or liquid, sample where $f_r = f_L$ and $Q = Q_L$, there exists the well-established perturbation formulae [19]:

$$\frac{f_0 - f_L}{f_L} = A\left(\varepsilon_r' - 1\right)\frac{V_s}{V_c} \tag{1.27}$$

$$\frac{1}{Q_L} - \frac{1}{Q_0} = B\varepsilon_r''\frac{V_s}{V_c} \tag{1.28}$$

where the constants A and B can be complicated functions of the resonant structure geometry and behaviour, and are more commonly found *via* calibration with a known sample. V_c and V_s refer to the cavity and sample volume, respectively. An example of a scenario where perturbation techniques may be suitable is the insertion of a dielectric rod or capillary tube, for liquid measurements, into comparatively large resonant waveguides, such as in [20].

A comprehensive study of established methods for permittivity measurements is perhaps beyond the scope of this thesis, but this section has briefly shown that accurate characterisation of dielectric and liquid samples has been achieved using a variety of methods, whether admittance, reflectometric or resonance-based. What follows is an overview of some recent contributions to the field of liquid sensing.

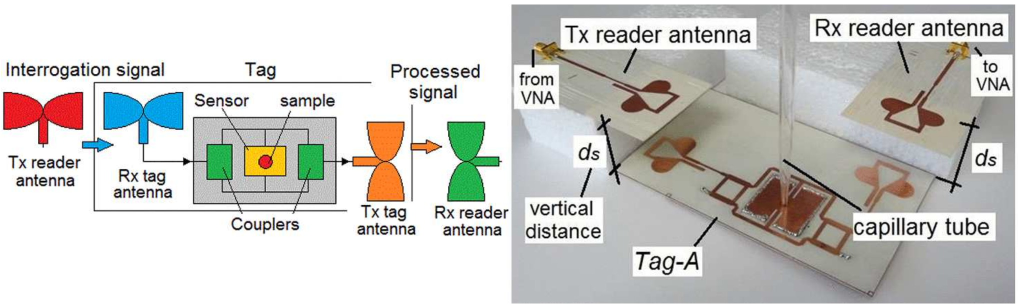

Figure 1.14: SIW-based wireless liquid sensor [28].

Resonant Cavities

Substrate-integrated waveguides (SIW) have found recent applications in liquid sensing, where the geometry lends itself well to the formation of resonant cavities. The SIW structure was first reported in [21], where the authors replaced the side walls of a rectangular waveguide with metallised vias enabling the integration into a regular substrate using standard fabrication techniques, metallised grooves may also be used. Using some form of impedance matching section [22–25], the SIW is readily matched to a regular microstrip line or other transmission line topology. A resonant cavity formed from vias was presented in [26], where a further cavity using the SIW geometry and fed with microstrip lines was shown to produce high-Q resonance in [27]. By perturbing the fields within an SIW cavity resonator, a sensor may be realised by relating the change of some parameter, such as the resonant frequency, with a liquid property.

The first attempt to use resonant SIW cavities for the characterisation of liquids is presented in [20], where Saeed *et al.* propose a microstrip-coupled cavity with a small glass capillary tube inserted through its side walls. Using perturbation techniques the complex permittivity of several liquids is reported, along with the assessment of a number of water mixtures, showing a total resonant frequency deviation of 1%. In [29] an X-band fluid sensor is designed by introducing a dielectric post to a resonant SIW cavity, where the post is filled with fluidic dispersions of oil and particulate. The sensor is shown to be highly sensitive, where a fluid permittivity range of 2.8 - 10.93 results in a resonant frequency decrease of 3 GHz, from 12 to 9 GHz. Morales *et al.* present two resonant SIW cavities in [30], where a quartz capillary tube is placed through the centre of each. Using the perturbation models developed by the authors [31, 32], the complex permittivity for a number of liquids is calculated. The ports were replaced in later work [28] with printed wideband antennas positioned orthogonally, as shown in Fig. 1.14, allowing for the incorporation of the sensors into a wireless measurement system, thus resulting in passive sensors. However, the data

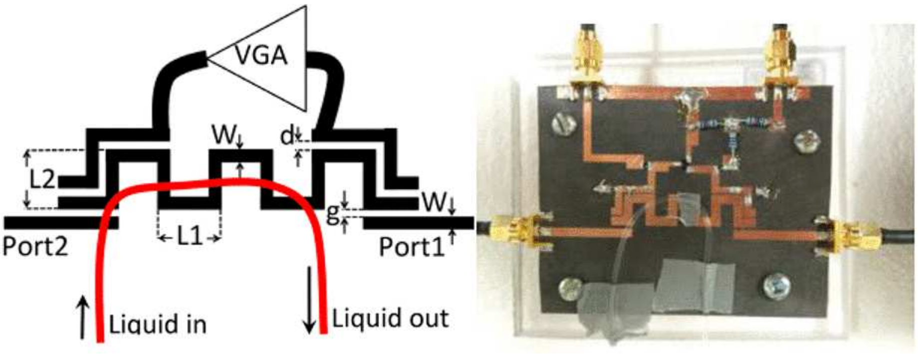

Figure 1.15: Half-wave microstrip resonator with active feedback loop [36].

is presented for very small read distances of 1 and 2 cm, where the latter distance also displays a significant degradation in the calculated permittivity values. Of final note with reference to SIW-based liquid sensors is the application of 3D printing technology in [33], where the authors fabricated a meandered microfluidic channel directly into the SIW cavity. The sensor displays a significant increase in sensitivity when compared with other sensors using SIW cavities referenced here, although the sensor was only tested with distilled water.

A more standard cavity formed from metal walls is discussed in [34], where a resonant rectangular waveguide cavity is connected *via* two coaxial probes. The waveguide features a narrow, $r = 0.5$ mm, Teflon (PTFE) capillary tube for the introduction of liquid samples. The Q-factor is very high, though the authors show that increasing the capillary radius by only 1 mm results in a very significant decrease in performance. The cavity is intended for the characterisation of different water solutions, and performs relatively well, though is noticeably larger and perhaps more costly than substrate-integrated equivalents.

Microstrip-Coupled Resonators

Microstrip is an attractive transmission line topology for a number of reasons, where it is low-profile, low-cost and easy to fabricate, and many sensors are designed with this in mind. Coupling a resonant structure to a microstrip line provides a convenient way to fabricate the sensor and potentially incorporate it into a wider system. Many microstrip-coupled sensors make use of a microfluidic channel placed in close proximity to an area where the resonant fields are of a high magnitude, and the perturbation caused by the channel is used to assess or characterise the LUT. Resonant structures placed directly next to a microstrip line are easily edge-coupled as a result of the fringing-field pattern [35].

Using a singly-split, rectangular ring coupled between two open-circuited microstrip lines, the authors in [37] discuss the appropriate placement of a microfluidic channel *via* S_{21} measurements. The input and output transmission lines are horizontally capacitively coupled to the ring, which displays a high field strength at the input coupling. Initially, the channel is situated perpendicularly to the microstrip, crossing the coupling region and one side of the resonator ensuring good perturbation of the resonant field. By instead embedding the microfluidic tube into the substrate, but along the same axis, there is seen to be more significant perturbation, where the authors report a 257% improvement in measurement sensitivity. A similar rectangular split ring is presented in [38], whereas in this case it is formed by etching the ring out of the ground plane below the microstrip line, known as a complimentary split ring resonator (CSRR). The through-line couples to the CSRR through the substrate, and is placed across its centre to ensure maximum coupling. The greatest field strength is observed along the resonator edge opposite to the split, and the microfluidic channel, attached directly to the sensor, is therefore positioned directly above this point. Measurements of ethanol and water show a good degree of sensitivity at around 25%, and the self-contained nature of the liquid channel is an advantage of this sensor design. In [39] a elliptical split-ring is edge-coupled to a microstrip line *via* an elongated, straight edge. The ring's split is formed by two narrow tips rather than the straight edges shown in [37] and [38], and a liquid sample reservoir is placed directly over the centre of the gap. The sensor relies on the loss of the liquid sample to cause a decrease in the Q-factor, as the resonance is negligibly affected by changes in ε'_r. Measured results of varying NaCl concentrations in water display a relatively low-Q response, which is undesirable given the sensor's reliance on the measured Q-factor. To compensate for this, the authors introduce a cylindrical dielectric resonator between the microstrip and elliptical split-ring. The resonance of the cylinder is tuned by the liquid reservoir, and results in an increase of the Q-factor by an order of 30, where the adapted sensor displays a measurable decrease in Q for increasing NaCl concentration. The authors in [36] propose a meandered half-wave resonator capacitively coupled to open-circuited microstrip lines at the input and output port, as seen in Fig. 1.15. The resonator is further coupled to an active feedback loop containing a BJT transistor intended to increase the Q-factor of the sensor. S_{21} measurements are presented for both passive and active configurations, where it could be argued that when passive the sensor does not show any change in resonant frequency to even very high values of permittivity, such as that of water. In the active configuration the response is improved and displays a very high-Q, but also very low sensitivity, on the order of a 0.03% change in f_r. Using the same sensor,

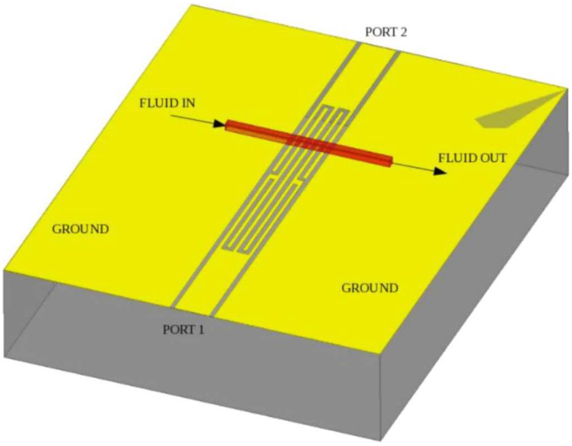

Figure 1.16: High-frequency coplanar waveguide sensor with microfluidic channel [41].

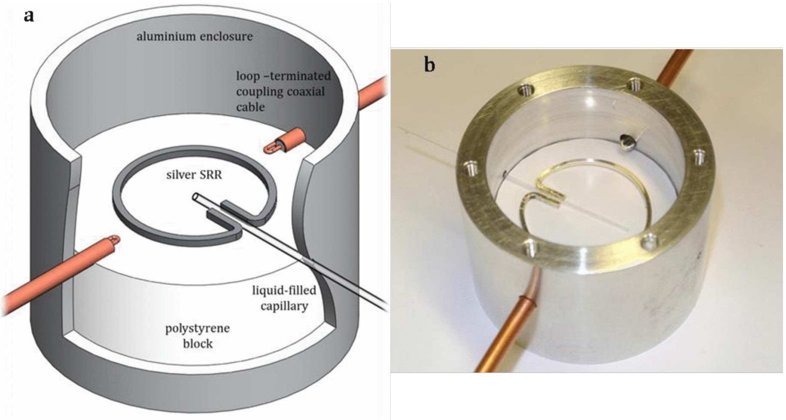

Figure 1.17: Split-ring based structure with extended capacitive region and microfluidic channel [42].

the authors measured particle deposition in [40], where sand was added to tubes of water and measured over time as the sand particles settled. While the sensor is able to measure changes at distances of a few centimetres, the change in resonant frequency is around 0.004% and potentially highly susceptible to noise or movement, the latter of which is shown to change f_r. Nonetheless, [40] displays one of the few sensors capable, at least in a limited capacity, of non-contact sensing of liquids in a practically-sized container, where microfluidic channels require specialist equipment or fabrication techniques.

Alternative Structures

In [43], an attempt to measure liquids at millimetre-wave frequencies using a gap waveguide structure is undertaken. The sensor consists of a transmission line with an open-circuited $3\lambda/4$ stub at its centre, the end of which passes underneath a microfluidic channel. With no liquid present the sensor operates at 59 GHz, changing to 52 and 49 GHz for methanol and air, respectively, showing a relatively high ($> 15\%$ change in f_r) level of sensitivity. The use of gap waveguide is justified due to the very high losses in both microstrip and SIW devices at millimetre-wave frequencies. A high-frequency, coplanar waveguide sensor is realised in [41], consisting of a folded quarter-wave resonator and bonded microfluidic channel positioned perpendicularly to the central conductor direction, as shown in Fig. 1.16. The proposed sensor is very compact, where the entire device is 1.03×2.4 mm, for a centre frequency of 22.62 GHz with no liquid present. Measurements of an ethanol-water mixture show good sensitivity, displaying a resonant frequency change of around 1.5 GHz over a permittivity range of 20.6 to 44.7. The authors additionally present models to estimate the complex permittivity of the solutions, claiming a worst-case error estimate of 6.5%. Although the majority of liquid sensors measure or characterise the electrical properties of a LUT, liquid level is also an important parameter for consideration. Using four rectangular electrodes affixed at regular intervals to the inside of a plastic pipe, [44] uses capacitance measurements to sense the level of water. The sensor appears to be capable of measuring level changes of < 5 mm in a pipe of inside radius 52.5 mm. Additionally, by separately monitoring each of the four capacitance values resultant from the four electrodes, an estimation of the pipe angle or gradient can be made. A further split-ring structure was studied in [42], which considered a split-ring based design with a microfluidic channel. The split or slot region features an elongated capacitive section which extends inwards towards the centre of the ring, as shown in Fig. 1.17, producing a larger volume over which the resonant electric field may be perturbed resulting in greater sensitivity. The microfluidic channel is situated between the extended ‘legs’, and the ring is excited *via* loop-terminated coaxial cables within an aluminium enclosure. The structure shows a significant improvement in sensitivity over a an identical split-ring without the extended section, where measurements of various liquids up to $\varepsilon_r \approx 80$ agreed relatively well with simulations, although this agreement deteriorated for smaller loop radii.

A number of sensor designs centred around advances in inkjet printing technology are reviewed in [45]. The authors of [46] present the incorporation of two T-resonators, originally simply microstrip-coupled, with an RFID-enabled system, complete with two folded dipole antennas and an RFID chip. A microfluidic channel runs through each of the capacitive gaps in the T-resonators, altering their resonant frequency accordingly. The entire device is inkjet-printed, and presents a completely passive liquid sensing tag, readily incorporated into existing RFID systems. An inkjet-printed coplanar patch antenna with incorporated microfluidic channel is discussed in [47], which displays a varying frequency of operation for water, ethanol and hexanol.

Conclusion

There exists a number of established methods for the measurement of the complex permittivity of liquids [17], but this thesis does not intend to present a sensor capable of such accurate analysis. Indeed, a review of recent literature reveals the great deal of effort expended to design sensors with this capability, with varying success [20, 28, 30, 41]. Instead, it is the real-time monitoring of known liquids which is of interest, particularly in the context of an active industrial environment containing potentially hazardous materials. Assuming that the LUTs are known, highly accurate measurement may not be necessary and neither therefore is the possible expense resultant from the instalment of sensors offering such performance. Finally, we consider that an industrial environment may well feature numerous liquids in various locations at different stages of processing, and any active sensing system will require associated cabling causing obvious issues with complexity and cost, whereas a passive device may be more suitable. The justification for these design considerations will be discussed further in the following section and chapter, but they are mentioned briefly here to enable appropriate analysis of the recent literature. Given the proposed application of the liquid sensor, contributions to the field discussed in the previous section may be assessed with reference to this contextualisation.

It is of note that many of the techniques require a liquid sample to be taken and introduced at some point on the sensor [28–30, 39]. This is not a particular issue in terms of measurement capability, but presents problems if we consider that the LUT may be corrosive, toxic or otherwise hazardous, as well as introducing a total increase in measurement time. In such a case, it is advantageous to design a sensor which does not necessitate the taking of samples, or rather, is designed as a non-contact sensor where the LUT never comes into contact with any part of the sensor geometry. Each of the microfluidic-based devices reviewed achieves this particular aim, where the LUT is passed in close-proximity to the resonant area of the sensor without touching it, with the exception of [38]. However, if we consider a practical measurement environment, such as some industrial process, the dimensions of the tube or pipe used to support a sensor's liquid channel may be very small when compared with *in situ* piping containing a potential LUT. If we wish to measure or monitor the liquid(s) contained by such piping, a microfluidic-based sensor would require some form of offshoot pipe to provide the very small volumes of liquid required, with great care taken not to introduce air bubbles which could significantly change the response for sensors featuring channels of such small radius. Alternatively, samples may be taken and introduced to the sensor *via* syringe or some other method, although this returns to the previous point on hazardous liquids. Installing connections to *in situ* pipes is not an insurmountable issue, but does result in added cost and rigidity of the sensing system, where every additional sensor requires an additional connection. There is also a decision to be made as to whether the appropriate sensor is to be passive or active, where the latter can show significantly improved performance [36]. Passive sensors may be re-purposed as wireless tags by replacing ports with antennas to enable remote sensing, but there are added issues with the effect of the read distance [28]. In the context of the proposed sensor application, a passive, wireless sensor would be advantageous in terms of system cost and complexity due to the lack of cabling and power requirements. Finally, we also consider that pipes are cylindrical in nature and very few sensors in the literature conform to such geometry, generally due to the requirement of a supporting, rigid substrate. A sensor which could be placed directly onto an *in situ* pipe would greatly reduce installation complexity, and therefore cost, allowing for 'on-pipe' measurement. In light of the review of relevant literature and proposed sensor application, the next section will introduce the central aims of this thesis, and the associated objectives.

1.5 Aims and Objectives

The intended purpose of the liquid sensor proposed in this thesis is the *in situ*, on-pipe, real-time monitoring of known liquids in an active industrial environment, with an emphasis on cylindrical geometry. The work presented here aims to solve a number of issues faced in the practical sensing of liquids for such an application, where these issues may be broadly categorised into the following areas:

- Cost
- Complexity
- Robustness
- Precision
- Adaptability

The first two aims are intrinsically linked, in that low-complexity will generally result in a lower price for producing, purchasing and maintaining a sensing device or system. Known liquids do not necessarily require highly-accurate characterisation, and it is not desirable to pay for performance which is not required. As such, this thesis aims to present a sensor which is low-cost and low-complexity, but still offers satisfactory performance for a particular environment and intended use. A significant step towards achieving these aims can be made by designing a passive, wireless sensor with no active circuitry.

Robustness concerns resistance to a practical environment, where measurements should be consistent and not significantly affected by their environment or a certain level of interference. The sensing device or system should be resilient to small movements, hazardous liquids, electrical noise and so forth, without resulting in a significant degradation of performance. By measuring various impacts of a practical environment, the robustness of the performance of a sensor can be assessed to a certain extent.

The use of a sensor as an absolute measuring device, such as the extraction of the complex permittivity of a material, requires high levels of accuracy in the determination of *absolute* permittivity values. In practice, this is difficult to achieve with a low-cost, low-complexity sensor. However, many industrial processes use known liquids which may not necessarily require accurate characterisation, and instead, it may be sufficient to monitor a given process to check for inconsistencies or errors. An example of this would be the assessment of some container which, under ordinary circumstances, should contain only water. The sensor would provide a characteristic response for the electrical properties of water and would therefore straightforwardly detect if there was another material or liquid present, as a result of an unexpected response. The example of water may be expanded to any number of liquids provided there is a large, detectable change in the LUT ε, to be determined by the sensitivity of the sensor. In this scenario it is sufficient to calibrate the sensor for known liquids, allowing particular frequency responses from a given sensor geometry to correspond with particular liquids. A sensor of high *precision*, one which produces consistent measurements, would allow for such a monitoring system, where the complexities of a high-accuracy alternative may be unnecessary and costly.

A cylindrical sensor designed for on-pipe measurement requires some consideration with regards to its adaptability. Discussion around microfluidic-based sensors concluded that the addition of connections to *in situ* pipes introduces added expense and complexity, and so where possible, it would be desirable to remove the requirement of any additional components aside from the sensor itself. The design of a sensor which is adaptive with regards to its radius is advantageous, as it increases the range of pipes on which it could be placed. Additionally, the prospect of multiple sensors in the same environment, placed on multiple pipes for example, raises the issue of interference. In this case it would be desirable that the sensor is tunable, where different sensors can be separated in the frequency domain to reduce response overlap. Finally, we have seen that the dielectric loss present in liquids can reduce the Q-factor, potentially very significantly. A sensor which only operates for low-loss scenarios would be restricted in the range of liquids it is capable of monitoring, and so it is important that the proposed sensor design is adaptive or resilient to high-loss liquids.

The sensor presented in this thesis should be designed to satisfy the aims discussed above. Therefore, the central objectives intended to achieve those aims can be defined in terms of the sensor performance, where it should be:

- Passive and wireless
- Conformal to cylindrical geometry
- Resilient to a practical measurement environment
- Consistent and precise
- Adaptive to different geometry, liquids and applications

The work presented in the following chapters seeks to address each one of these objectives in a way which is measurable and quantifiable, where applicable.

1.6 Thesis Outline

This thesis will first present an introduction to the main body of work in chapter 2, discussing the geometry, theory and simulation of the liquid sensing device. Chapter 3 will present experimental results and measurements, also covering experimental configurations and methodology, along with sensor fabrication and data processing techniques. In addition, chapter 4 will introduce some further applications of the liquid sensor, including the sensing of level and temperature. Finally, the conclusion will offer a summary of the information presented in this thesis and discuss potential future work.

Chapter 2

Theory & Simulation

This chapter intends to introduce the sensor geometry and its general principle of operation, before moving onto theoretical analysis. Following this, a comprehensive set of simulated results is presented to display the behaviour of the sensor through a full parametric study covering all relevant dimensions of the device. First, an introduction to the sensor design and basic operational description is necessary.

2.1 Sensor Introduction and Scope

The previous chapter made several references to an 'industrial environment', in which the proposed sensor is intended to operate. Several examples of such an environment can be seen in Fig. 2.1, showing metal and non-metal pipework, where this thesis is mostly concerned with the latter. A passive, wireless cylindrical resonator placed directly onto one of the plastic pipes shown would have its resonant field distribution perturbed by the pipe and its contents, and from this perturbation we may retrieve information regarding the liquid within the pipe. Such a sensor would require no samples, no offshoots or connections, no power or cabling, and for appropriate *in situ* pipe radii, potentially no disruption to a live industrial process. Pipe radius is mentioned due to impractically low resonant frequencies for sensors of a large radius, as will be discussed later. It will also be shown later that a number of sensors may be deployed within the same industrial setting, allowing multiple pipes, and therefore liquids, to be monitored simultaneously using only one transmitting antenna.

The term *monitor* is occasionally used to distinguish the application of the sensor from others which aim to accurately characterise liquids and provide absolute values of permittivity from theoretical models. Additionally, the sensor seeks to perform real-time measurements due to the lack of sampling required, which is more

Figure 2.1: Example of industrial processes utilising metal and non-metal piping.

appropriately described as monitoring a LUT. Although the sensor is still used to *measure* the liquid, it is only intended to return a particular resonant frequency corresponding with a given permittivity value within the pipe. It would be possible, nonetheless, to measure a number of reference liquids [17] with a sensor of fixed dimensions to produce a calibration curve of resonant frequencies, but no attempt is made to utilise the sensor as an accurate measurement device in this work. As an example of a monitoring process, consider a situation in which water is removed from another liquid, such as ethanol, through multiple rounds of filtering. Assuming the permittivity of water is considerably higher than that of the alcohol, a valid assumption for most alcohols, we would observe the reduction in ε_r of the liquid mixture as water is removed. Therefore, the resonant frequency of a sensor measuring this mixture would increase as the percentage of water decreases, until the mixture becomes the pure alcohol. Now, consider that a purity grade of 95% is required, we may define a particular resonant frequency which occurs for this particular mixture, and immediately halt the process once the sensor responds with the predetermined f_r. The proposed real-time monitoring sensor is highly-suitable for this application, as its response time is limited only by the interval of the transmitting antenna. In the previous example, the sensor can be thought of simply as a threshold detector, and this could be a convenient way to describe its application.

Due to its passive operation, the sensor's response to an external stimulus will result in energy losses within the LUT, the extent of which is a function of the dielectric loss of the liquid, and cannot be recovered *via* active components. Additionally, its wireless operation will cause reductions in the amount of energy contributing to its excitation due to path loss effects in the wireless channel. These effects combine to increase the energy loss and decrease the average energy stored, causing a reduction in the Q-factor of the sensor response in accordance with 1.24. Therefore, it is important that the sensor is capable of adapting for high-loss liquids or larger measurement distances.

Geometric Overview

The proposed sensor geometry is relatively straightforward, consisting of a metal cylinder featuring a single slot along its length, as shown in Fig. 2.2. The cylinder may be placed directly onto a non-metal pipe, forming an inhomogeneous dielectric cavity containing the *in situ* pipe and its contents, or what can be thought of as the liquid channel or cavity. By etching the structure onto a thin film, such as Mylar or Kapton, it can be readily affixed to pipes such as those shown in Fig. 2.1 without the need to remove any sections or halt processes. The sensor may also be incorporated with metal pipe structures, but would necessitate the instalment of an intermediate section of non-metal pipe, contrary to the aims of simple installation. A summary of the annotated dimensions is given in Table 2.1, and it should be assumed that this notation will always refer to the given dimension, unless specifically otherwise stated.

Table 2.1: List of sensor dimensions as shown in Fig. 2.2.

Notation	Dimension (mm)
SW	Slot width
SL	Slot (or sensor) length
r	Outer radius of pipe
a	Metal thickness
d	Pipe wall width

The metal width a is exaggerated in Fig. 2.2 for clarity, and in practice would be very thin relative to the pipe wall width d. The slot width SW is also seen to be relatively large for annotation purposes, but is generally very small. Dimensions given in Table 2.1 present a number of design parameters for analysis and performance tuning, and will be discussed in great detail in the next few sections, but first we discuss the general principle of operation.

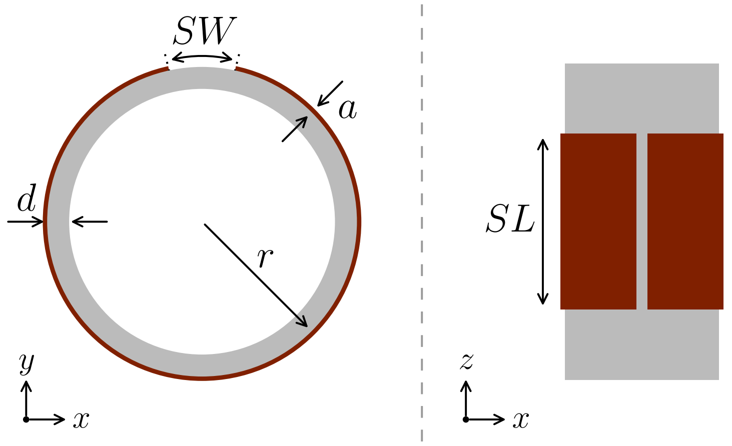

Figure 2.2: Cross-sectional and bird's-eye view of the slotted cylindrical structure.

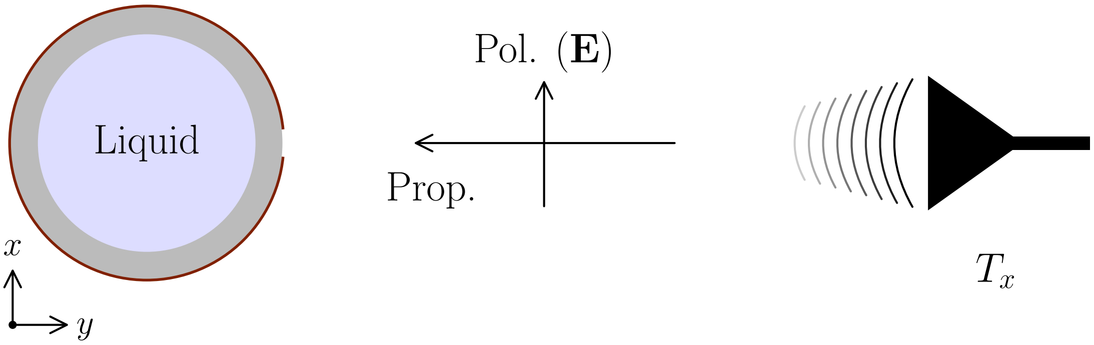

Figure 2.3: Excitation configuration showing the transmitting antenna T_x.

Principle of Operation

The literature review has shown that in order to extract information regarding properties of the LUT, there must be some method of penetrating the liquid with a resonant field of some sort, or to view it another way, the liquid must perturb the resonance observed when no LUT is present. As the proposed sensor is passive it necessarily relies on another system, such as an antenna, to provide the interrogative external electric field. An incident plane-wave which is polarised perpendicularly to the slot axis, as shown in Fig. 2.3, results in the excitation of a strong electric field in the slotted region. For a relatively large metal thickness, Fig. 2.4 shows a simulated, cross-sectional view of the resonant field, where the field fringes upwards into free-space and downwards into the sensor cavity. The simulation method and environment will be discussed in detail in section 2.3.1. The sensor is shown here with no pipe or liquid present, where the perturbation effects caused by their introduction to the sensor cavity is discussed shortly. It is the portion of the resonant field that

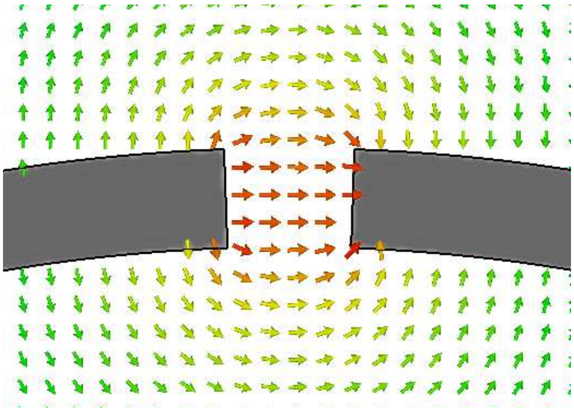

Figure 2.4: Electric field between the slot edges in free-space.

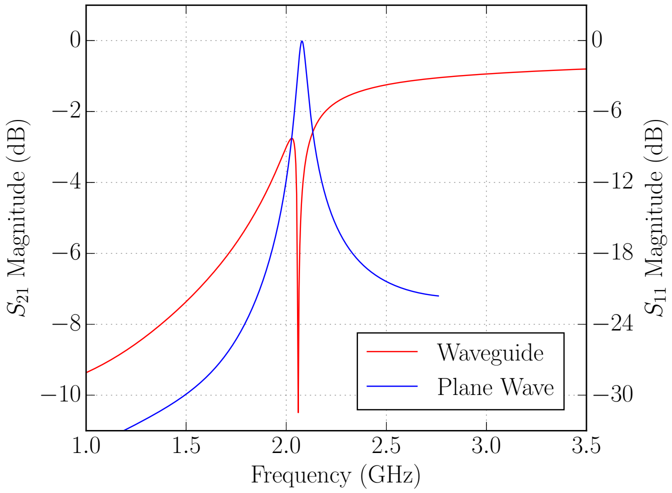

Figure 2.5: Simulated S_{21} magnitude when the sensor is excited as a waveguide and S_{11} magnitude when excited by a plane wave.

extends downwards into the cavity that is of interest, as it is this portion which will interact with the LUT. At this point, with reference to Fig. 2.4, it is worth noting that the pipe wall will act to move the liquid cavity away from the area of maximum field strength by a distance of d. This will have the effect of reducing the sensitivity of the sensor to changes in the permittivity of the LUT due to reduced field perturbation, as demonstrated by [37]. The effect of d will be discussed in a later section, but Fig. 2.4 allows for an intuitive introduction to the issue.

There is some consideration as to whether the slotted cylinder is viewed as an elongated or extruded split-ring structure, or as a type of slotted circular waveguide. A comparison of simulated results when the sensor is excited as a waveguide and as a split-ring structure can be seen in Fig. 2.5. The S_{21} behaviour of the slotted waveguide is as expected, where a significant loss of energy, due to radiation, is observed at its cut-off frequency f_c, behaving similarly to a slotted SIW studied in [48].

This correlates almost exactly with the S_{11} result obtained when exciting the sensor with a plane wave, where a large reflection is observed at f_c. This suggests that the split-cylinder structure resonates at its equivalent waveguide cut-off frequency, which also agrees with an analysis of the electric field along the slot discussed in a later section. This thesis will generally refrain from direct comparisons with split-rings or waveguides in subsequent sections to avoid confusion, as either the geometry, application or behaviour of the sensor tends to be inconsistent with these structures.

The simulated resonant electric and magnetic field magnitudes of a short (small SL) sensor for the first 2 modes are shown in Figs. 2.6 and 2.7, showing a cross-sectional and side view, respectively. It should be noted that the dynamic range of the field strengths has been chosen to best display their distribution, where some quantitative analysis will follow later. The electric field magnitude of the fundamental mode is maximum in the slotted region and tends towards zero at the bottom of the cavity, whereas the magnetic field distribution is the opposite. We note that the electric field pattern in Fig 2.6 a) appears to be a perturbed version of the TE_{11} mode observed in circular waveguide, where the slot has replaced one of the nulls [49]. The 1^{st} harmonic exists at around $3.5f_0$ and displays 3 nulls around the cavity, though is of no intended practical use in this study. The same field magnitudes can be seen in Fig. 2.7 from a cross-section through the slotted region of the sensor. Though it is interesting to see the magnetic fields and their relation with the electric fields, there is no added benefit in simultaneously analysing them within the scope of this thesis. As such, any further discussion on field distributions will focus solely on the electric component unless otherwise stated. As the field magnitude is maximum in the slotted region, it is important that the sensor is orientated vertically to ensure that the LUT occupies this region to achieve the greatest sensitivity. Alternatively the sensor may operate horizontally if necessary by facing the slot downwards, allowing liquid to flow over the slot even in cases where the pipe is not full.

In addition to the resonant E and H fields, the related surface current magnitude of the fundamental mode can be seen in Fig. 2.8 for a sensor of relatively large a, which is shown for clarity. Fig. 2.8a shows the x or horizontal component, where the maximum is observed along the bottom edge of the sensor. The y or vertical component is displayed in Fig. 2.8b showing the expected maxima over the vertical sections of the device, in opposite directions. The current magnitude is evaluated along a path which travels around the sensor from one slot edge (a) to the other (c) in Fig. 2.9, showing the expected distribution of zero at the slot edges and a maximum at the base of the sensor. The noisy element of the plot is related to

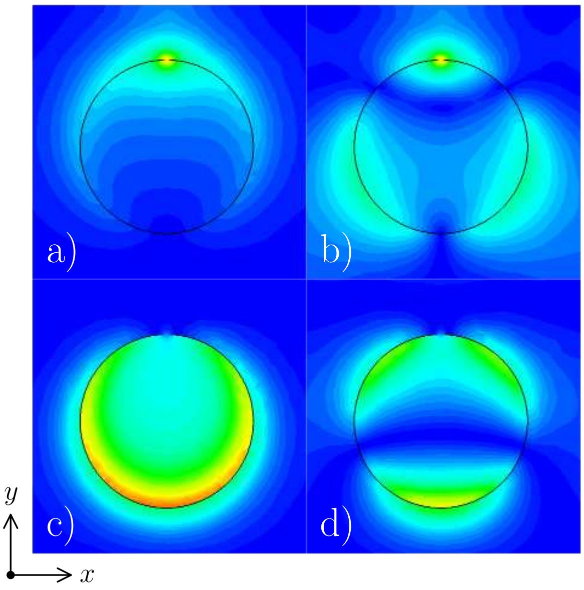

Figure 2.6: Cross-sectional view of resonant field magnitudes, where a), b) show the E-fields of the fundamental and 1st harmonic modes, respectively, and c), d) show the related H-fields.

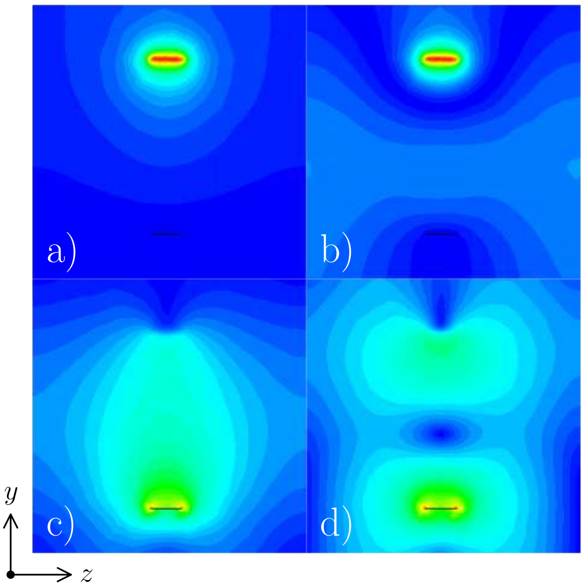

Figure 2.7: Side view of the resonant field magnitudes displayed in Fig. 2.6.

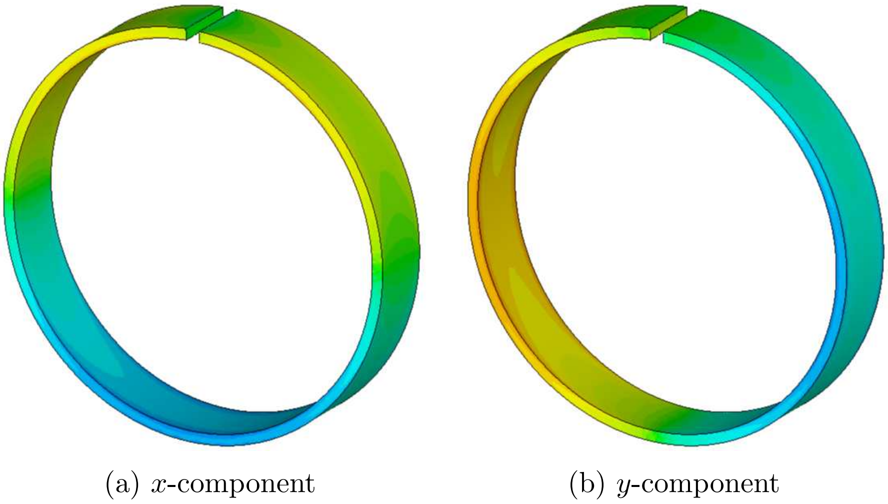

(a) x-component (b) y-component

Figure 2.8: Surface current plot of the x (horizontal) and y (vertical) components at resonance.

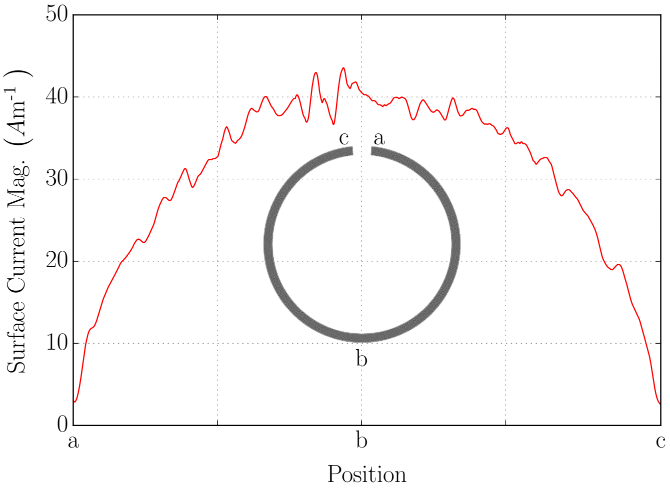

Figure 2.9: Simulated surface current magnitude between the slot edges.

the non-uniform discretisation of the simulated model, along with other meshing constraints which will be discussed briefly in section 2.3.

In practice the sensor will be placed onto to a pipe, resulting in perturbation of the fields displayed in Figs. 2.6 and 2.7 as discussed previously. Discussion related to Fig. 2.4 also mentioned that the pipe will physically separate the LUT from the maximum field intensity in the slotted region by a distance of d. There are a couple of considerations related to the *in situ* pipe to note here. Eq. 1.14 shows that frequency decreases by a factor of $1/\sqrt{\varepsilon_r}$, and so the real part of the permittivity of the pipe material will set the maximum resonant frequency of the sensor, that which is observed when the pipe is empty. More importantly, the dielectric loss of the material will attenuate the field within the pipe walls and significantly dampen

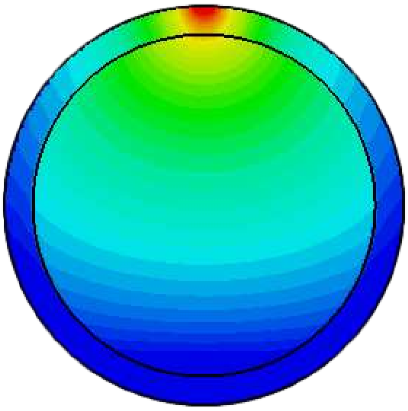

Figure 2.10: Electric field magnitude in the presence of a pipe.

the sensor resonance. From a more practical perspective, the pipe must be resilient to a large range of corrosive or hazardous liquids, as well as high temperatures as may be expected in an industrial environment. With these considerations taken into account, both theoretical and practical, polytetrafluoroethylene (PTFE) was selected as the pipe material. PTFE has a well-characterised, near-constant permittivity of $\varepsilon_r \approx 2.1$ across a large frequency range, and a very low loss tangent $\tan\delta \approx 0.0005$ in combination with excellent chemical and thermal resistivity [50]. Though this study only considers PTFE, other polymers could be used, such as uPVC. For future discussion, the sensor cavity refers to the region of space within the metal layer formed by the sensor, and the liquid or pipe cavity specifically refers to the region of space bounded by the internal pipe walls.

The field perturbation caused by the PTFE pipe can be seen in Fig. 2.10, where the electric field is significantly reduced in the pipe walls relative to the liquid cavity. In this case, the pipe is filled with air, and $\varepsilon_{air} < 2.1$, so we observe the expected behaviour. The extent to which energy will be concentrated within the pipe walls or liquid cavity is determined by the electrical properties of the pipe material ε_p relative to its contents ε_r. As ε_r increases relative to ε_p we expect to see an increasing concentration of the electric field within the pipe walls, where generally $\varepsilon_r > \varepsilon_p$. To better observe the field distributions resultant from different materials in the liquid cavity, the relative permittivity ε_r of the liquid cavity was varied from $1 \leq \varepsilon_r \leq 81$ and simulated. The resultant field distributions can be seen in Fig. 2.11, where the penetration of the field into the pipe walls for higher values of ε_r can be seen very clearly. Additionally, we see that there is almost no discontinuity in the electric field magnitude across the pipe and liquid cavity boundary when $\varepsilon_r = 2$, as the sensor cavity is almost homogeneous. It should be noted that the colour map was

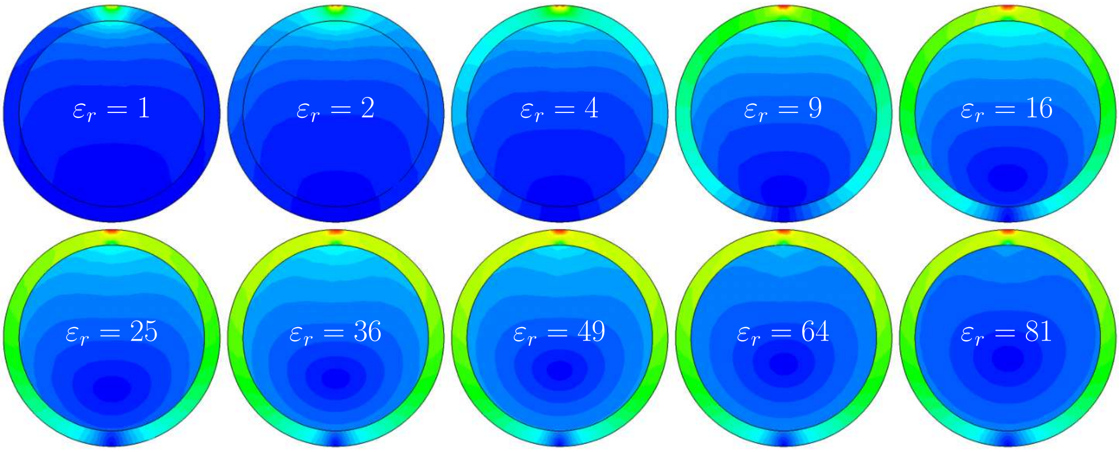

Figure 2.11: Field plots at resonance for varying dielectric constant within the pipe.

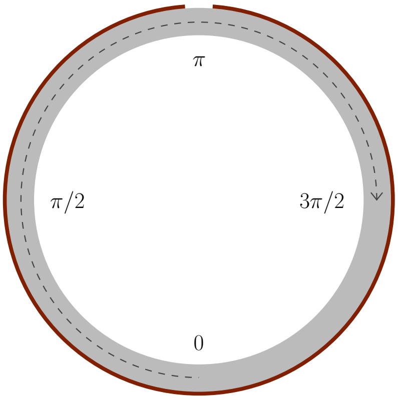

Figure 2.12: Cross-sectional view showing the position of the curve within the pipe wall.

dynamically generated for each simulation based on each particular range of electric field values, and the colours are not representative of equivalent field strengths between images.

To expand upon the idea of field concentration within the pipe walls, the magnitude of the resonant electric field was extracted from a cross-sectional, circular path in the centre of the pipe wall, shown in Fig. 2.12, to provide some form of quantitative analysis. For $1 \leq \varepsilon_r \leq 64$ the normalised field magnitude is displayed in Fig. 2.13, where position π is the slot centre. It is clear that, as ε_r increases, the field is increasingly concentrated within the walls of the pipe. This result corroborates the qualitative assessment of field distributions shown in Fig. 2.11. The appropriate choice of pipe material is therefore important, as a lossy material would severely dampen the resonance of the sensor, this will be discussed further in section 2.3.2.

This section has introduced some of the key concepts of the sensor operation,

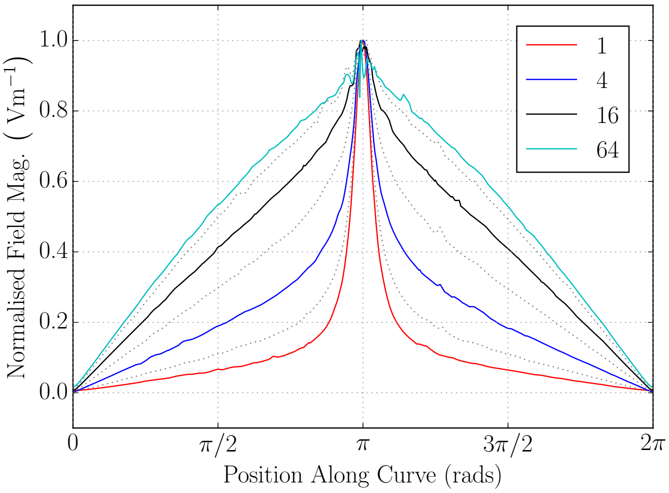

Figure 2.13: Normalised electric field strength along the curve shown in Fig. 2.12 for $\varepsilon_r = 1$, 2, 4, 8, 16, 32 and 64.

including resonant field distributions, design considerations, excitation and cavity perturbations. Though not mathematical, the descriptions present an introduction to different aspects of and points of analysis for the sensor geometry. The next section will discuss a theoretical approach to the proposed liquid sensor.

2.2 Theory

The nature of the sensor, in terms of its geometry and inhomogeneity, make it difficult to model accurately. Nonetheless, this section intends to provide some form of theoretical analysis which can potentially be used to predict trends or observe the effect of parametric changes. Before presenting specific theory, some simplified analysis is perhaps useful to illustrate the difficulties in modelling the sensor geometry, particularly owing to its inhomogeneity.

2.2.1 General Discussion

Fig. 2.14 shows a representation of the fringing fields at resonance, suggesting that they penetrate the liquid cavity to a greater extent as the slot width increases. This is intuitively true, but will also be shown through simulations in a later section, here we are concerned with the impact of fringing on the effective permittivity ε_e of the sensor cavity. It should be noted that the fringing field lines which are outside of the cavity above the slot are not shown in this diagram. For narrow slots, such as the smallest one shown in Fig. 2.14, the fringing is relatively small and most of the field inside of the sensor cavity is concentrated within the pipe wall of permittivity

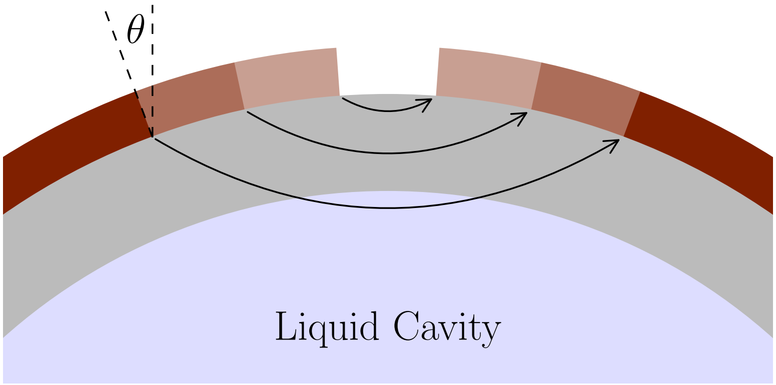

Figure 2.14: Cross-sectional view depicting fringing field lines for different slot widths.

ε_p. In this case, the effective permittivity of the region around the sensor may be approximated as $\varepsilon_e = (\varepsilon_0 + \varepsilon_p)/2$, or ≈ 1.55 in the case of PTFE. However, it is clear that as SW increases the field fringes further into the sensor and liquid cavity. The determination of the effective permittivity in this case is considerably more difficult, and would require a numerical or simulation-led approach. A second point of interest from 2.14 is the angle of the slot edge faces, shown by θ for the largest SW. For clarity, the faces form the inside edges of the slot and run along the length of the sensor, with an area $A = SL \cdot a$. Modelling the two faces as parallel plate capacitors, as will be the case later in this section, is increasingly inaccurate as the slot width increases. Additionally, the fringing fields will travel further upwards into free-space as θ increases, potentially impacting the effective permittivity of the sensor cavity. The issues described here should provide some rationale for avoiding a rigorous application of Maxwell's equations to describe the sensor, which could alone be the subject matter of a future thesis. Instead, this work draws upon relevant literature to provide a theoretical model which is applicable to a particular range of sensor dimensions, where the limits of this range will also be discussed.

2.2.2 Theoretical Model

The expressions presented in this section are extracted from work undertaken by Sydoruk *et al.* in [51], where an attempt was made to analyse a singly split ring (SR), two of which are used to construct the more common split-ring resonator (SRR) for which there exists analytical models [52, 53]. Analysis of SR structures generally focusses on planar rings fabricated in microstrip where $SL \ll a$, such as work presented in [54]. The sensor presented here is instead elongated or extruded along the slot axis and more appropriately referred to as a slotted cylindrical resonator, and

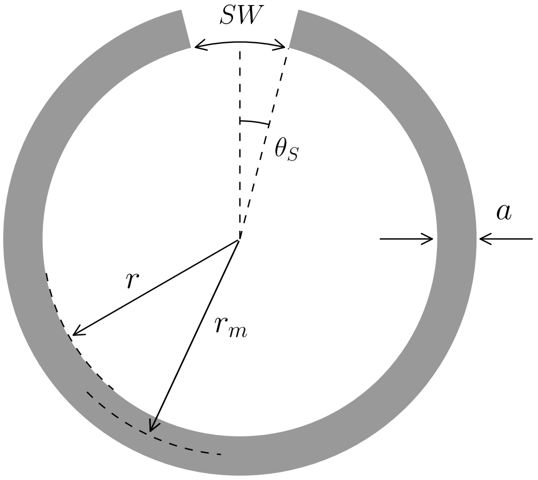

Figure 2.15: Cross-section of the free-space sensor used for the theoretical model, the slot length SL is as defined in Fig. 2.2.

the geometry of the 'split rings' studied in [51] are similar in appearance ($SL > a$). For ease of reference, the sensor cross-section shown earlier in Fig. 2.2 is shown again in Fig. 2.15, but with slightly different annotation. This diagram is valid only for this section due to the expressions formulated in [51], where further references to the sensor geometry in subsequent sections and chapters will be in relation to Fig. 2.2. It is worth noting that there is no pipe present in Fig. 2.15, where the geometry is assumed to be in free-space.

The expression given for inductance is similar in form to the self-inductance of a circular loop found from analysis of the mutual inductance between two filamentary loops [55]:

$$L_0 \cong \mu \, r_m \left[ln \left(\frac{8 \, r_m}{a} \right) - 2 \right] \tag{2.1}$$

where $r_m = r - a$ and a is the wire radius, not to be confused with the dimensions shown in Fig. 2.15. The inductance of the singly split ring is given as [51]:

$$L = \mu_0 \, r_m \left[ln \left(\frac{8 \, r_m}{SL + a} \right) - 0.5 \right] \tag{2.2}$$

where $r_m = r + a/2$. Given that Eq. 2.2 arises from analysis of loops, it is assumed that a small slot will not significantly affect the total inductance, hence the lack of a SW term. However, this is true only for very small slot widths, where larger values of SW will reduce the total inductance by simply removing a length of conductor. If we assume the inductance to be distributed around the ring, then we

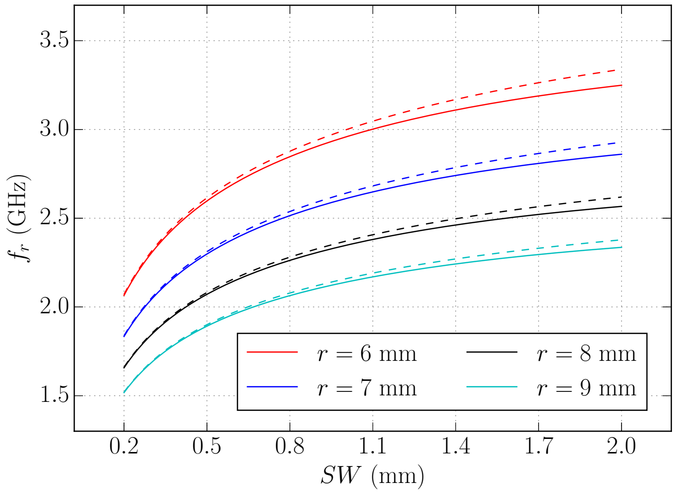

Figure 2.16: Comparison of Eq. 2.2 (solid) with the corrected inductance (dashed).

may reduce the total value as a function of SW:

$$L = L_0 \left(\frac{2\pi r - SW}{2\pi r} \right) \tag{2.3}$$

where L_0 is the inductance from Eq. 2.2. Using this correction with the capacitance models introduced next, we see a comparison of the theoretical f_r with L_0 for increasing slot width in Fig. 2.16. For small values of SW there is very little change as $2\pi r - SW \approx 2\pi r$, but larger slot widths show a divergence as the corrected inductance decreases with SW, resulting in a higher frequency resonance. The difference is only relevant for relatively large slot widths, but should certainly be considered for accurate modelling, particularly for sensors of a smaller radius.

The capacitance is more troublesome, and an initial assessment would quite rightly assume that the two slot edges act as parallel plate capacitors, for which the capacitance in free-space is given by:

$$C = \frac{\varepsilon_0 A}{d} \tag{2.4}$$

where A is the area of each plate and d is their separation, not to be confused with the pipe wall width. Eq. 2.4 assumes that the electric field is constant and confined to the area between the two plates, neglecting fringing field effects. To account for this fringing a correction term may be added to Eq. 2.4, and setting $A = SL \cdot a$ and $d = SW$ for the sensor geometry, the capacitance in the slot, or gap capacitance, is equal to:

$$C_{gap} = \varepsilon_0 \frac{SL \cdot a}{SW} + C_0 \tag{2.5}$$

where C_0 is the expression for the fringing field given as [51]:

$$C_0 = \varepsilon_0 \left(SW + SL + a \right) \tag{2.6}$$

In addition to the gap capacitance, charges on the inner surface of the ring contribute to the overall capacitance, where this effect is referred to as surface capacitance C_{surf}. One might assume the contribution of C_{surf} to be small or negligible in comparison with C_{gap}, but Fig. 2.17 displays the result of Eqs. 2.5 and 2.14 as a function of SW for different slot lengths. It is seen that the surface capacitance is highly significant, and for larger slot widths appears to be greater than C_{gap}, although the models presented here are not necessarily accurate for large values of SW, as will be discussed. The surface capacitance at a point on the inner surface of the ring is defined as the surface charge σ divided by the voltage V between the point of interest and one diametrically, or symmetrically, opposite:

$$C_{surf} = \frac{\sigma\left(\theta\right)}{V\left(\theta\right)} \tag{2.7}$$

where θ is the angle taken from the centre of the slot. The total surface capacitance, per unit height, is then given as:

$$C'_{surf} = \int_{\theta_S}^{\pi} \frac{\sigma\left(\theta\right)}{V\left(\theta\right)} r d\theta \tag{2.8}$$

where the limit θ_S defines the angle between the slot centre and edge as shown in Fig. 2.15, and the total angle resultant from the size of the slot is $2\theta_S$. The electric field of an infinitely long cylinder with a slot of $SW \rightarrow 0$ was examined in [56], and the expressions for σ and V, as reproduced in [51], are given as:

$$\sigma = \varepsilon_0 \frac{V_0}{\pi r} \cot\left(\frac{\theta}{2}\right) \tag{2.9}$$

$$V = \frac{V_0}{\pi} \left(\pi - \theta\right) \tag{2.10}$$

Substituting Eqs. 2.9 and 2.10 into 2.8:

$$C'_{surf} = \varepsilon_0 \int_{\theta_S}^{\pi} \frac{\cot\left(\frac{\theta}{2}\right)}{\left(\pi - \theta\right)} d\theta \tag{2.11}$$

Assuming that θ_S is small, θ may be ignored in the denominator, yielding:

$$C'_{surf} = \frac{\varepsilon_0}{\pi} \int_{\theta_S}^{\pi} \cot\left(\frac{\theta}{2}\right) d\theta = \frac{2\varepsilon_0}{\pi} ln\left(\frac{2}{\theta_s}\right) \tag{2.12}$$

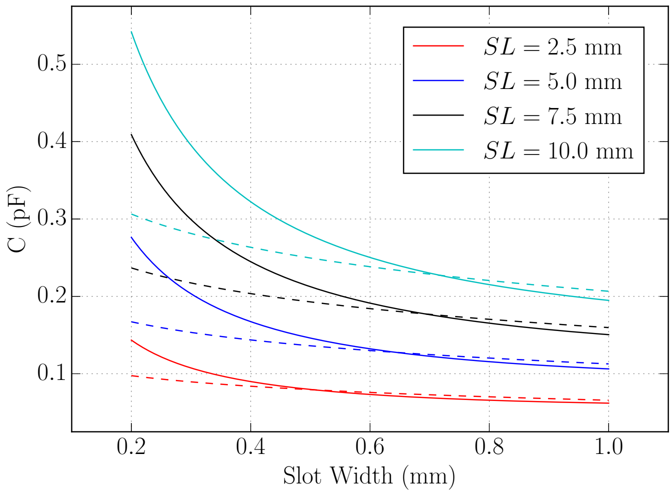

Figure 2.17: Comparison of the gap capacitance (solid) with surface capacitance (dashed) for varying slot width and length.

where the property $\sin(x) \rightarrow x$ in the limit $x \rightarrow 0$ has been used. From Fig. 2.15:

$$\theta_S = \frac{SW}{2r} \tag{2.13}$$

Finally, the total surface capacitance for a sensor of length SL and metal thickness a is given as:

$$C_{surf} = \frac{2\varepsilon_0}{\pi}\left(SL + a\right) ln\left(\frac{4r}{SW}\right) \tag{2.14}$$

The authors in [51] compare the result in Eq. 2.14 with an identical expression derived through conformal mapping. The gap and surface capacitance are in parallel, and so we obtain the total capacitance as:

$$C = C_{gap} + C_{surf} \tag{2.15}$$

Using the expressions for L and C with Eq. 1.25 the resonant frequency of the sensor can be calculated. To assess the accuracy of the presented models, the same dimensions were simulated and compared, where the simulation method will be described in more detail in a later section. First, a comparison between theoretical and simulated results for very small slot widths can be seen in Fig. 2.18, $SL = 2.5$, 5.0 and 10.0 mm, $r = 10$ mm and $a = 1$ mm. For smaller values of SW, the agreement between results is excellent, but begins to deteriorate as the slot width increases, an effect which is more pronounced for larger slot lengths.

Next, we compare the theoretical and simulated resonant frequencies for a sensor of changing metal width a, $SW = 30$ μm and all other dimensions are identical to

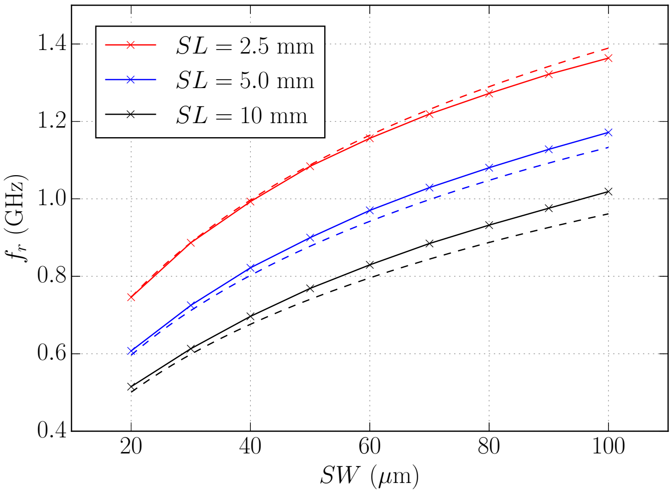

Figure 2.18: Theoretical results (dashed) compared with simulated sensors for varying sensor lengths and slot widths.

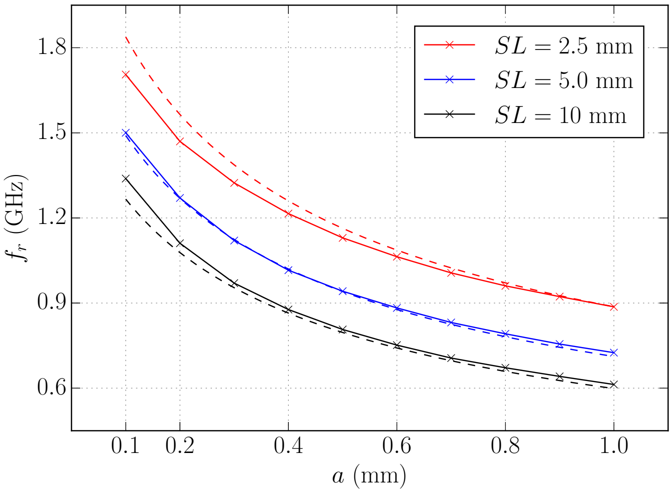

Figure 2.19: Theoretical results (dashed) compared with simulated sensors for varying metal thickness a and sensor lengths.

those used in Fig. 2.18. Again, there is a good agreement for certain parametric combinations but not for others, where we see a particular divergence between theory and simulation for smaller metal widths.

2.2.3 Limitations

The models presented in the previous section agree well with simulations for a given parametric range of sensor geometry, although it is clear that the agreement begins to diverge away from this range. It is in no way unexpected to encounter limitations for approximate models such as these, but it is useful to attempt to define the domain in which they remain accurate, which can be achieved through some basic mathematical

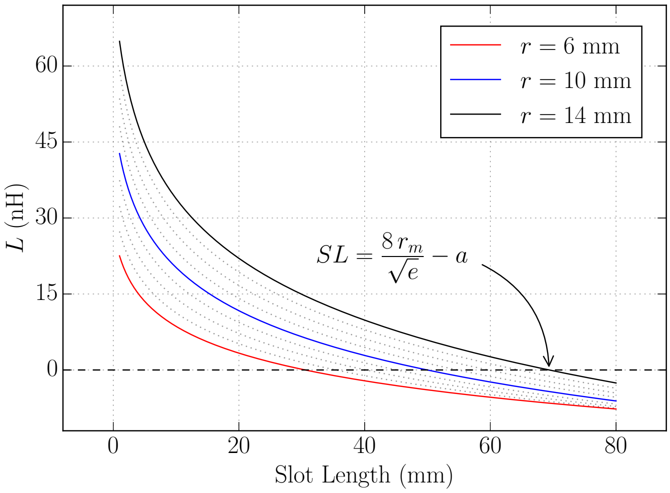

Figure 2.20: Effect of SL on inductance for different radii.

analysis. The sensor inductance given by Eq. 2.2 immediately presents a limit for positive values, where the equation is only valid for:

$$ln\left(\frac{8r_m}{SL + a}\right) > 0.5 \tag{2.16}$$

and so:

$$SL > \frac{8r_m}{\sqrt{e}} - a \tag{2.17}$$

where Eq. 2.17 may be rearranged accordingly for each dimension. For a sensor of $6 \leq r \leq 14$ mm, $SW = 0.5$ mm, $a = 1$ mm and increasing slot length, the inductance is shown in Fig. 2.20. The value of SL at which each curve crosses $L = 0$ is given by Eq. 2.17, which may be used to aid in the selection of dimensions for sensors which require accurate modelling using Eq. 2.2. Clearly this limit should not be viewed as a boundary to valid sets of parameters, but instead signifies the point at which the inductance model is not even mathematically sound.

The expression for the gap capacitance given in Eq. 2.5 contains a correction term C_0 for fringing field effects. As the slot width increases, the first term decreases as one would expect for a parallel plate capacitor, but C_0 increases indefinitely with SW which is certainly not valid. Fig. 2.21 displays the value of C_{gap} for a large range of slot widths and a number of metal widths. The left-hand side of Fig. 2.21 looks reasonable, but the right-hand side suggests that C_{gap} begins to increase once the slot width increases above a given value. The turning point in C_{gap} is found by obtaining its derivative:

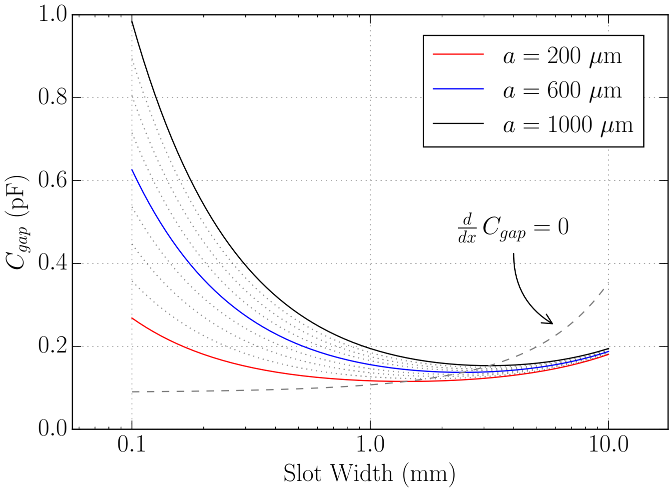

Figure 2.21: Effect of SW on the gap capacitance for different metal widths.

$$\frac{d}{dx}C_{gap} = -\varepsilon_0 \frac{SL \cdot a}{SW^2} + \varepsilon_0 \tag{2.18}$$

equating to zero, and rearranging for SW:

$$SW = \sqrt{SL \cdot a} \tag{2.19}$$

Similarly to the inductance, the result of Eq. 2.19 can be seen by the dashed line in Fig. 2.21, where it has been calculated for a continuous range of metal widths a. Again, limits such as these should only be viewed as a reference and are not intended as rigorous design rules.

The analysis in this section has so far only considered the sensor in free-space, and we may observe the effect of different media by replacing the vacuum permittivity term ε_0 with ε_e, the effective permittivity. The value of ε_e is used to describe the equivalent medium completely surrounding the sensor to represent the inhomogeneous region encountered when a pipe and liquid are present. By replacing free-space permittivity in Eqs. 2.5 to 2.14 with ε_e, we can observe the change in resonant frequency for increasing slot width in Fig. 2.22. It can be seen that this has the expected result, showing a decrease in f_r as the effective permittivity increases. This plot is also used to show the significant disagreement between theory and simulation for all but relatively small slot widths. The effective permittivity was applied to the entire simulation background for these results.

This section has presented a useful set of models for describing the liquid sensor, albeit for a particular range of parameters. Unfortunately, as will become clear in the following sections and chapters, this thesis is concerned with sensor geometry

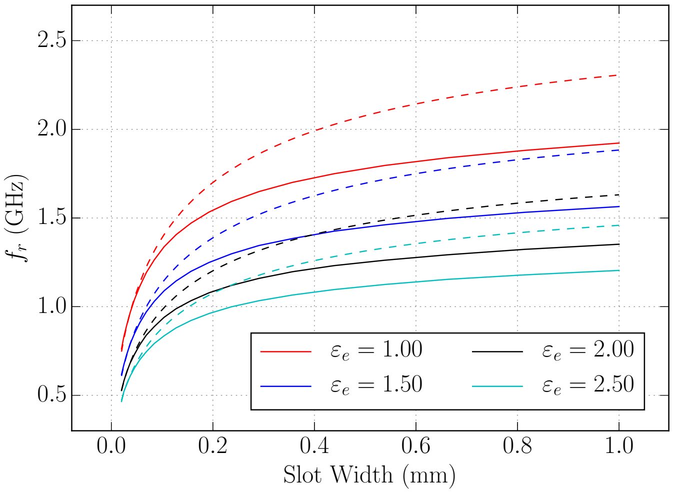

Figure 2.22: Theoretical (dashed) and simulated results for larger slot widths and different media.

Table 2.2: Effect of Parametric Changes on Resonant Frequency f_r

Dimension	Increase	Decrease
SW	$+f_r$	$-f_r$
SL	$-f_r$	$+f_r$
r	$-f_r$	$+f_r$
a	$-f_r$	$+f_r$

which exists within the regions of relatively large disagreement between theoretical predictions and results obtained from simulation and measurement. This section has, however, provided useful insight into the effect of individual dimensions on the resonant frequency of the sensor, where a summary of those effects are seen in Table 2.2.

2.3 Device Simulation

This section aims to cover all relevant aspects of the simulation of the liquid sensor, including an overview of the simulation environment and a parametric study of the device geometry with an associated sensitivity analysis. Additionally, a comprehensive analysis of the structure allows its behaviour to be well understood before proceeding to fabrication and measurement efforts. All simulated results presented in this thesis were obtained using Microwave Studio (MWS), part of Computer Simulation Technology's (CST) electromagnetic software suite. The next section covers details of the simulation environment used for all simulated results.

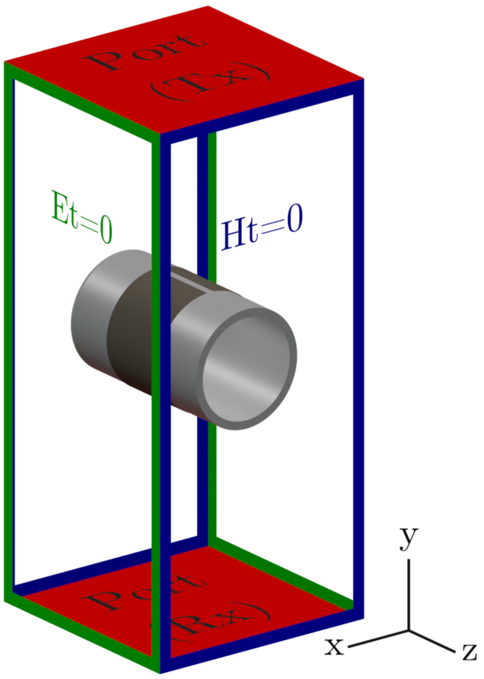

Figure 2.23: Simulation environment, showing a short section of pipe.

2.3.1 Simulation Overview

Excitation of the sensor is achieved *via* an incident plane wave polarised along the x-axis, as shown in Fig. 2.3. The excited plane wave travels downward from the top port along the y-axis, travelling towards the pipe which lies along the z-axis. The incoming and/or outgoing signals at the waveguide ports generate S-parameters which can be used to identify the resonant frequency f_r of the simulated device. MWS allows for a number of different excitation ports, each useful for different scenarios. As we require a plane wave, but also S-parameters, we opt for a waveguide port placed at either end of the simulation domain with the sensor situated in the centre, providing a two-port network. The plane wave can be excited by replacing the boundaries with appropriately placed electric and magnetic walls, where the tangential E and H-fields are 0, respectively. An example of the simulation environment can be seen in Fig. 2.23 for a short section of pipe. The electric boundaries result in electric field lines which may only be normal to that boundary, where the same is true for magnetic field lines and the magnetic boundaries, essentially placing the sensor inside of a parallel-plate waveguide. This transmission line supports TEM waves, where E and H have no component in the direction of propagation, and of which plane waves are a subset.

Due to the imposed conditions, it is necessary to add a small distance between the sensor and the boundaries to avoid any significant perturbation of the resonant

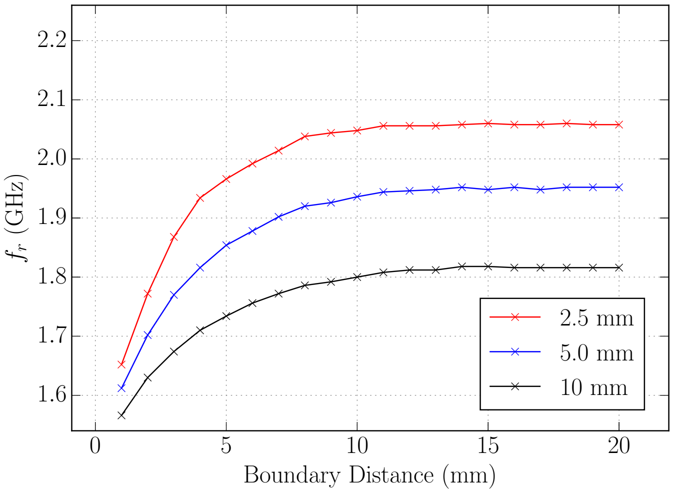

Figure 2.24: Effect of the boundary distance on simulated resonant frequency for different slot lengths.

field, which would alter the resonant frequency of the sensor. Fig. 2.24 shows the effect of increasing the boundary distance from the sensor, from 1 to 20 mm and for various slot lengths. It is clear that for very small distances f_r changes rapidly, as is to be expected due to interaction between the excited field and boundaries, but quickly reaches a near-constant value after around 12 mm. The similar behaviour shown for a larger SL suggests that there is a negligible impact of increasing the overall sensor size on the effect of boundary proximity. The boundary distance is set to 20 mm for all simulated results, where any further increase is not necessary and also introduces spurious resonances within the simulation domain.

To demonstrate typical S-parameters obtained from the sensor, results from a simulation using arbitrary dimensions and for normalised frequency can be seen in Fig. 2.25. At resonance, the excited sensor radiates energy back towards port 1, resulting in a high reflection. Additionally, the energy reflected towards port 1 does not enter port 2, and so a low transmission is observed at resonance. The maximum magnitude of either result is sufficient to identify the resonant frequency of the simulated sensor. It should be noted that S_{12} and S_{22} are not included in Fig. 2.25 due to being essentially identical ($\Delta S < 6 \times 10^{-4}$), suggesting that the axial orientation of the sensor with respect to the incoming plane wave excitation is not important, which will be discussed further in the next chapter. Additionally, the simulation does not consider a pipe or liquid and the sensor is considered as a perfect electric conductor (PEC), consequently the result displays no dielectric or conduction losses.

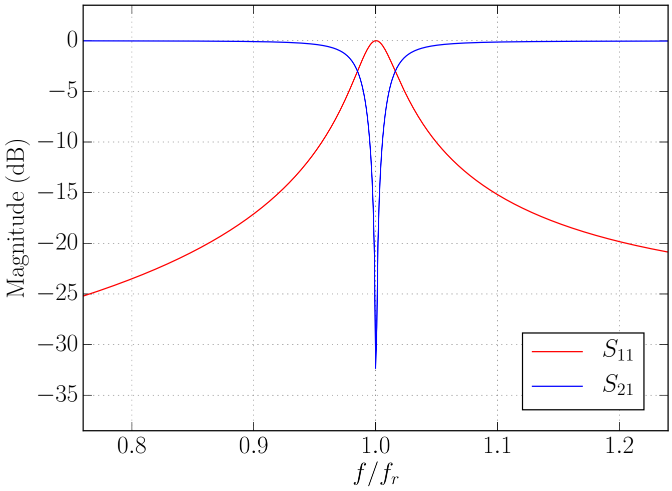

Figure 2.25: Comparison of S_{11} and S_{21} for an arbitrary sensor and normalised frequency.

Meshing

Discussion of the surface current shown in Fig. 2.9 referenced simulation discretisation, suggesting it as a cause for the noisy element of the plot. MWS relies on the application of the finite integration technique (FIT), requiring that the simulated model be transformed into a mesh consisting of a (usually large) number of parts, or cells. The discretisation of the model can be achieved using a hexahedral or tetrahedral mesh, which are both automatically generated within MWS. A hexahedral mesh consists of cuboid-like cells with 6 vertices, and a tetrahedral mesh features cells of 4 vertices with triangular faces. Historically, a hexahedral mesh would have been unsuitable for curved geometry as it generates cells directly aligned with Cartesian coordinates, though recent advances (such as CST's perfect boundary approximation) overcome this problem. Nonetheless, a tetrahedral mesh will generally require less mesh cells, and therefore solver time, to adequately discretise a curved structure. The simulations begin with an initial mesh of 4 cells per wavelength and adaptively discretise based on the electrical behaviour throughout the model.

For the cylindrical structure of the proposed sensor, a curvature limit may be defined to control the minimum angle of consideration for the mesh computation, where a lower limit will result in a greater number of mesh cells. To find the appropriate compromise between simulation accuracy and solver time, the curvature limit was decreased from 45° to 5°, where the solver time for 4 passes and resonant frequency for each limit can be seen in Table 2.3. It should be noted that the times listed here are for simulations of an air-filled pipe, those with liquids of higher permittivities can be considerably higher due to the finer mesh required to account

Table 2.3: Effect of Tetrahedral Mesh Curvature Limit

Limit	Time (s)	f_r (GHz)
45°	6	2.150
35°	7	2.152
25°	8	2.150
15°	10	2.154
5°	23	2.156

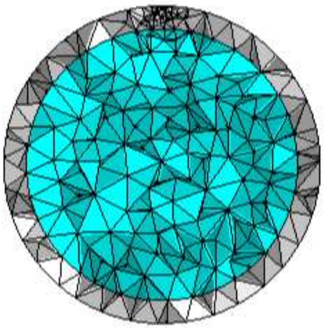

Figure 2.26: Cross-sectional view of an example tetrahedral mesh generated by MWS.

for smaller wavelengths in the LUT. In order to find a compromise between accuracy and solver time, the limit was set to 10° for all subsequent simulated results. For comparison, the total time taken for 4 simulation passes using a hexahedral mesh was 513 seconds, or just under 9 minutes. The resonant frequency was found to vary by 44 MHz and reach a value of 2.01 GHz by the 4$^{\text{th}}$ pass, over 150 MHz lower than the tetrahedral result. In addition to lower solver times, the simulated values of f_r using the tetrahedral mesh are much closer to measured values, as discussed later. An example of the generated mesh can be seen in Fig. 2.26. The non-uniform nature of the model discretisation suggests that different geometry or materials may produce relatively varied mesh structures, even for geometrically similar sensors, such as a small change in the slot width dimension. As such, a small variation in results is to be expected though should not deviate from trends too greatly, where results in this chapter often feature algorithmically-fit curves that rely on such small deviation.

Model Simplification

Any electromagnetic simulation or model requires that some limit be placed on its complexity, which is most often a trade-off between accuracy and simulation time. The sensor presented here is no exception, where highly accurate, time-consuming simulations are not necessarily required or justified, hence the curvature

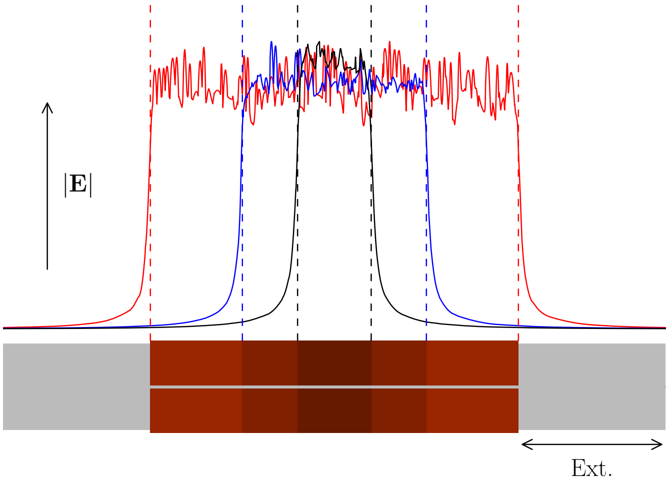

Figure 2.27: Electric field magnitude along the slot axis for different slot lengths.

limit discussed previously. As will be explained in more detail in section 3.2, the sensor structure is difficult to reproduce consistently using the methods available to this project, and measurements can be slightly varied for two sensors of the same geometry. Although the difference between measured results is relatively small, it is still larger than those incurred by the time-saving model simplifications detailed in this section, and as such their use is justified.

With reference to Fig. 2.2, the sensor consists of a pipe with a split metal ring of finite thickness. In reality, the sensor is constructed using an etched Mylar [1] film, where the copper cladding and film widths are 35 μm and 125 μm, respectively. For most practical sensors used in this thesis, the value of SL is often greater than 25 mm, and the pipe radius r is 7 mm, orders of magnitude greater than the film dimensions. The quality of the mesh is reduced when there is an increase in the ratio between the largest and smallest model dimension, and modelling the film introduces very small dimensions for which MWS produces warnings. Simulations of the same sensor with $a = 35$ μm and $a = 0$ differed by 10 MHz at around 2.1 GHz, showing very little change, and therefore all subsequent simulated results feature an infinitely thin PEC metal layer. The Mylar film itself presents less of a problem due its larger size relative to the metal layer, but can still introduce mesh errors or inconsistent discretisation. Comparing simulations with and without the Mylar layer for the same sensor of $r = 7$ mm and resonant at 2.1 GHz, we see a decrease of around 30 MHz when the film is included, essentially resultant from the 125 μm increase in r. This effect is understandably lessened for larger radii, and *vice versa*, due to the percentage change in r. One final consideration is that of the total size

---

[1] Polyethylene Terephthalate (PET), $\varepsilon_r \approx 3.1$.

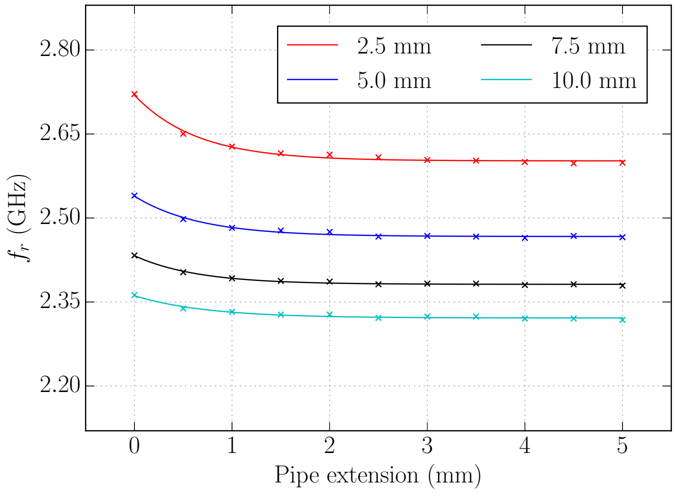

Figure 2.28: Effect of pipe extension on f_r for different sensor lengths.

of the PTFE pipe included in simulations, where in reality the experimental pipes are around one metre in length and this would clearly be impractical to simulate. Truncation of the pipe should not have an effect on the resonant frequency of the sensor if it is to be a valid model simplification, and the fringing field perturbation should therefore be considered. Fig. 2.27 shows the normalised simulated electric field magnitude extracted along the centre of the slot, extending beyond the sensor, for three different slot lengths. The field magnitude is seen to be constant along the slot, ignoring embedded discretisation noise, and decreases exponentially beyond the sensor cavity, where the dashed lines identify the edge of each sensor. It is worth noting that this result agrees with the behaviour of the sensor as a waveguide at cut-off as discussed earlier, where the phase constant β is equal to 0 in a waveguide at f_c, resulting in no phase variation of the excited mode along the slot. Given the rapid decay of field magnitudes beyond the sensor cavity, only a small section of pipe should be required to extend beyond this point to avoid any significant perturbation. For different values of SL, the effect of increasing the pipe extension (shown in Fig. 2.27) on the simulated resonant frequency is displayed in Fig. 2.28. It is seen that only a small extension is necessary in order to achieve a constant f_r, and so a value of 10 mm is applied to all subsequent simulated models.

The model simplifications are applied in an attempt to significantly decrease simulation time, as indeed they do, and are justified due to inherent issues in comparing simulated and measured results to any great degree of accuracy. They have been discussed here to demonstrate no great impact on sensor characterisation, where any other outcome would invalidate their use. Despite simplification of the modelled sensor, simulations are able to display effects and trends of parametric changes, which forms the basis of the next section.

2.3.2 Parametric Study

This section aims to cover all relevant properties of the liquid sensor through a comprehensive parametric study and associated sensitivity analyses. Relevant theory covered in section 2.2 displayed some brief analysis of various dimensions, but limitations in the theoretical models prevented further study of larger sensors, as is the nature of many of the fabricated devices in this thesis. The dimensions studied in this section are intended to be generally realisable with simple fabrication techniques, allowing for reasonable comparison with measured results. Unless otherwise stated, all simulations use a PTFE pipe of $r = 7$ mm and $d = 1$ mm, to represent the experimental pipes used in later chapters. A large amount of simulated data is included in this section, covering a great many sensor geometries of differing dimensions. There is no particular importance placed on absolute values such as f_r and Q, where instead this study intends to present relative behaviour and the general impact of various dimensions on sensor behaviour.

Slot Width

The sensor slot width SW perhaps presents the simplest way to adjust the resonant frequency of the liquid sensor, due to the fixed values of r, a and d for a given measurement environment, potentially including SL if size constraints are of concern. From Figs. 2.18 and 2.22 it is clear that small changes in SW, especially for smaller slot widths, cause a relatively large change in f_r in comparison with other dimensions. With reference to Eqs. 2.5 and 2.14 we see that the total capacitance C decreases with increasing slot width, resulting in an increase in f_r. Additionally Eq. 2.3 suggested a correction to the inductance model in Eq. 2.2 which includes slot width effects, showing a decrease in L with increasing SW. Therefore, an increase in SW results in a decrease in both L and C simultaneously, causing a relatively large shift in resonant frequency, which increases with slot width. This behaviour was displayed in Figs. 2.16, 2.18 and 2.22, and without the limits of theoretical models, it is possible to simulate much larger slot widths.

Fig. 2.29 displays the simulated S_{11} magnitude for increasing slot width, where $0.2 \leq SW \leq 3.0$ mm and $SL = 2.5$ mm, note that pipe losses are not included. The result shows the expected behaviour, where f_r increases with slot width, to a lesser extent as SW becomes larger. It is immediately clear that larger slot widths display a reduced Q-factor. Taking the value of Q as defined in Eq. 1.20, the effect of SW

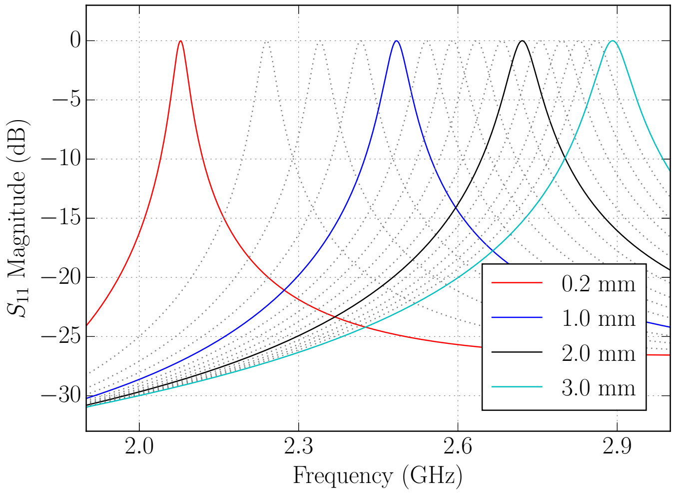

Figure 2.29: Effect of the slot width on the simulated S_{11} magnitude for $0.2 \leq SW \leq 3.0$ mm in 0.2 mm increments, $SL = 2.5$ mm.

on the Q-factor of the simulated S_{11} response is shown in Fig. 2.30. The value of Q falls sharply for small slot widths, and continues to do so as SW increases, where it can be seen that very small slots would have a significantly higher Q-factor. However, as previously stated, this section is concerned only with practical dimensions. The result shown by Fig. 2.30 aids in the selection of an appropriate value for SW, where it should not be so large that the value of Q is reduced too greatly. It should be noted here that the absolute value of Q is not of particular importance, where it can be influenced by the simulation domain. Instead, we are interested in its behaviour with respect to another variable to ascertain whether changes in certain dimensions improve or reduce Q, and to what extent. This thesis does not intend to use calculated Q-factors as a measurement metric, but generally aims to avoid its reduction where possible, as a higher Q response offers improved resolution and resistance to noise.

The effect of fringing fields was discussed in section 2.2 with reference to Fig. 2.14, which showed some arbitrary slot widths along with examples of the resultant field lines extending into the sensor cavity. For larger values of SW, it is expected that the resonant electric field penetrates the liquid cavity more extensively than for smaller slots, and is therefore more perturbed by the liquid present in the pipe. It follows that a sensor which features a larger slot will result in a resonant frequency more sensitive to changes in ε_r due to increased perturbation. In order to quantify this effect to some extent, we may extract the magnitude of the electric field along a path within the sensor cavity, which starts at top of the pipe in the centre of the slot, and travels downward to the middle of the cavity as shown by the diagram

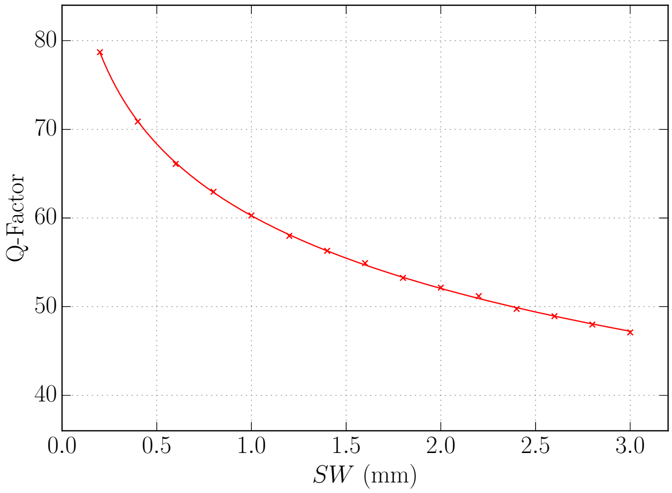

Figure 2.30: Effect of the slot width on Q, $SL = 2.5$ mm.

in Fig. 2.31. The added effect of the pipe material complicates the field plot due to inhomogeneity and so is neglected for this simulation, but analysis of the pipe material and wall width will discuss an equivalent simulation later in this section. The value Δy refers to the position along the path, where $\Delta y = 0$ and 7 mm are the top and centre of the pipe cavity, respectively. For slot widths of $0.2 \leq SW \leq 2.0$ mm the magnitude of the electric field, sampled at the relevant resonant frequency, was extracted along the path in Fig. 2.31, where Fig. 2.32 displays the normalised results. There is a very clear decrease in the rate of field decay within the sensor cavity as SW increases, where the resonant field magnitude for $SW = 0.2$ mm is reduced by over 90% during the first 1 mm of the cavity. It is also interesting to note, although difficult to see, that the maximum observed field strength moves slightly further along the path as SW increases, which is explained by the change in vertical position of the slot edges, see Fig. 2.14.

The effect of slot width on the sensitivity of the sensor to changes in the LUT ε_r can be assessed by adjusting the permittivity of the liquid cavity. However, it was briefly mentioned in section 2.1 that the pipe wall acts to move the liquid cavity away from the slot by a distance equal to the wall width d. Additionally, the rates of decay in Fig. 2.32 show that a small distance, such as d, may have a significant effect on field perturbation and therefore the sensitivity of the sensor. Finally we consider that a sensor suspended in free-space containing a LUT is impractical, and for all of these reasons the pipe should be included in an analysis of sensitivity, as otherwise an unrealistic performance may be reported. With the PTFE pipe placed inside of the sensor cavity, where $d = 1$ mm, the permittivity of the liquid cavity was varied between 1 and 32 for different slot widths, and the simulated f_r values are shown in

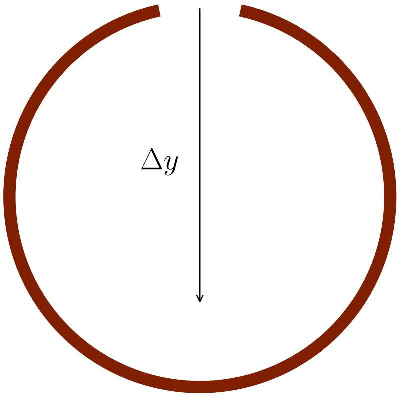

Figure 2.31: Diagram of the path along which the field strength is analysed in Fig. 2.32.

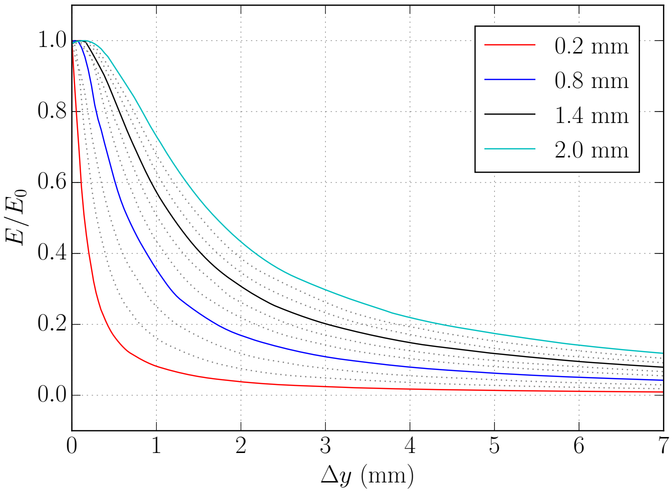

Figure 2.32: Normalised field magnitude for $0.2 \leq SW \leq 2.0$ mm, in 0.2 mm steps, along the path shown in Fig. 2.31.

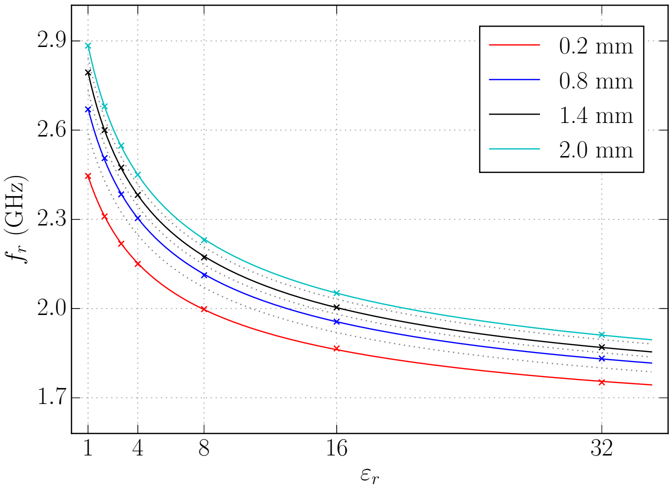

Figure 2.33: The effect of the LUT ε_r on f_r for $0.2 \leq SW \leq 2.0$ mm, in 0.2 mm steps.

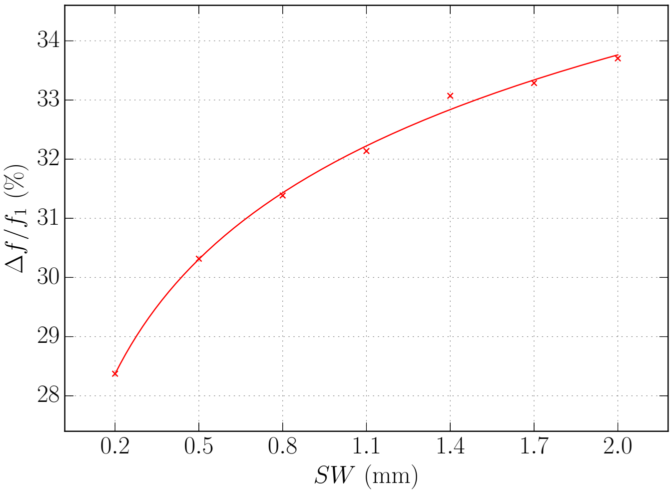

Figure 2.34: Effect of slot width on sensor sensitivity.

Fig. 2.33. A quick assessment of the curves does not reveal a great deal of change in the sensitivity for different values of SW. We may take the total frequency change Δf over the permittivity range and normalise it against the initial resonant frequency f_1 when $\varepsilon_r = 1$ to obtain a percentage change, providing a quantitative assessment of the sensitivity of each SW to changes in ε_r. The result of these calculations are fit to a curve and plotted in Fig. 2.34. There is certainly an increase in the sensitivity to changes in liquid permittivity, although given the relatively large range of slot widths it is not overly significant. Rather than offer an advantage to using larger values of SW, such as vastly improved sensitivity, Fig. 2.34 perhaps displays that a smaller slot is almost equally as sensitive while still retaining a comparatively high Q, as seen in Fig. 2.30.

Slot Length

The slot length SL, as shown in Fig. 2.2, is the total length of the sensor and therefore the slot. It provides a way to adjust the physical size of the sensor for a given measurement environment, where *in situ* pipes are of a fixed radius. The theoretical analysis in section 2.2 showed that the sensor inductance decreases with increasing SL, as described by Eq. 2.2 and displayed in Fig. 2.20. Conversely, Eqs. 2.5 and 2.14 both show an increase in capacitance with an increase in slot length, as shown by Fig. 2.17. Due to the opposing effects on L and C, the total change in resonant frequency for a given change in SL is much less than for the slot width, where a very high sensitivity to small changes is displayed in Fig. 2.29. The change in physical size has particular implications for wireless measurements, where a larger sensor will reflect a greater portion of the incident signal.

The slot length was varied from 2.5 to 25 mm in 2.5 mm increments, and the simulated S_{11} magnitude can be seen in Fig. 2.35. It can be seen that increasing SL decreases the resonant frequency as expected, and relatively large changes in the slot length are necessary in order to achieve the same change in f_r as observed with SW. The Q-factor appears to decrease with increasing SL, and indeed this is shown by Fig. 2.36. Similarly to Fig. 2.33, the liquid ε_r was adjusted from 1 to 32 for slot lengths of 5, 10, 25 and 100 mm, and the result is shown in Fig. 2.37. Unlike the slot width, SL appears to have no particular impact on the sensitivity of the sensor to changes in LUT permittivity, and using the same method of $\Delta f/f_1$ to asses sensitivity, the results showed no trend. This is not surprising, as Fig. 2.4 displayed plots of the excited electric field magnitude which was seen to be constant along the length of each slot, suggesting that adjusting the slot length has no effect in terms of field perturbation within the sensor cavity.

The effect of the slot width on f_r for a number of different slot lengths is shown in Fig. 2.38, and it can be seen that the larger sensors appear to be more sensitive to changes in SW. Taking the sensitivity again as a percentage change in the initial resonance f_1 when $SW = 0.2$ mm, Fig. 2.39 displays the result. This behaviour was in fact shown previously in Fig. 2.17, which plotted the modelled capacitance $C = C_{gap} + C_{surf}$ against SW for a number of slot lengths, showing a similar increase in sensitivity to slot width for longer sensors. The effect is partially attributable to the first term of C_{gap} in Eq. 2.5, which shows that a larger value of SL will result in a greater range of capacitance values for a given range of SW. This is perhaps relevant if a high level of accuracy is required in terms of f_r, where shorter sensors will be more resistant to changes in slot width caused by fabrication tolerances or

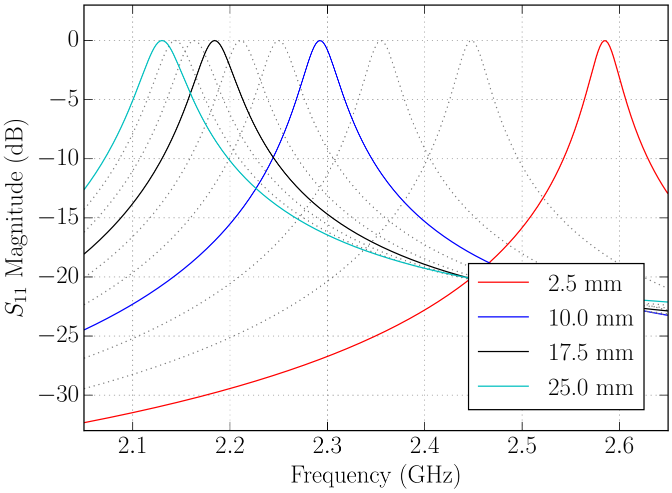

Figure 2.35: Simulated S_{11} magnitude for various slot lengths.

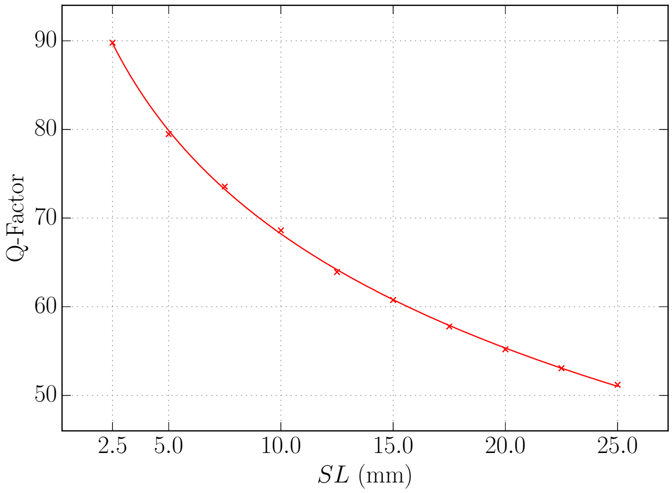

Figure 2.36: Effect of slot length on the Q-factor.

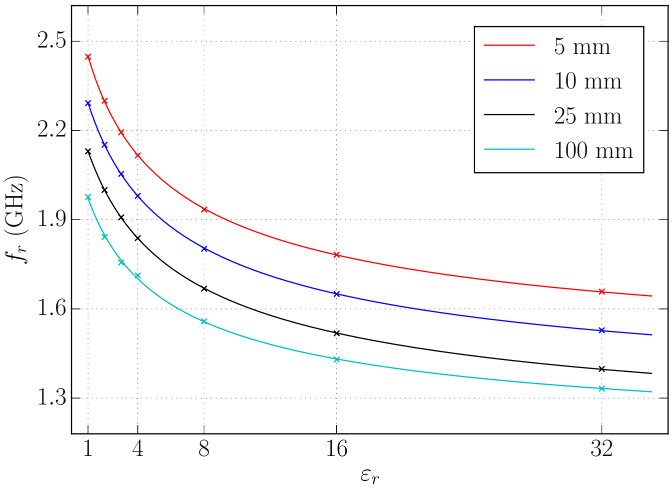

Figure 2.37: The effect of the LUT ε_r on f_r for different slot lengths.

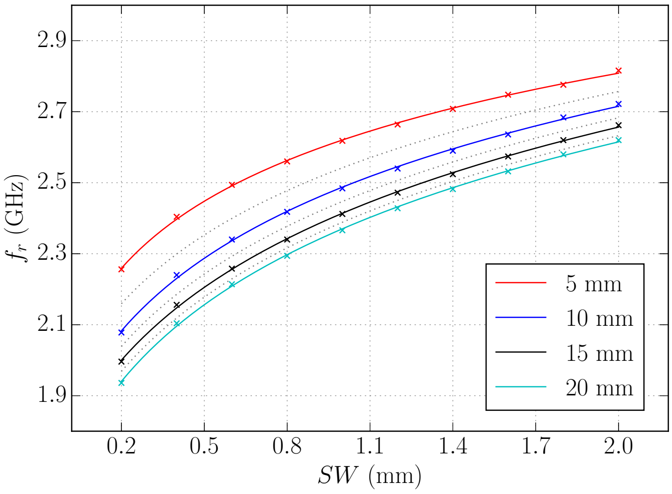

Figure 2.38: Effect of SW on f_r for a number of slot lengths.

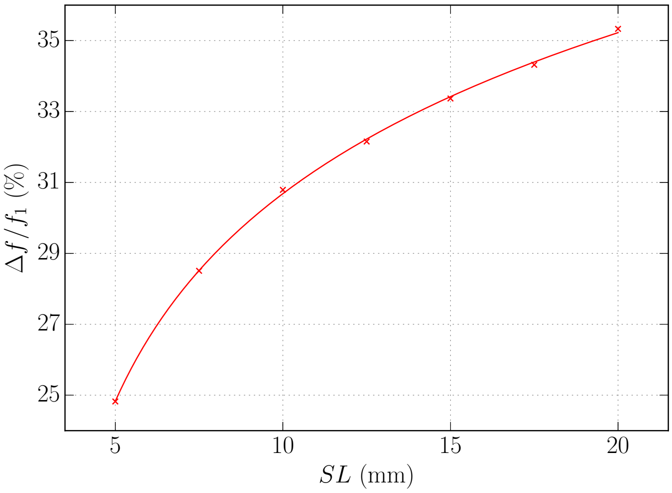

Figure 2.39: Sensitivity to SW for different slot lengths, from Fig. 2.38.

errors.

The physical size of the sensor directly impacts the amount of power which it reflects, and given that this reflection, or scattering, is used by the receiving antenna to perform measurements, it is essential that enough power is reflected by the liquid sensor. One metric used to assess the amount of power reflected is the radar cross-section (RCS) which, simply put, provides a measure of how well an object reflects an incident wave towards its source, where a low RCS suggests minimal scattering in the direction of the transmitting antenna, such as would be desirable for a stealth jet [57]. Using a field probe, the simulated RCS at f_r for a large range of slot lengths is shown in Fig. 2.40. The result shows a very clear and significant increase in the level of reflected power as SL increases, where the RCS increases by around 20 dB from $SL = 2.5$ to $SL = 200$ mm. A larger slot

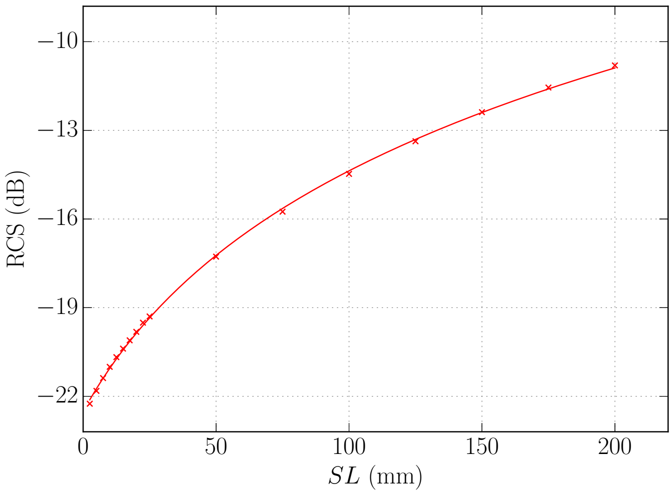

Figure 2.40: Simulated radar cross-section for increasing slot length.

length results in a greater effective aperture A_e over which the sensor can capture and re-radiate incident waves, increasing the power of reflections at resonance. It is true that the RCS also increases away from resonance simply as a result of a larger metal area, but not at a rate greater than at f_r. It would seem sensible to opt for a much larger sensor in order to maximise the level of reflection and therefore improve measurement clarity. However we note from Fig. 2.36 that Q decreases with increasing slot length, and this should be taken into account when attempting to improve the sensor response. Additionally, there are a number of practical considerations for larger sensors related to fabrication and measurement configurations, discussed later in sections 3.2 and 3.3.4, respectively. For this reason, the majority of sensors considered in this thesis have a length $SL < 50$ mm, although improved fabrication techniques may be capable of mitigating some of these issues.

Radius

The sensor radius r is more likely than not to be defined by the *in situ* pipe on which the proposed liquid sensor is placed, which is why the slot length and width are important to study comprehensively, as they offer a method to tune f_r without the installation of new pipes. Despite the potential lack of control over r, it has a very significant impact on the resonant frequency of the sensor, as well as its Q and physical size. The sensor radius is directly proportional to L, as shown by Eq. 2.2, and the surface capacitance described by Eq. 2.14 also increases with r.

The effect of pipe radius on the simulated S_{11} magnitude is seen in Fig. 2.41, where $6 \leq r \leq 12$ mm and $SL = 2.5$ mm. The pipe wall-width d maintained the same ratio to r, where $d = r/7$ to agree with the PTFE pipe used in measurements.

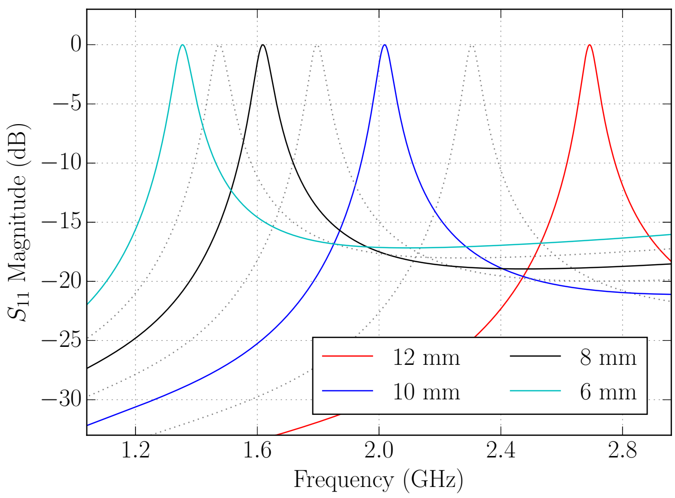

Figure 2.41: Simulated S_{11} magnitude for different pipe radii.

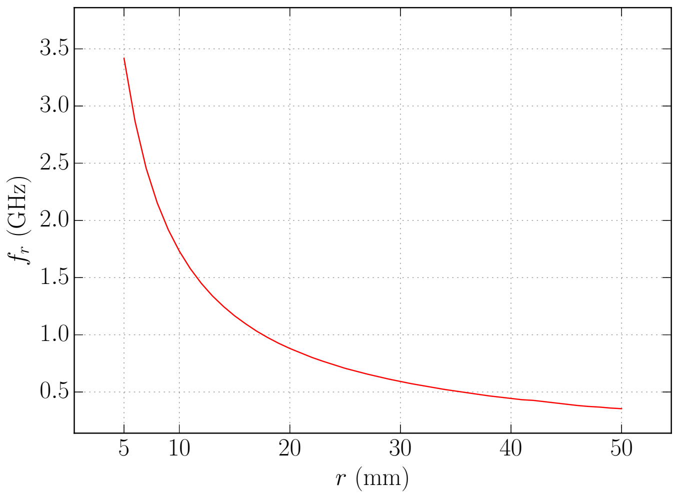

Figure 2.42: Simulated f_r for a large range of r.

A relatively large decrease in f_r as r increases is clearly seen, as expected, due to the simultaneous increase in L and C with increasing r. Fig. 2.42 shows the simulated resonant frequency over a much larger range of radii, where $5 \leq r \leq 50$ mm. For a radius of 2 mm, not shown in Fig. 2.42, the sensor is resonant at around 8 GHz, suggesting that higher frequency operation could be realised through the use of much smaller pipes, and that relatively large pipes may also be viable for the proposed sensor geometry. Additionally, there is an increase in the Q-factor of the S_{11} response as the radius grows smaller, where the calculated Q values are shown by Fig. 2.43, along with a curve fit between $r = 4$ and 14 mm.

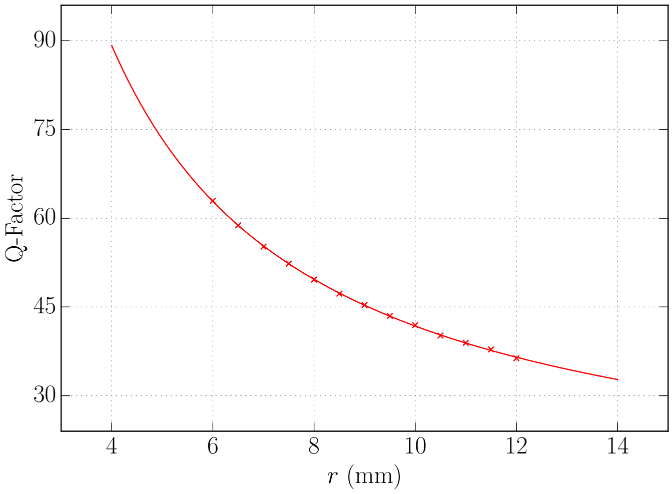

Figure 2.43: Effect of pipe radius on the Q-factor.

Pipe Material

The selection of a pipe material perhaps considers pragmatism before performance, given the issues inherent in its contact with potentially hazardous or corrosive liquids. It is imperative that the material is highly chemically resistant to a wide range of liquids, to avoid the obvious degradation of the pipe but also the contamination of any LUT caused by even light corrosion of the interior pipe walls. It is clear that as the permittivity of the pipe material increases the resonant frequency of the sensor will decrease, as is the case for any liquid present. The simulated resonant frequency for a range of liquid permittivities ε_r and pipe permittivities ε_p can be seen in Fig. 2.44. As expected, an increase in ε_p results in a decrease in f_r for any liquid, as the effective permittivity of the inhomogeneous region within the sensor cavity is subject to an increase with ε_p, regardless of ε_r.

It is also important that the material is as low-loss as possible, where any increase the pipe loss will reduce the Q-factor of the sensor, which may already be relatively low when monitoring high-loss liquids. Fig. 2.32 displays the normalised electric field magnitude along the path shown in Fig. 2.31, but neglects the pipe effects. For liquids of permittivity $1 \leq \varepsilon_r \leq 64$ and $d = 1$ mm, the normalised field magnitudes extracted along the same curve, this time including a pipe of $\varepsilon_p = 2.1$, can be seen in Fig. 2.45. It is seen that the electric field strength is reduced by over a half before reaching the LUT, and for higher permittivity liquids the field magnitude at the pipe-liquid boundary is considerably lower. The reduction in the field strength as it extends across the pipe wall is useful in illustrating the importance of a low-loss pipe material, where high losses present in this region will have a significant effect on the resonant field. For a pipe of $d = 1$ mm and $\varepsilon_p = 2.1$, the effect of the

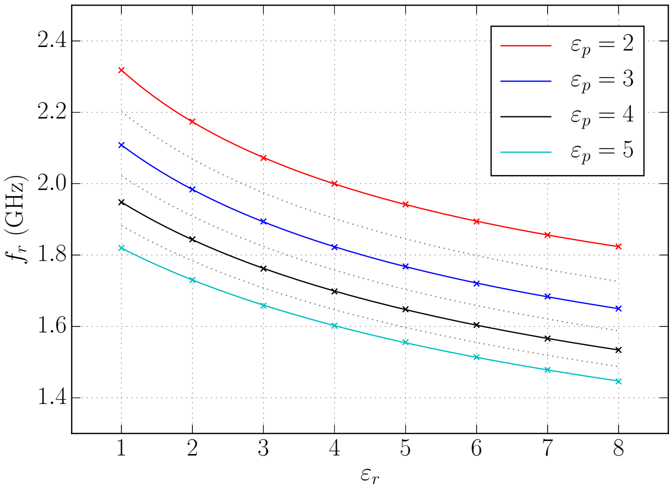

Figure 2.44: Effect of LUT permittivity ε_r on f_r for varying pipe permittivity ε_p.

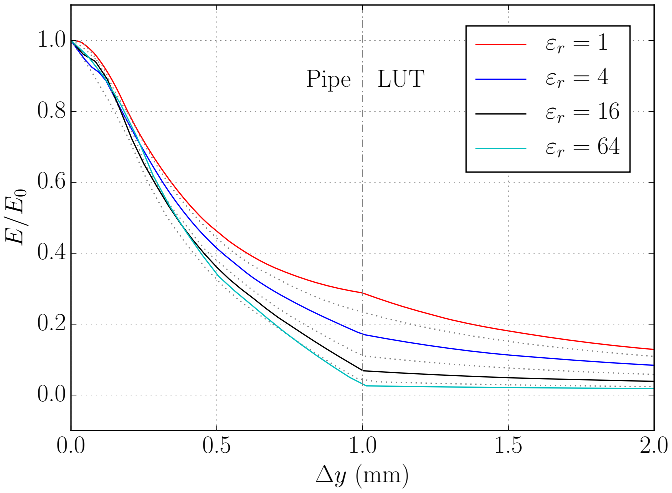

Figure 2.45: Normalised field magnitude along the path shown in Fig. 2.31 for varying ε_r and including pipe effects.

loss-tangent $\tan\delta$ of the pipe material on Q is shown in Fig. 2.46, where we see that even relatively low losses result in a significant reduction of the Q-factor of the S_{11} response. As mentioned in section 2.1 all pipes used in this thesis are constructed of PTFE, where $\varepsilon_p = 2.1$ and $\tan\delta = 0.0005 \pm 0.0002$ [50]. The difference in the peak S_{11} amplitude between a lossless and PTFE pipe was around 0.05 dB in simulations, which is considered negligible.

Pipe Wall Width

The thickness of the pipe wall, as shown in Fig. 2.2, results in the separation of the slotted region and the liquid cavity by a distance equal to d. As has been mentioned previously, this acts to reduce the sensitivity of the sensor due to the reduction in

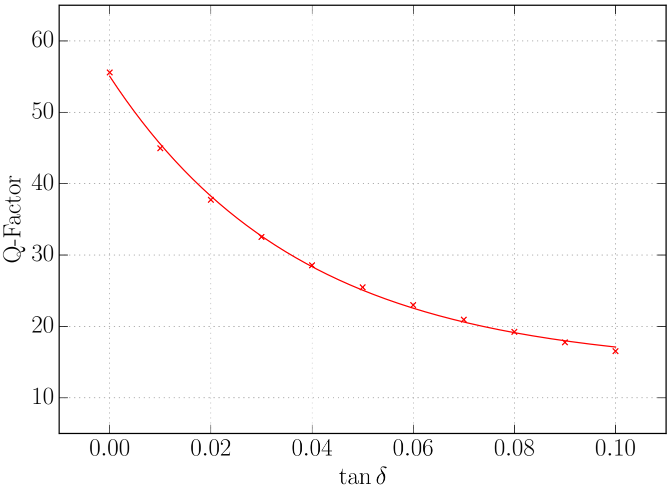

Figure 2.46: Effect of pipe loss tangent on the Q-factor.

perturbation resultant from the liquid within the pipe. We observe a significant reduction in the resonant field strength before it enters the liquid cavity, as displayed by Fig. 2.45. The effect of d on f_r will simply exaggerate the effect shown in Fig. 2.44, as a greater portion of the sensor cavity will be occupied by the pipe walls, thus increasing ε_e. Clearly, the change in resonant frequency with d will be emphasised for smaller values of r due to the increased relative size of the wall width.

For a sensor of $r = 7$ mm, the effect of ε_r on the simulated resonant frequency for a number of wall widths can be seen in Fig. 2.47, where the pipe material is again PTFE. In the case where no liquid is present, the decrease in f_r resultant from the increased effective permittivity in the sensor cavity is observed as d increases. The resonance curves converge at the point where $\varepsilon_r = \varepsilon_p = 2.1$, as the pipe and 'liquid' essentially form a homogeneous material. Over the entire range of permittivity the vastly increased sensitivity of smaller values of d is clearly observed, where the total variation in f_r for $d = 0.5$ mm is over double that of $d = 2.0$ mm. By taking the ratio of the total change in frequency Δf to the initial value f_1, a measure of the sensitivity of f_r to permittivity changes within the liquid cavity is shown in Fig. 2.48 for changing d. The difference is very significant, decreasing from more than 35% to less than 15% over a range of 1.5 mm of change in d.

This control over sensitivity has implications for the monitoring of particular liquids, or permittivities, as d may be adjusted to control the total bandwidth required to measure a given range of ε_r. For example, if a high degree of resolution is desired for the monitoring of liquids across the $2 \leq \varepsilon_r \leq 4$ range, it may be advantageous to place the sensor onto a pipe with as small a wall width as possible, thus increasing the Δf range. Conversely, if the range of permittivity is very large

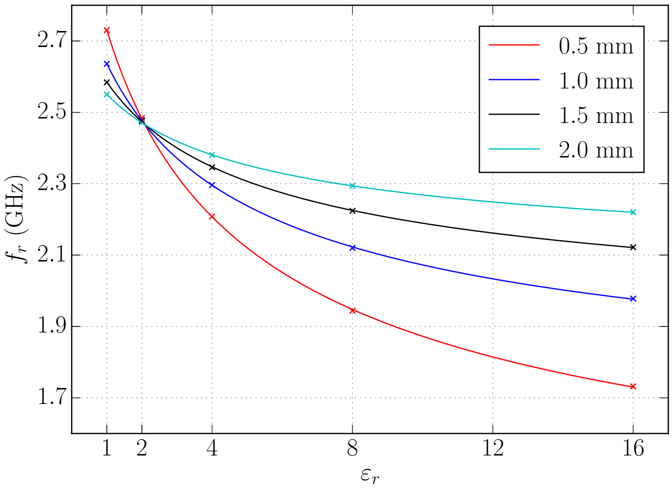

Figure 2.47: Effect of ε_r on f_r for different pipe wall widths.

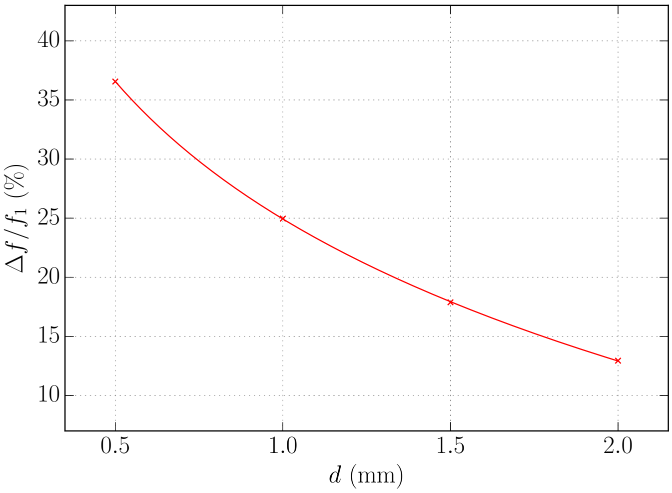

Figure 2.48: Sensitivity to changes in ε_r for changing wall width d.

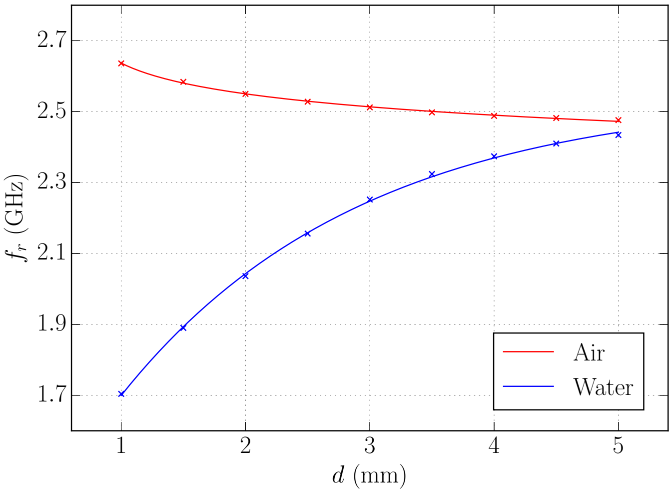

Figure 2.49: Reduction in required bandwidth to measure air and water as d increases.

and we wish to constrict the total bandwidth in order to incorporate the sensors with a narrowband antenna system, the opposite is true and a larger d is desirable. Fig. 2.49 displays an example where two sensors are required to monitor an empty pipe and a water-filled pipe of permittivity $\varepsilon_r = 1$ and 80, respectively. Initially, where $d = 1$ mm, the resonant frequencies of the sensors are separated by around 1 GHz, requiring wideband antennas which operate at almost 50% bandwidth. By increasing the wall width to 5 mm this frequency separation is reduced dramatically to a few tens of MHz, at around 40 MHz.

Metal Thickness

The metal thickness a is modelled as a perfectly thin PEC, as discussed at the beginning of this section, but a brief example of its effect on f_r is shown in Fig. 2.50. The reduction in resonant frequency as a increases is due to its effect on both C_{gap} and C_{surf} shown by Eqs. 2.5 and 2.14, respectively. With reference to Eq. 2.2, an increase in a also acts to decrease L but to a lesser extent than its impact on C, resulting in an overall reduction in LC. A portion of the rationale for replacing a with an infinitely thin sheet was the simplification of the simulation mesh, where small dimensions, relative to the rest of the model, can create difficulties during discretisation. This effect may be observed in Fig. 2.50 as the somewhat noisy distribution of data points, which are seen to be less consistent than those present in the majority of simulation results presented in this chapter.

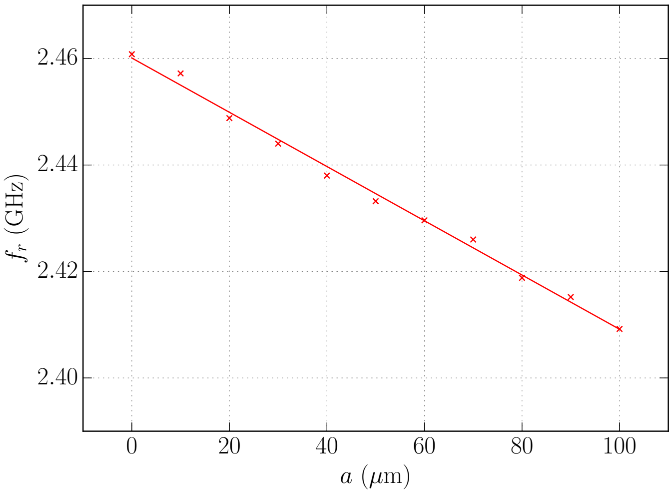

Figure 2.50: Effect of metal thickness a on resonant frequency.

2.4 Conclusion

The proposed liquid sensor geometry shown in Fig. 2.2 intends to satisfy the aims and objectives outlined in section 1.5, in addition to the general idea of non-contact sensing. This chapter has presented a general overview of the sensor, including the principle of operation, plane-wave excitation method and resonant field and current distributions. A brief theoretical analysis is shown, displaying the effect of various geometric parameters on resonant frequency, as well as some limitations of the inductance and capacitance models. Additionally, there is some consideration of the aspects of the split-cylindrical structure which make it difficult to analyse, such as the fringing fields exhibited by larger slot widths. The simulation method and environment is introduced, covering various potential sources of inaccuracy such as boundary distance, pipe extension and meshing constraints. A comprehensive parametric study and sensitivity analysis is presented in section 2.3.2, covering every aspect of the sensor structure. This study provides valuable insight into how the sensor behaviour and performance is impacted by changes in its geometry, and how the device may be adapted to suit a particular measurement environment. A summary of the sensor parameters and their respective effects on f_r and Q observed from simulations is shown in Table 2.4.

From the theory, parametric studies and sensitivity analyses presented in this chapter, it is clear that there are a number variables which can be adjusted to provide satisfactory sensor performance for a wide range of applications and environments. Setting the frequency of operation can be simply achieved by adjusting the slot width and length for a given pipe radius, wall width and material. If a greater response

Table 2.4: Summary of the effect of increasing sensor parameters on f_r and Q.

Parameter	Δf_r	Sensitivity	ΔQ
SW	$+$	High	$-$
SL	$-$	Med	$-$
r	$-$	High	$-$
d	$-$	Med	$+$
a	$-$	Low	n/a
ε_r [1]	$-$	High	$+$
$\tan\delta$	n/a	n/a	$-$

[1] Valid also for ε_p.

amplitude is required, the slot length may be extended to increase the RCS of the sensor. The sensing of liquids which cover a relatively large permittivity range can be reduced in the frequency domain through the use of a pipe with thicker walls, and sensing over a small range of permittivities can utilise thinner walls for greater sensitivity. The sensor presented in this chapter has the advantages of being passive, low-cost, low-complexity and highly versatile and adaptive. By straightforward modification of simple geometry, a wide range of sensors may be produced to fit any number of pipes in a given industrial setting.

Chapter 3

Experimental Results

This chapter will present all of the relevant experimental data required to verify theoretical and simulated results, followed by a number of experiments which measure various liquids. First, the electrical properties of the liquids used in measurements will be examined and characterised, followed by an explanation of the fabrication, measurement process and environment. The selection of liquids for experimental work attempted to cover a broad range of permittivity values, while still opting for those which are easily available and found commonly in industrial applications. All experimental measurements will assess butan-1-ol (henceforth referred to simply as butanol), ethanol, methanol and water, and the electrical properties of each liquid will be discussed in the following section.

3.1 Liquids Under Test

The electrical properties of polar liquids, those that contain permanent dipole moments, can largely be described using Debye relaxation equations. Dielectric relaxation describes the delay in polarisation relative to an applied electric field, as discussed in section 1.3 and in Eq. 1.6. The term τ was introduced to describe the polarisation time of dipoles within a material or liquid, which we now refer to as the relaxation time. We consider a polarised liquid with a static external field applied, where constituent dipoles will generally be aligned with $\mathbf{E}$ resulting in an average dipole moment. Given the instantaneous removal of the external field, dipoles become disordered as a result of random Brownian motion, and the relaxation time τ defines the time taken for the order to reduce by a factor of $1/e$ [58]. In general terms, τ provides a measure of the speed at which the liquid responds to a change in the external field, as alluded to earlier in section 1.3. An approximate expression for τ, assuming a spherical molecule rotating in oil, is given as [58]:

$$\tau = V\frac{3\eta}{kT} \tag{3.1}$$

where V is the volume of the sphere, η is the viscosity of the liquid, $k \approx 1.38^{-23}$ $\mathrm{J\,K^{-1}}$ is the Boltzmann constant and T is absolute temperature. There is perhaps some intuitive interpretation of Eq. 3.1, where a large molecule in a viscous liquid would suggest a slower rotation than the inverse scenario, and indeed, τ is directly proportional to both V and η. The inverse of τ defines the angular relaxation frequency ω_{rel}, at which the dipoles in a liquid attenuate the maximum amount of energy due to rotation, where:

$$f_{rel} = \frac{1}{2\pi\tau} \tag{3.2}$$

It follows that the dielectric loss ε'' reaches a maximum at f_{rel}, where there may be more than one maxima over certain frequency ranges. At relatively low and high frequencies, permittivity becomes effectively constant, where these points are known as the static ε_s and high-frequency ε_∞ permittivity limits, respectively. These terms, along with f_{rel} (or τ), appear in the Debye relaxation equation which describes the complex permittivity behaviour of polar liquids and other dielectrics, and is given by Eq. 3.3. The derivation of this expression is beyond the scope of this thesis, but the method is outlined in [59]. Using several measurement techniques, appropriate over different frequency ranges, tabulated values for the terms in Eqs. 3.3 - 3.5 for various polar liquids at different temperatures are presented in [60] up to 5 GHz. Eq. 3.4 expands on Eq. 3.3 to describe liquids that display two relaxation frequencies, where ε_h refers to the high-frequency permittivity limit above the first relaxation and the τ subscript identifies the first and second relaxation times. For higher frequency second relaxations, Γ is included in Eq. 3.5 to improve the fit to measured data.

$$\varepsilon = \varepsilon_\infty + \frac{\varepsilon_s - \varepsilon_\infty}{1 + j\omega\tau} \tag{3.3}$$

$$\varepsilon = \varepsilon_\infty + \frac{\varepsilon_s - \varepsilon_h}{1 + j\omega\tau_1} + \frac{\varepsilon_h - \varepsilon_\infty}{1 + j\omega\tau_2} \tag{3.4}$$

$$\varepsilon = \varepsilon_h + \frac{\varepsilon_s - \varepsilon_h}{1 + j\omega\tau} - jf\Gamma \tag{3.5}$$

The real parts of the modelled complex permittivities for butanol, ethanol and

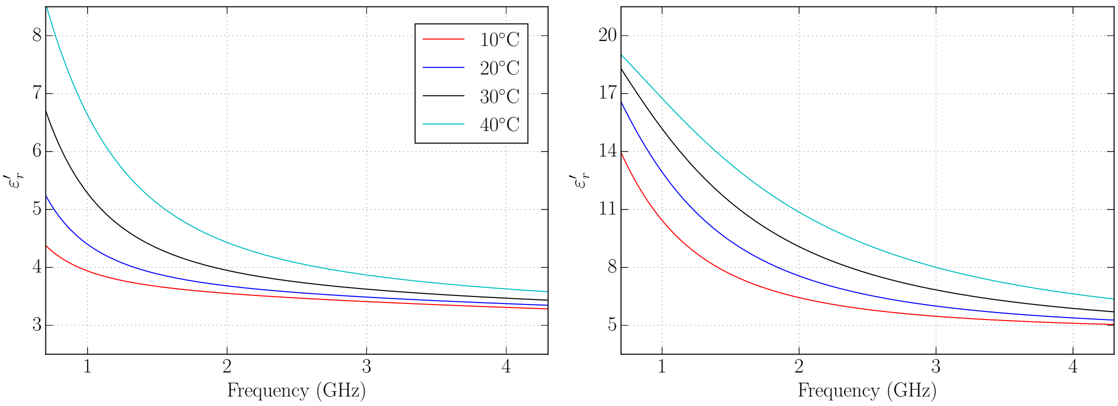

(a) Butanol, Eq. 3.4.

(b) Ethanol, Eq. 3.5.

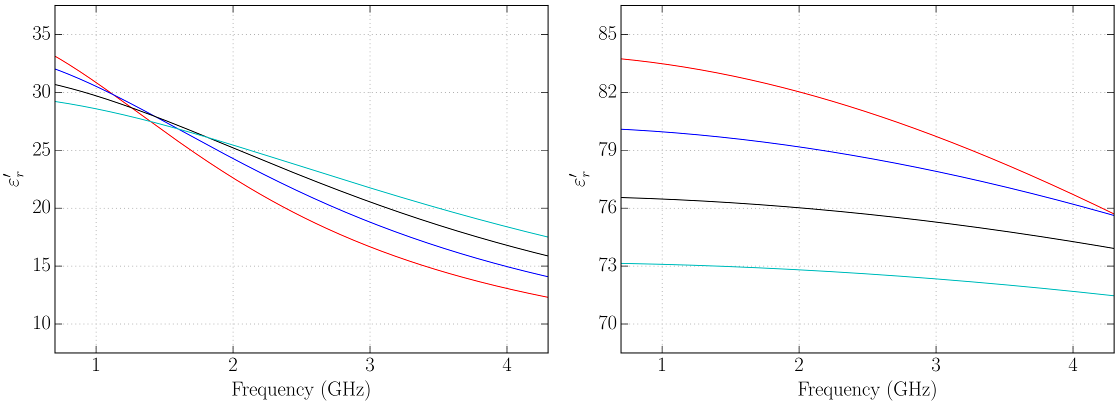

(c) Methanol, Eq. 3.3.

(d) Water, variation of Eq. 3.4.

Figure 3.1: Real part of the permittivity for each alcohol [60] and water [11] calculated from Debye relaxation models.

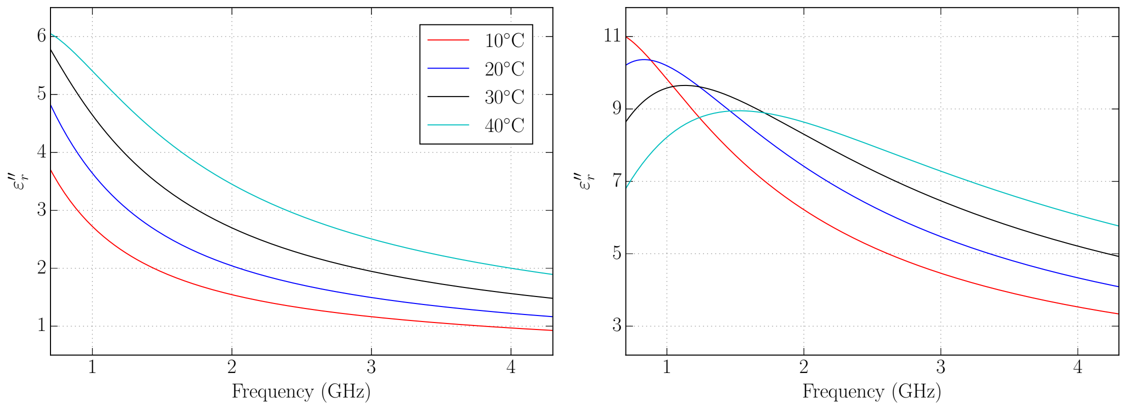

(a) Butanol, Eq. 3.4.

(b) Ethanol, Eq. 3.5.

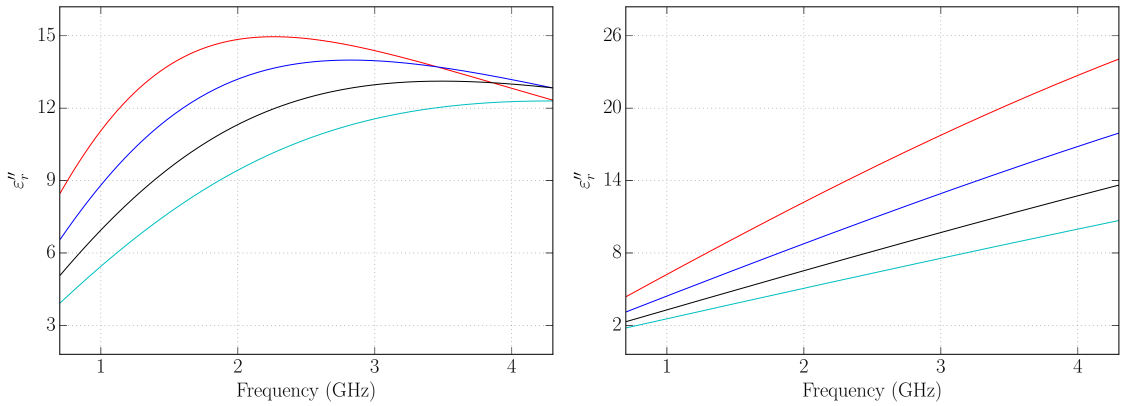

(c) Methanol, Eq. 3.3.

(d) Water, variation of Eq. 3.4.

Figure 3.2: Dielectric loss for each alcohol [60] and water [11] calculated from Debye relaxation models.

methanol can be seen in Fig. 3.1a - 3.1c. The model for water, a variation of Eq. 3.4, was taken from [11], as seen earlier in Fig. 1.7, and is shown in Fig. 3.1d. The liquids display a relatively large range of permittivities which will allow for the assessment of the sensor over a wide frequency range. It is also worth noting that the effect of temperature on ε_r' is not straightforward, especially for methanol, where permittivity initially decreases with increasing temperature at lower frequencies, before reversing this relationship above 1.5 GHz. Across the frequency range in Fig. 3.1, the permittivity of water is seen to decrease with increasing temperature by a seemingly large amount, but Eq. 1.14 shows that this change would not cause as large a change in the resonant frequency of the sensor as the effect of temperature on butanol below 2 GHz would, for example.

From the same models we obtain the imaginary part of the permittivity, or the dielectric loss, for each liquid in Fig. 3.2. The ethanol and methanol plots both show peaks within the frequency range of interest, displaying the relaxation frequency discussed in relation with Eqs. 3.1 and 3.2. Note that the imaginary part of the

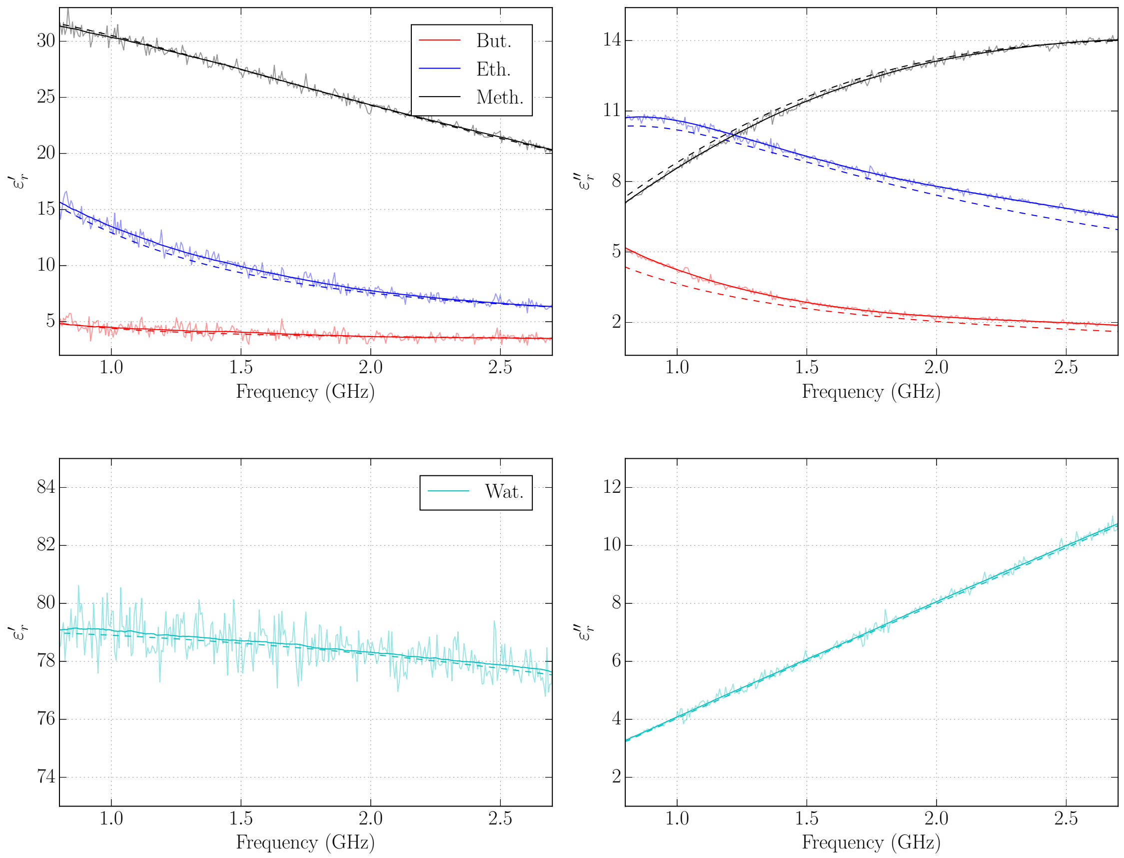

(a) Real (b) Imaginary

Figure 3.3: Measured liquids (solid) compared with models (dashed) for the alcohols [60] and water [11] at 20°C and 22°C, respectively.

permittivity does not necessarily have the same relationship with temperature as its real part, where one notable example is methanol at 2.5 GHz, which shows opposing behaviour between its real and imaginary terms.

Figs. 3.1 and 3.2 and their underlying models are useful for predicting permittivity behaviour across temperature and frequency ranges, but it is reasonably likely that the LUTs are not of as high a purity grade as those assessed in reports such as [60]. Additionally, the temperature of a measurement environment may well not sit perfectly in-line with the samples at which values such as ε_∞ or f_{rel} are referenced, although this can be resolved by interpolating the data. In any case, it is perhaps prudent to measure liquids intended for measurement before relying on theoretical models. Using an open-ended coaxial probe method, outlined in [18], each liquid was assessed using a commercial dielectric assessment kit (DAK) software package, and the results are shown in Fig. 3.3. It should be noted that raw measurements are smoothed with a low-pass filter, discussed in section 3.4, where the unfiltered data points are shown as slightly transparent. The dashed lines display the modelled

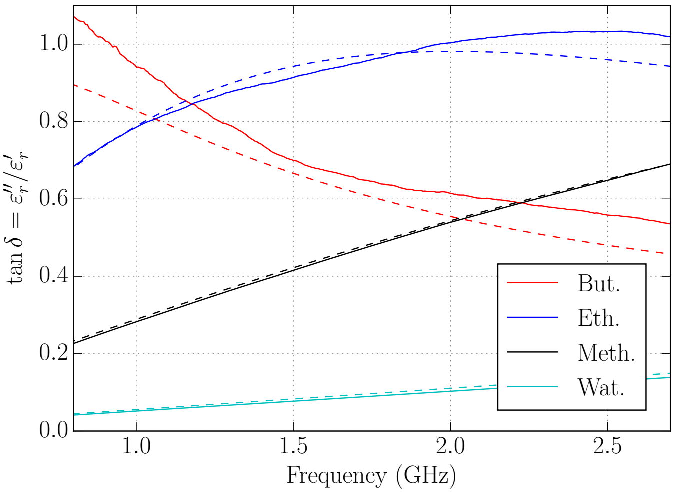

Figure 3.4: Measured (solid) and modelled (dashed) loss tangent $\tan\delta = \varepsilon_r''/\varepsilon_r'$ at 20°C for each liquid at 20°C.

permittivity at 20°C for the alcohols, and 22°C for water. The room temperature was generally between 21 and 22°C during measurements, but the closest tabulated data in [60] is referenced at 20°C, whereas the model in [11] includes a temperature variable. Nonetheless, the agreement is still very good and so no attempt was made to interpolate models in [60]. Finally, we see the modelled and measured loss tangent for every liquid in Fig. 3.4, displaying slightly less agreement for butanol and ethanol, but still acceptable. We see that, at lower frequencies, water and methanol display relatively low loss in comparison with butanol and ethanol, which has implications for the Q-factor of the sensor response, as discussed later.

3.2 Fabrication

The adaptive geometry of the sensor results in a large variety of possible configurations, where work in this thesis focusses on the slot width and length due to fixed pipe dimensions. In order to measure the effect of changes in SW and SL somewhat comprehensively, it was necessary to fabricate a relatively large number of sensors, and so any advanced fabrication methods would have significantly increased the total cost and time taken to produce the required devices. To avoid these issues each sensor is constructed simply from an etched Mylar film, which is wrapped around a PTFE pipe and soldered along its length, where the films used in this thesis had a thickness of 125 μm and single-sided 35 μm copper cladding. Fig. 3.5 shows a bird's-eye view of the initial etched piece of Mylar, which is $2\pi r$ by SL, as well as a cross-sectional view of the wrapping process. In practice, the sheet is slightly

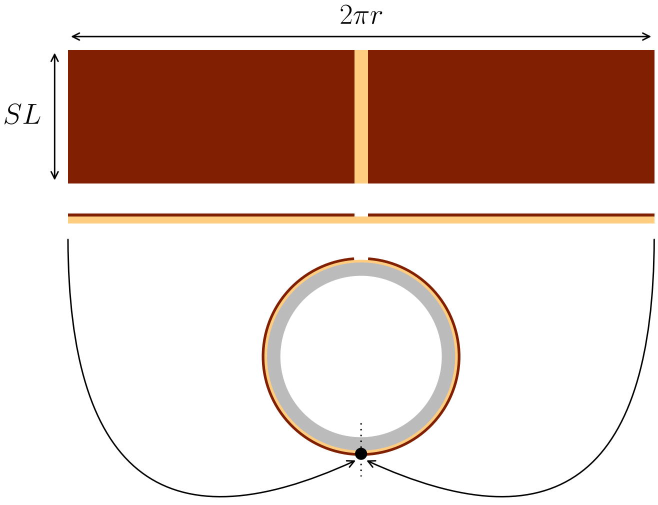

Figure 3.5: Diagram showing a bird's eye view of the fabricated Mylar film and its placement onto the PTFE pipe, where the solder joint is shown.

larger than $2\pi r$ to enable a small overlap when the film is wrapped around the pipe, which can then be soldered at the dotted line to ensure a relatively good electrical connection. An example of a fabricated sensor, where $SL = 50$ and $SW = 0.5$ mm, can be seen in Fig. 3.6, showing the slotted front and soldered rear-view. The small overlap, usually 5 - 10 mm, causes an offset in the solder joint position, where it is not necessarily diametrically opposite to the slot as suggested for the ideal case in Fig. 3.5. With hindsight, it may have proved useful to solder the sensor away from this position, as the discontinuities resultant from the joint will perturb currents flowing around the cylinder, an effect worsened by the fact that currents are a maximum in this region, as shown earlier in Fig. 2.9. Soldering midway between the slot and the base of the sensor may have offered a compromise between perturbation of the excited currents and electric field.

It was necessary to install and remove the fabricated sensors a large number of times during experimental work, and as a result the sensor radius was required to be slightly greater than that of the pipe. If the sensors were soldered too tightly, movement along the pipe was restricted and re-installation after removal was almost impossible without damaging the structural integrity of the film. The models discussed in section 2.2 suggest that the overall increase in r will act to increase both L and C_{surf}, see Eqs. 2.2 and 2.14, respectively. As a result of the increased size, the film developed a tendency to bend along the slotted region due to the reduced strength caused by removal of the copper cladding, a behaviour which worsens for

(a) Front-view showing slot. (b) Rear-view showing solder joint.

Figure 3.6: Fabricated sensor, $SW = 0.5$ mm and $SL = 50$ mm.

decreasing slot widths. An example of this effect for a sensor of $SL = 25$ and $SW = 0.5$ mm can be seen in Fig. 3.7, showing the sensor both on and off-pipe. Fig. 3.7b demonstrates the severity of the bending observed along the length of the slot, as well as the asymmetry caused by the offset of the solder joint. When installed on the pipe in Fig. 3.7a, the importance of the issue is shown clearly by the introduction of an air gap between the slot and the outer surface of the pipe. The impact of this gap is difficult to analyse accurately, where its exact shape is not easily obtainable and is in any case dependent on the slot width and soldering process. There will certainly be a change in the effective permittivity around the slot, as the gap will act to reduce ε_e due to the addition of a region of ε_0 between it and the PTFE, and indeed liquid. Additionally, with reference to Fig. 2.14 which displayed the angle of each slot edge from vertical, bending will increase the angle 2θ between the slot edges and consequently reduce the value of C_{gap}. As seen from this general discussion, the combined effect of increased sensor radius and bending along the slot presents a complicated scenario, where increases in L and C_{surf} act to decrease the resonant frequency of the device, and reductions in ε_e and C_{gap} have the opposite effect. Consequently, it is possible that the opposing effects on f_r tend to cancel to a degree, resulting in measurements that do not deviate too greatly from simulations, as will be shown later in this chapter. Given the difficulty in accurately modelling the effects discussed here, and the variation in such effects observed from sensor-to-sensor, no further attempt will be made to quantify their impact.

Four fabricated sensors of different slot lengths are shown in Fig. 3.8, each with a slot width of 0.5 mm. It can be seen that the smaller sensors feature a short extension of Mylar film beyond the metalised section, this was used to aid in the soldering and

(a) Top-down view showing bending around the slot.

(b) Sensor off-pipe showing Mylar bending.

Figure 3.7: Fabricated sensor, $SL = 25$ mm, displaying film bending issues.

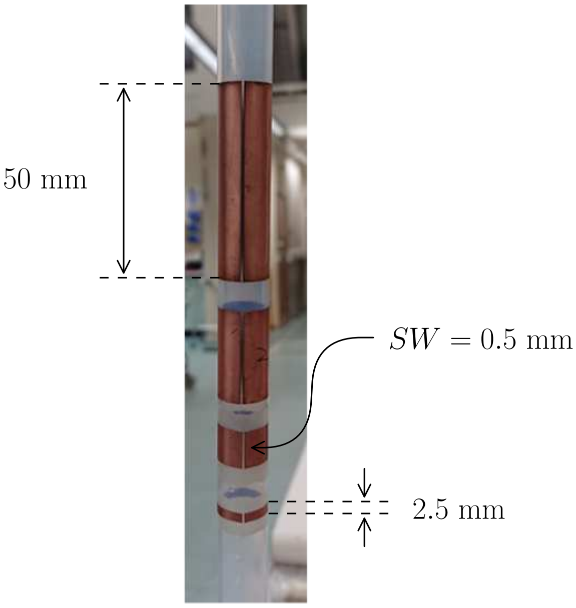

Figure 3.8: Several sensors placed on a PTFE pipe, $SL = 50$, 25, 10 and 2.5 mm, $SW = 0.5$ mm.

placement of devices and has no relevant effect on sensor behaviour. It should be noted that the majority of sensors in this thesis feature a slot width of 0.5 mm, which was decided as a compromise between maximising the Q-factor and more practical reasons related to fabrication, where etching tolerances and film bending had to be considered. The proposed geometry would benefit greatly from a more advanced fabrication technique which, while more costly, would greatly improve reproducibility and consistency. Despite the issues raised in this section, the fabrication technique is sufficient to demonstrate the behaviour and performance of the liquid sensor, where discussion will now turn to experimental work.

3.3 Experimental Environment and Methodology

This section intends to discuss various aspects of the experimental environment, covering the measurement technique and methodology. A brief study on the effects of changes in the measurement environment will also be presented, where the impact of issues which may arise in practice is assessed, such as changes in the sensor or antenna positioning.

3.3.1 Measurement Method

There exists a fundamental consideration in the measurement of reflective microwave structures as to whether one or two antennas are used. In a single antenna measurement system the reflection coefficient S_{11} is used to measure and characterise a device, as the system represents a one-port network with no other S-parameters to consider. For a structure which is incorporated into a system using two antennas, the transmitter T_x and receiver R_x, both S_{11} and the transmission coefficient S_{21} may be useful in characterisation. For single antenna measurements it is expected that the device under test (DUT) is in direct line of sight (LoS) of the main lobe of the transmitting antenna's radiation pattern, whereas two antennas add a consideration regarding their position relative to each other and the DUT. A system in which both antennas are co-located is said to be monostatic, and where there exists a spatial separation of the transmitting and receiving antennas a system is referred to as bistatic. Some monostatic configurations may employ a single antenna as both T_x and R_x by using a controller to switch between transmitting and receiving modes, as is the case in some RFID systems, or use a circulator to remove the switching requirement. We also consider a LoS bistatic measurement where the antennas are aligned facing each other with the DUT placed between them, a method often used

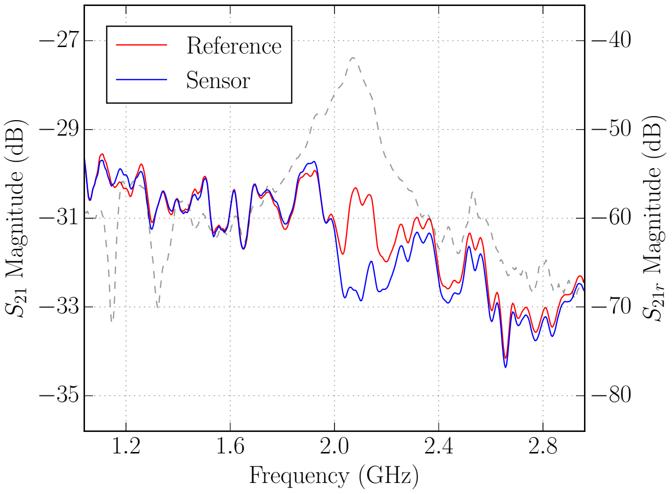

Figure 3.9: Example measurement showing S_{21} with and without a sensor in place, where the dashed line displays the resultant S_{21r} response.

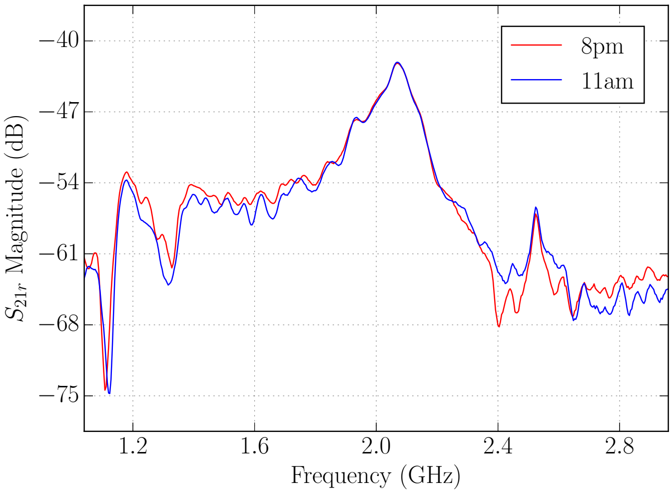

Figure 3.10: Measurements taken at 8pm and 11am the following day using the same reference reading.

to measure frequency-selective surfaces.

Away from resonance the proposed sensor will effectively act as a solid cylindrical reflector, where incident waves will be scattered accordingly. At resonance, energy will be coupled through the slot into the sensor cavity and re-radiated in the direction normal to the slot axis with no great deal of directivity, but certainly not isotropically. For lossy liquids of high ε'' the attenuation within the sensor at resonance will be relatively high, resulting in a reduced reflection at f_r. The sensor was shown to have little impact on S_{11} or S_{21} measurements unless the read distance was very small (< 10 cm) and the sensor was relatively large, where $SL > 100$ mm, and this effect was worsened considerably by lossy liquids. Instead of using direct S-parameter measurements, we may capture a reading with no sensor present and subtract this from a subsequent measurement where the sensor is in place, thus providing the difference caused by the device. All data which refer to a difference measurement will be identified with a subscript r denoting a relative result, where S_{11r} and S_{21r} refer to a relative reflection and transmission measurement, respectively. This method allows for much greater read distances and sensors at least as small as 2.5 mm, as well as the removal of reflections from the experimental environment, where large metal structures were present in all experimental work with no obvious detrimental effect. An example of a measurement is shown in Fig. 3.9, where the reference reading is compared with a sensor reading, and the resultant S_{21r} response is shown by the dashed curve. The difference is calculated by a native function on the Vector Network Analyser (VNA), which results in some uncertainty as to how the S_{21r} curve is precisely formatted. However, taking the log of the difference between the current reading S'_{21} and the reference S_{21} as:

$$S_{21r} = 20\log_{10}\left(|S_{21} - S'_{21}|\right) \tag{3.6}$$

consistently returns the same resonant frequency as the result displayed by the VNA. One concern of using this method is the potential requirement to take frequent reference readings in response to changes in the measurement environment, which may increase the background noise level. It was instead the case that repeat readings were generally not necessary even for measurements spanning an entire week, excluding, of course, scenarios where the experimental configuration was changed in some way. Fig. 3.10 shows a comparison of two S_{21r} curves using the same reference reading, which was taken at approximately 7pm, where the measurements themselves were subsequently taken at 8pm and 11am the following morning. This result was obtained outside of the anechoic chamber, unlike the majority of results in this thesis, showing that even for environments which have not been rigorously designed to reduce interference the reference reading remains valid for long periods of time. Additionally, the use of a relative measurement is not intended for use in a practical system, but does aid in the characterisation of the sensor for research purposes.

Two possible antenna configurations are shown in Fig. 3.11, showing LoS and reflective bistatic measurements. It is worth noting that the slot position is different for each method, although the rotational orientation of the sensor will be shown to be non-critical in a later section. Single antenna measurements are simpler to configure and would reduce cost in a practical system, but the attenuation caused by lossy liquids has a highly detrimental effect on S_{11r} readings. The reference S_{11} measurement will be relatively small across the operating bandwidth of the antenna,

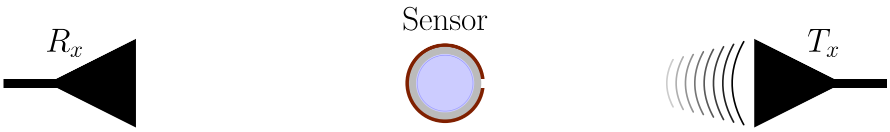

(a) LoS.

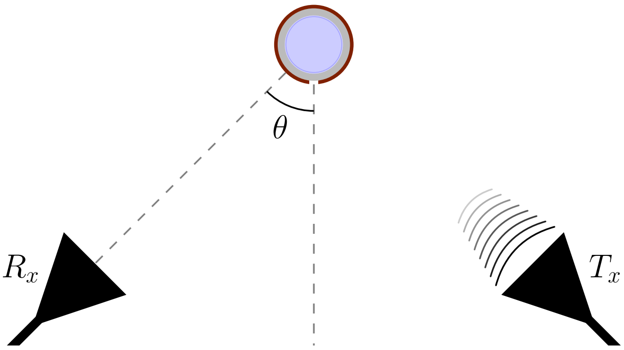

(b) Reflective.

Figure 3.11: Diagram showing two bistatic configurations, LoS and reflective.

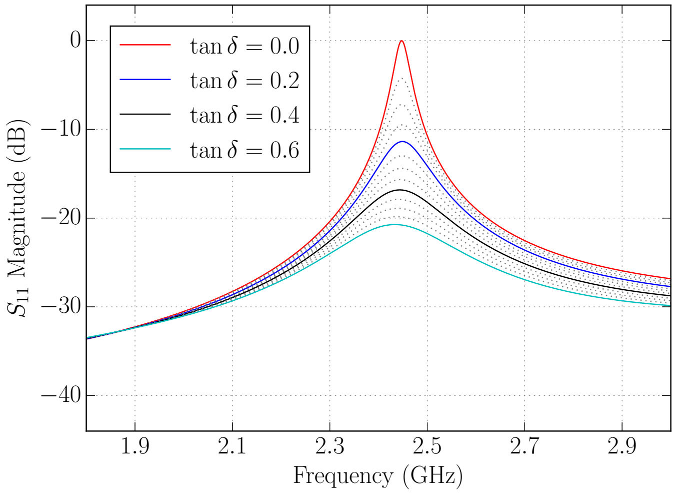

Figure 3.12: Effect of liquid $\tan\delta$ on simulated S_{11} magnitude.

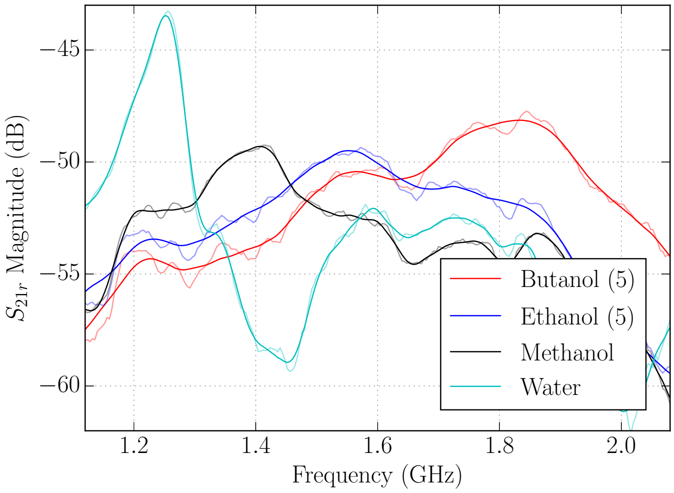

Figure 3.13: Measured S_{21r} for each liquid for a reflective configuration (Fig. 3.11b), where butanol and ethanol are measured with 5 sensors in place.

at least below −10 dB but typically lower. Fig. 3.12 displays the simulated S_{11} magnitude for liquids of varying loss tangent $\tan\delta$, where the Q-factor decreases from 80.3 to 10.3. When an empty sensor ($\tan\delta = 0$) is introduced, or one containing a low-loss liquid, the maximum S_{11} amplitude at resonance provides a measurable peak in the S_{11r} result from which we may identify f_r. However, for high-loss LUTs the sensor reflects very little energy at resonance and so the measurement does not appear to differ too greatly from the reference S_{11} reading, resulting in a poorly-defined resonance. This same problem is observed in a reflective bistatic configuration shown by Fig. 3.11b, where measurements are of a relatively low-Q and prone to high levels of noise. Without further explanation of the measurement process, which is discussed later in this chapter, Fig. 3.13 displays the S_{21r} result in this configuration for each LUT, where butanol and ethanol both required multiple sensors, a concept later introduced in section 3.7. This figure may be useful for reference following subsequent measurements presented in this thesis in order to compare the performance of a two antenna reflective configuration with the LoS method, which is the chosen experimental format.

For LoS measurements, a large portion of the transmitted power will arrive at R_x resulting in a relatively high S_{21} reading, depending on the ability of the DUT to reflect, scatter or attenuate incident waves, and the appropriate alignment of the antennas. Positioning of the antennas in Fig. 3.11b can be somewhat difficult, and positional errors may have a very significant impact on the quality of measured results due to already low transmission, whereas LoS alignment is relatively straightforward and small movements of the anntenas have only a minor impact. Attenuation may be

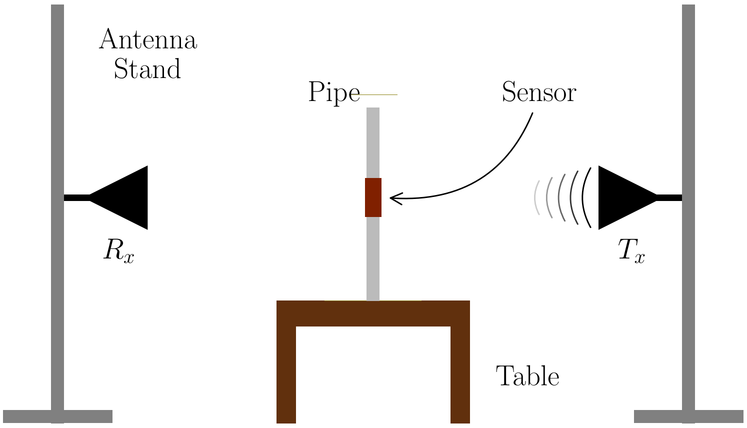

Figure 3.14: Side view of the experimental setup, wooden frame is not shown.

used advantageously in a LoS system, which offers a distinct advantage over a single antenna or reflective method. As a relative transmission measurement is concerned with the magnitude of the difference between measurements, attenuation observed at resonance will result in a peak at f_r on the S_{21r} response curve, as this attenuation was not present in the reference reading. It is true that the reference S_{21} reading does not include non-resonant reflections from the sensor, but this effect is generally frequency-invariant and presents a constant background noise level in the S_{21r} result. That is to say, provided that the attenuation or reflection caused by the sensor at resonance is greater than the non-resonant reflection level, we will observe a peak in the S_{21r} result which identifies the resonant frequency of the DUT. Of final note is the increased practicality of the LoS configuration, which greatly improved access to the experimental environment due to the lack of necessity to move antennas to reach the sensor support frame, as well as the improved consistency in aligning the antennas and DUT across a number of experimental sessions.

All experimental work was carried out within an anechoic chamber in order to reduce interference caused by Wi-Fi routers, phone signals and other electrical noise. The antennas were mounted onto identical aluminium stands with sliders for vertical alignment, and heavy bases to avoid accidental movement while entering and exiting the chamber, as the space available was relatively compact. The experimental frame, supporting the PTFE pipe and DUT, was placed equidistant between the antennas on a small wooden table, where a side-view of the measurement can be seen in Fig. 3.14. To mount the PTFE pipe vertically, as is necessary for liquid measurements, a simple wooden frame was constructed. The pipe is sealed by a PTFE bung at the bottom, and held in place by an inserted nylon rod at the top. The frame can be seen in more detail in Fig. 3.15, where the frame shown was used for every experimental

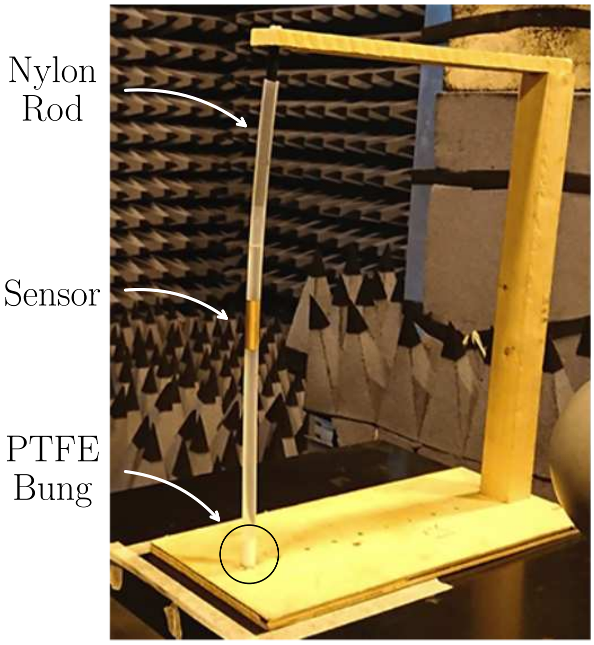

Figure 3.15: Picture of the experimental frame, showing the mounting components.

result in this thesis. Sensors can be placed on to or removed from the pipe by simply removing the nylon rod and sliding the DUT on or off. This allows for any number of measurements be taken, with different sensors, without the need to remove the frame from the chamber or move it at all, thereby maintaining consistency between readings.

The interrogation antennas used in all experimental measurements can be seen in Fig. 3.16 and were two identical Log-Periodic (LP) antennas, operating from 0.85 to 26.5 GHz, with a typical gain of 8.5 dBi and linearly polarised [61]. A reasonably low-end VNA was used, [1] along with the simple Through Open Short Match (TOSM) calibration method. The antennas were connected to the VNA *via* $>$ 3m of cabling, including 2 SMA interconnects. Calibration took place at the end of each length of cable, where the reference plane lay at the input of each antenna. The experimental equipment was placed inside of the anechoic chamber with the VNA remaining outside.

Most of the data presented in this and the following chapter make use of real-time filtering functions when capturing data with the VNA, where 10-factor averaging and 1% smoothing apertures were used. 10-factor averaging simply averages 10 full-frequency sweeps to mitigate random, time-variant noise. The 1% smoothing aperture averages a subset of the sweep, where the subset is a window equal to 1% of the number of data samples. For example, for 1000 samples, the window is 10

---

[1] Rohde & Schwarz ZVL 13 [62].

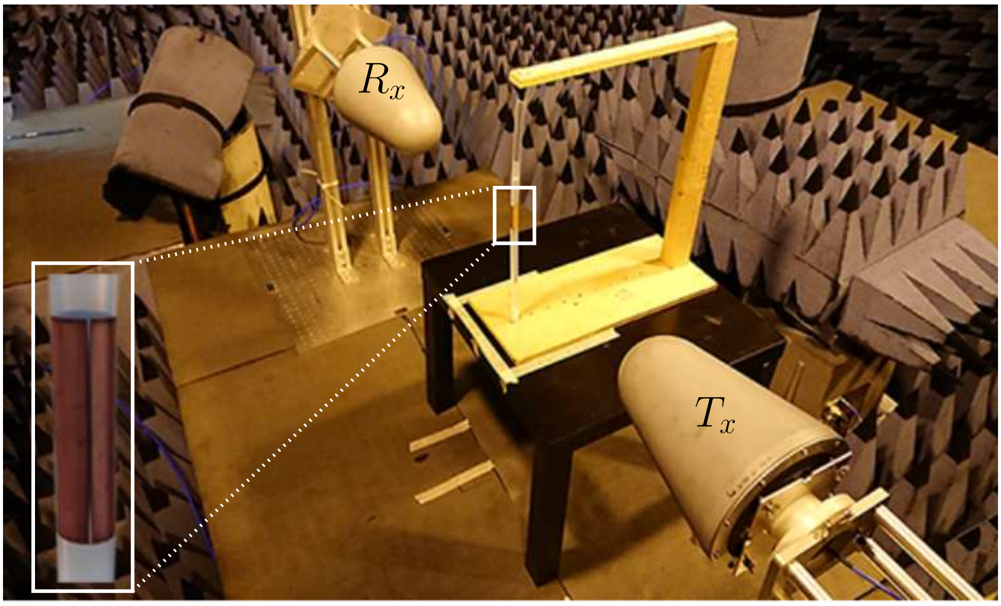

Figure 3.16: Picture of the experimental setup, showing the orientation of the sensor.

samples wide, and points 11 to 21 would be averaged to obtain the value at point 16. The concept of a moving average smoothing algorithm and noisy data processing is expanded upon in section 3.4. The next section will attempt to provide a sensitivity analysis of some potential sources of poor performance, which may arise from human error or the impact of a practical measurement environment.

3.3.2 Antenna Separation

For the great majority of wireless devices and sensors, performance is improved significantly when the wireless channel is shortened, thus improving the overall signal-to-noise ratio (SNR). Waves travelling in free-space suffer from path loss effects as they spread out, and in the far-field this loss may be calculated as:

$$PL = \left(\frac{4\pi d}{\lambda}\right)^2 \tag{3.7}$$

where d is the distance from the transmitter. Additionally, the power received P_r at the terminals of a receiving antenna R_x can be found using the Friis transmission equation:

$$P_r = P_t G_t G_r \left(\frac{\lambda}{4\pi d}\right)^2 \tag{3.8}$$

where we see the reduction in received power caused by PL. G_t and G_r refer to the gain of the transmitting and receiving antenna, respectively, and P_t is the

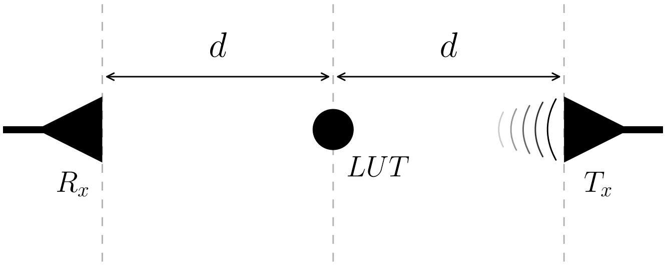

Figure 3.17: Bird's eye diagrammatic view of the distance measurement.

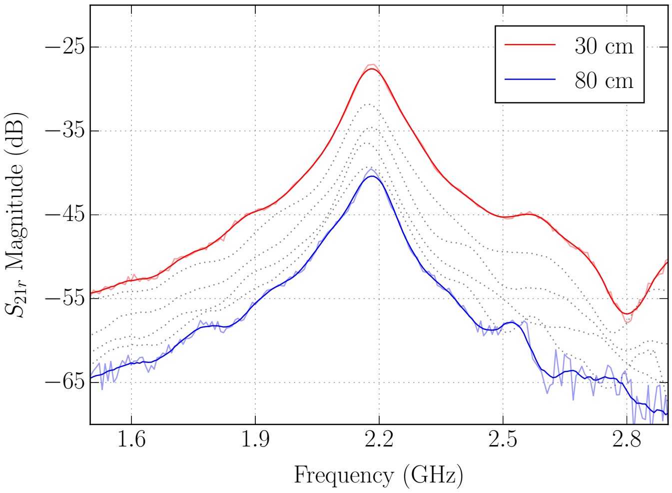

Figure 3.18: Variation of the S_{21r} magnitude for different read distances, d.

power delivered to the terminals of the transmitting antenna. It should be noted that Eq. 3.8 is valid only for antennas that are polarisation and impedance-matched and perfectly aligned. Reducing the distance between the measurement antennas will reduce path loss effects and maximise the amount of power delivered to the sensor. This is especially important for passive sensing devices, which rely on transmitting devices to supply all of the power in a system. Indeed, RFID tags require enough power to activate embedded chips, without which they would not function at all. In reality however, it is not often possible to achieve such small distances between transmitting/receiving antennas and sensors within a sensing system, and so robustness against a larger wireless channel is highly advantageous.

To assess the performance of the liquid sensor for larger distances, the device was placed equidistant between the two antennas which were carefully placed a distance $2d$ apart, as for all measurements. Fig. 3.17 displays a diagram of the measurement environment, where d is not to be confused with the pipe wall width. The maximum dimension of the experimental antennas is around 24 cm, which at 3 GHz results in a far-field distance of approximately 115 cm. Unfortunately, the measurement space available was not sufficient to take measurements exclusively in the far-field, though all results were at the very least obtained outside of the reactive near-field. [2] The distance was varied from 30 to 80 cm, with a new reference S_{21} measurement taken for each value of d. This experiment was carried out to assess feasible read distances and not the impact of antenna movement during monitoring, hence the repeated S_{21} readings. The S_{21r} magnitude for each distance, in 10 cm increments, can be seen in Fig. 3.18, where $SL = 50$ mm and $SW = 0.5$ mm. It is very clear that increasing the read distance d reduces the maximum amplitude of the reading, which is to be expected, but there is a similar reduction away from resonance resulting in no significant reduction in Q. The raw measurement data is shown for $d = 30$ and 80 cm as slightly transparent, and it is clear that there is a reduction in SNR for the larger read distance when comparing the noise levels away from resonance with the smaller distance. The smoothing algorithm shown here will be discussed in section 3.4. The overall change in amplitude is not necessarily of any great concern, as many measurements rely only on identification of the resonant frequency of the sensor to derive information on the LUT, but there is a small deviation in f_r over the range of distances. Even for small read distances the peak S_{21r} amplitude is below -25 dB, showing that the difference between the reference and current reading is very small, and potentially corruptible by noise. There is no observable trend in the movement of f_r over the course of the experiment, and so it would be expected to remain constant for a fixed measurement position. For the largest read distance which results in a wireless channel of 160 cm we see satisfactory performance, which is highly important for the potential application of real-time monitoring in an industrial environment. It would be beneficial to extend the channel further to assess the maximum read distance, but this was not possible given the dimensions of the anechoic chamber used for measurements. With reference to Fig. 3.16, the antenna stands are situated at approximately $d = 50$ cm, and the results for larger d were obtained by sliding the antenna stands partially off of the edge of the platform. The antennas were generally placed as seen in Fig. 3.16, but there may be some measurements which differ slightly, resulting in a range of S_{21r} peak amplitudes. This thesis makes no attempt to measure absolute amplitude, instead using relative trends and behaviour for analysis, and so small differences in the antenna distance are of no particular concern. It is also worth noting that the performance of the sensor with distance will be significantly impacted by the antennas themselves, where a higher gain should

---

[2] The far-field and reactive near-field distances are taken to be $\geq 2D^2/\lambda$ and $\leq 0.62 \times \left(D^3/\lambda\right)^{1/2}$, respectively.

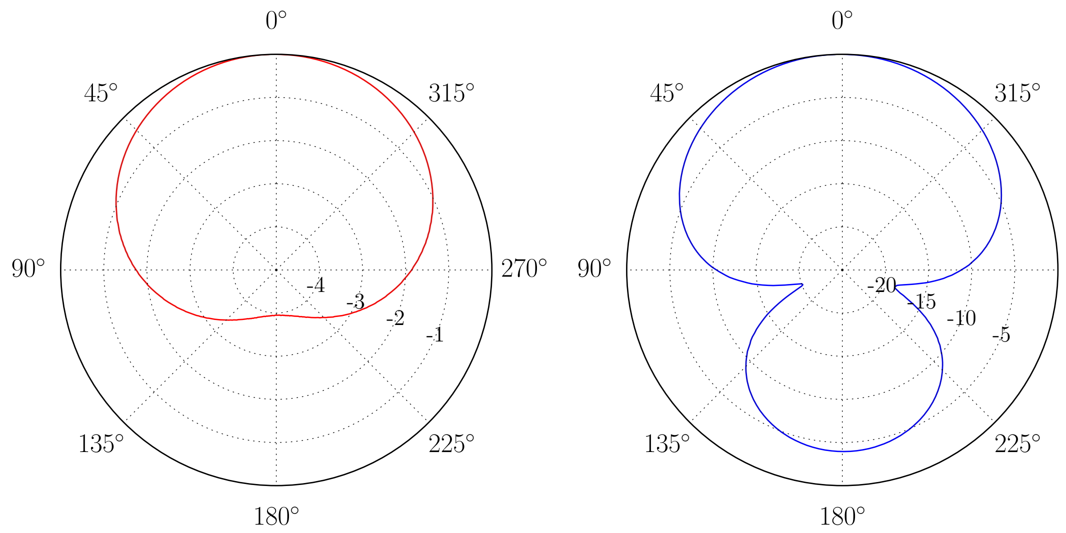

(a) x-y plane.

(b) z-y plane.

Figure 3.19: Normalised radiation pattern at f_c for the x-y (cross-sectional) and z-y (side) plane.

allow for larger read distances, and *vice versa*.

3.3.3 Sensor Rotation

Following the discussion of robustness in terms of distance, it is highly important to assess the potentially significant effect of sensor orientation. The sensor presented in this thesis has thus far remained in one orientation, where the slot is facing towards the incident plane wave, or $\theta = 0°$. Similarly to small read distances, it is not reasonable to expect that the sensor will always be placed perfectly or remain in the same position, and it would be highly beneficial if its orientation about the pipe axis had little effect. By exciting the sensor as a waveguide, discussed earlier in relation to Fig. 2.5, we may identify the cut-off frequency $f_c = f_r$ at which the structure resonates, and observation of the dip in simulated S_{21} results suggests radiation at this frequency. The normalised radiation patterns at f_c are shown in Fig. 3.19 for the x-y or cross-sectional plane, and the z-y plane seen when looking at the sensor from one side, both planes have the slot facing upwards and positioned at 0°. The x-y pattern displays a relatively small dynamic range around the sensor circumference, particularly ±90° from 0°, potentially showing that the radial position of the slot is not critical. To assess this, a sensor was measured with the range of orientations displayed in Fig. 3.20a, each using the same reference reading to mirror a real-world scenario where the device may be moved accidentally *in situ*. The measured S_{21r} magnitude for each position is shown in Fig. 3.20b, where $SL = 25$

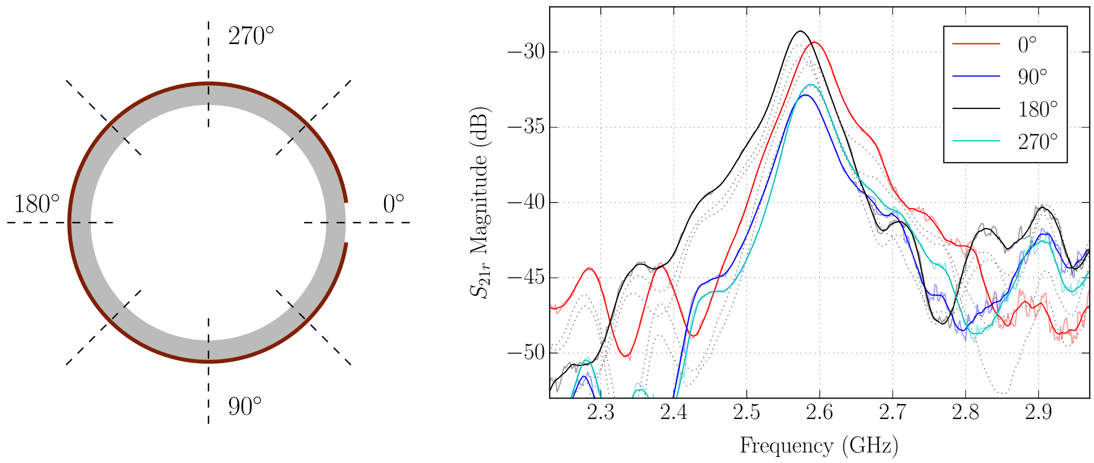

(a) Diagram of sensor positions. (b) S_{21r} magnitude for different orientations.

Figure 3.20: Diagram of sensor positions and associated measured results.

mm and $SW = 0.5$ mm.

It is clear that the orientation of the sensor has a small but relevant effect on the maximum amplitude, allowing for somewhat relaxed placement of devices in a practical measurement environment. A summary of the measured resonant frequency and maximum amplitude A_0 for each position is presented in Table 3.1, where we see a 20 MHz change (0.77%) in f_r and around 3.5 dB in A_0 over the course of the experiment. This is most likely due to a slight deformation of the Mylar film, as described in section 3.2, where the rotation of the sensor by hand has resulted in a small change in the slot positioning. For example, some rotations may have caused the slot to bend slightly more resulting in a larger air gap and greater radial distance, and *vice versa*, as shown by a sensor in place in Fig. 3.7a. The results show that the rotational positioning of the slot is not a critical consideration in the experimental environment, but care should be taken to not move the sensor where possible if high levels of precision are required. The radiation patterns shown in Fig. 3.19 are perhaps not accurate for the fabricated sensors, as it is assumed that the film bending may have significant affects on directivity. Indeed, the maximum measured amplitude is observed when the sensor is facing directly away from the transmitting antenna, which does not agree with Fig. 3.19a.

3.3.4 Sensor Vertical Position

With reference to Figs. 3.14 and 3.17, it has so far been assumed that the sensor is in the direct LoS between T_x and R_x. It is relatively simple to achieve this in a lab environment, but may be difficult or impractical in real-world scenarios. A

Table 3.1: Effect of sensor rotation.

Rotation	f_r (GHz)	A_0 (dB)
0°	2.592	-29.4
45°	2.588	-32.3
90°	2.580	-32.9
135°	2.574	-30.4
180°	2.574	-28.6
225°	2.572	-29.5
270°	2.588	-32.1
315°	2.588	-30.7
360°	2.592	-29.5

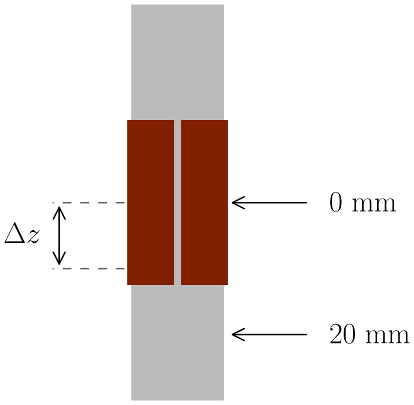

Figure 3.21: Diagram of the vertical position measurement.

sensor of $SL = 25$ and $SW = 0.5$ mm was placed on a water-filled pipe and moved into an approximate LoS position, then finely moved until the maximum S_{21r} peak amplitude was observed. From this position, $z = 0$, the sensor was moved downwards in 2 mm increments, which can be seen in Fig. 3.21. The S_{21r} magnitude for each measurement can be seen in Fig. 3.22. It is shown that the performance of the sensor degrades as Δz increases, as expected, where the maximum amplitude decreases as the vertical offset of the sensor increases. This measurement displays that a positional error of ±20 mm from the optimal LoS location will still provide satisfactory sensor performance for a water-filled pipe, but the effect of a misalignment error would be expected to worsen for liquids of higher loss.

It is worth noting that the antenna read distance will affect the impact of the vertical position of the sensor, where smaller distances would be more susceptible to changes in Δz given the greater resultant angle between LoS and the offset position. Fig. 3.23 displays an example of the relative levels of power received from the transmitting antenna over different regions of the pipe, where the decrease

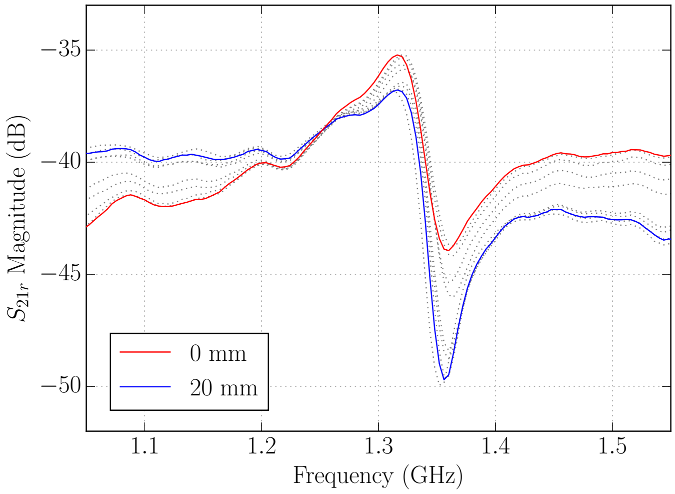

Figure 3.22: Effect of the vertical positioning of the sensor on the S_{21r} magnitude for water.

in radiated power as we move away from LoS will be a function of the antenna's directivity. Using the radiation pattern of the LP antenna used in measurements given in [61], it is possible to estimate the received normalised power over regions on the pipe for a given antenna distance. Let P_0 equal the maximum gain delivered by the antenna along the LoS angle $\theta = 0$, or when $\Delta z = 0$ mm in Fig. 3.21. The values of θ for $0.5P_0$ to $0.8P_0$ are then used to calculate the maximum offset from $\Delta z = 0$ possible while still receiving a given amount of power. The Δz ranges for $0.5P_0$ to $0.8P_0$ for antenna distances of $20 \leq d \leq 60$ cm can be seen in Table 3.2, where the values are listed as ± cm relative to LoS. The resultant Δz ranges are not of particular concern unless the read distance becomes relatively small and higher gains are required for measurements, though nonetheless, Fig. 3.22 shows that there is an impact on the S_{21r} magnitude for relatively small changes in Δz. It should be noted that smaller sensors would be expected to be more susceptible to changes in position, as longer sensors would remain in LoS for a greater Δz. The values presented in Table 3.2 are not of immediate concern and will not be discussed further, but they do become relevant for highly directive antennas and subsequent sections which discuss the placement of multiple sensors on a single pipe.

3.3.5 Antenna Polarisation

For all of the experimental results presented, care was taken to ensure that the antennas were correctly polarised, though it would not necessarily be feasible to ensure such high levels of accuracy in a practical environment. Similarly, it could be the case that in practice the pipe orientation may not allow for perfect alignment.

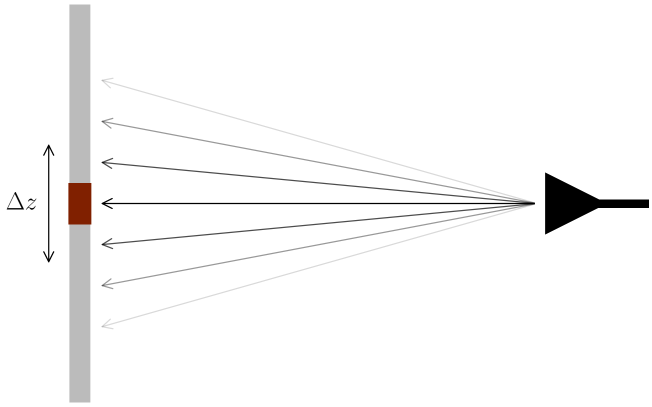

Figure 3.23: Diagram illustrating the levels of power received over different pipe regions.

Table 3.2: Range relative to LoS receiving fraction of maximum power P_0 for different antenna distances d.

	Δz Range (± cm)			
d (cm)	$0.8P_0$	$0.7P_0$	$0.6P_0$	$0.5P_0$
20	9.33	13.49	16.78	23.84
30	13.99	20.24	25.17	35.75
40	18.65	26.98	33.56	47.67
50	23.32	33.73	41.95	59.59
60	27.98	40.47	50.35	71.51

As such, it is important to assess the performance degradation of the sensor as the orthogonality between the slot axis and the antenna polarisation is lost, either by rotation of one of the antennas or the sensor. A single reference S_{21} reading was taken with the antennas correctly polarised, and the interrogating antenna was then rotated through 45° in regular increments. The use of a single reading intends to mimic a potential real-world scenario where the polarisation(s) of the antenna(s) may be mistakenly changed, and repeating the reference readings for each new polarisation still identified the correct resonance even up to 45°, albeit with lower amplitudes and SNR. Additionally, if it were practical to take new reference readings in a real measurement environment, it would follow that the alignment of the antennas could be fixed also. Figs. 3.24a and 3.24b display the effect of the antenna polarisation on the S_{21r} magnitude for air and water, respectively.

The nature of the experimental antenna mounts made it difficult to accurately rotate the antenna through exact angles, but attempts were made to keep each rotation consistent up to 45°, requiring 9 movements in total. The measured result

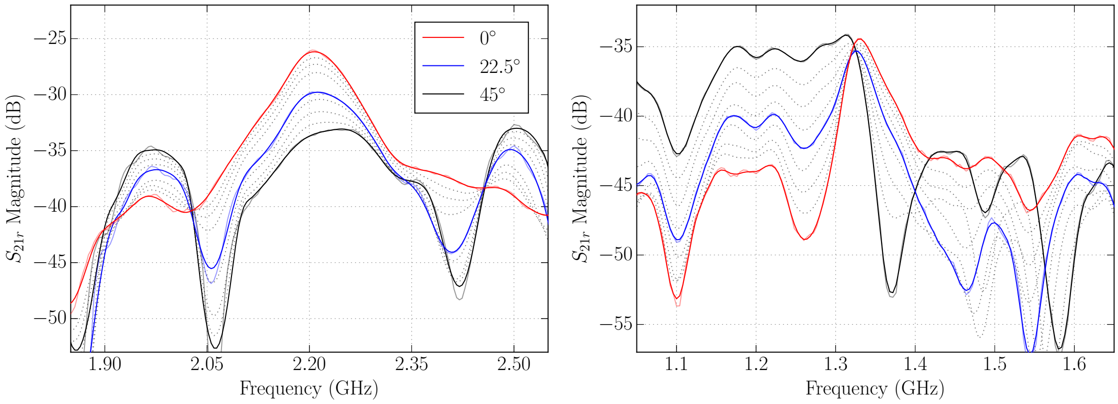

(a) Air

(b) Water

Figure 3.24: Effect of the antenna polarisation on the measured S_{21r} magnitude for air and water.

labelled as 22.5° was taken at the approximate mid-point of the total rotation, and though not necessarily correct, certainly aids in determination of the trend of results. The resonant frequencies identified at each polarisation sample are shown in Table 3.3 for both air and water measurements. The higher frequency secondary peak which is present in the air measurements for the latter part of the rotation is ignored for the purposes of identifying f_r, as it would be for practical measurements through filtering. It can be seen that the air measurement remained valid for over half of the rotation, where the resonant frequency did not significantly deviate until the antenna reached the final 2 positions, showing a maximum change in f_r of 8 MHz, or 0.4%, up to sample 7. Water was similarly resilient, showing a an equal maximum change equivalent to 0.6% over this range, and only 12 MHz in total. Though the sensor is never intended to operate with poorly polarised antennas, it is beneficial that it is generally robust against relatively large changes in polarisation which may occur in practical, real-world scenarios.

3.4 Noisy Data Processing

Data obtained from difference measurements are naturally noisy when observing small changes, and the determination of peaks, as is required to calculate f_r, can become difficult and result in errors. While this can be mitigated to some extent by real-time VNA functions, mentioned in section 3.3.1, it is advantageous to use some form of post-processing smoothing. Noisy data can be thought of as relatively high-frequency oscillations mapped onto the desired, lower frequency trend, and thus it follows that a low-pass filter is ideal in this case. The Savitzky-Golay (SG) filter is

Table 3.3: Measured air and water f_r for each polarisation position.

Sample	Air (GHz)	Water (GHz)
1	2.208	1.328
2	2.208	1.328
3	2.208	1.328
4	2.212	1.328
5	2.212	1.328
6	2.216	1.324
7	2.216	1.320
8	2.228	1.320
9	2.248	1.316

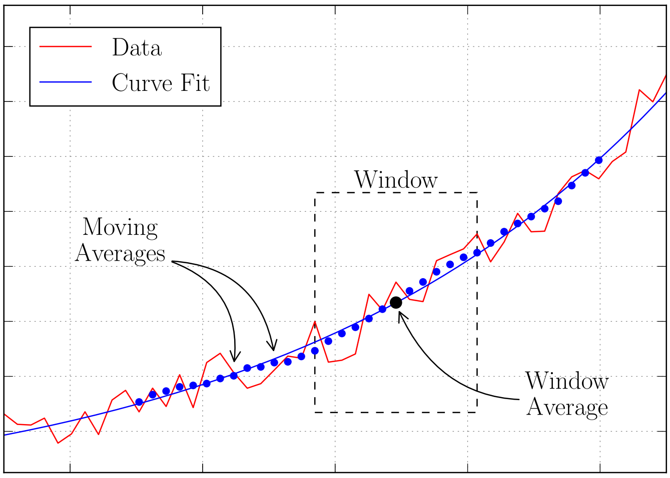

Figure 3.25: Example displaying a simple averaging algorithm.

one such algorithm, which also has the advantage of straightforward programmatic implementation. This section aims to briefly consider the choice of the SG filter and justify its use over a more computationally and conceptually simple smoothing algorithm.

Smoothing functions generally refer to a window of size n, which defines the number of data points analysed per iteration of the algorithm. The simplest filter of this type implements a moving average, where n samples are averaged within a window, which then shifts along by 1 data point, and the resultant line drawn through each moving average point provides a relatively smooth representation of the original noisy data. Using an arbitrary function of the form $y = e^x + N_r$, where N_r represents some random noise, a moving average filter of $n = 10$, with 50 data points, was applied in Fig. 3.25. The curve is fit to the moving average points well by assuming an exponential curve, providing the curve-fitting function with good

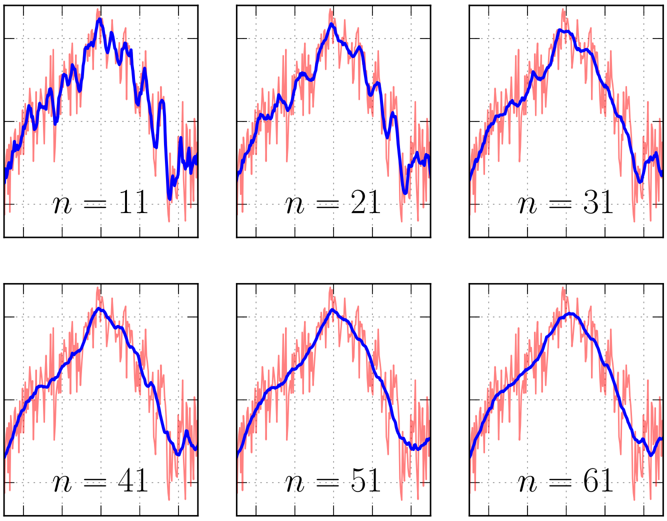

Figure 3.26: Example of the effect of the window size n on the smoothed output.

starting conditions. While this simple algorithm works well for the data in Fig. 3.25, it becomes increasingly difficult to appropriately fit curves without an initial assumption of their shape. Additionally, averaging is a reasonable approach for noise independent of the measured variable and which is normally distributed, where instead the noise present in antenna measurements may well not be independent, and can be highly frequency-dependent. Such noise can be difficult to remove by averaging without resorting to increasingly large values of n, which consequently distorts the data. The SG filter similarly analyses data points within a window of size n, but instead fits a polynomial of a given order to the data within the window. This is then evaluated at the central data point to provide a single output, and the window is iteratively moved along until the smoothed output is complete. One particular advantage of this filter is that the polynomials calculated towards each end of a data set can be extrapolated to alleviate data points lost as a result of the window size. Consequently, it is possible to apply the SG filter without significant distortion of the data and achieve highly smoothed outputs. An example of the algorithm used on real measurement data is shown in Fig. 3.26, where the effect of the window size is clearly displayed. It can be seen that the filter fits an accurate curve and there appears to be very little distortion.

The Savitzky-Golay filter presented in this section will be applied to varying degrees throughout the presentation of measured data, where attempts will be made to display the original data where applicable. Original data will not be displayed in instances where it is visually disruptive, and will appear transparent in any case of its use otherwise. The size of the window was set by a convergence algorithm, which iteratively applied the filter to raw measurement data with an increasing window size until the calculated resonant frequency remained stable. After 5 iterations with a constant f_r, the window size was set to the first, lowest, window size in this set of stable results to avoid the over-smoothing of data. As mentioned in section 3.3.1, a real-time VNA smoothing function was also used for most measurements, but different settings were applied unintentionally for some measurements which may appear more noisy than others. It is true that a more generous VNA smoothing process would have produced clearer measurements, but it is not always obvious in real-time whether such results are accurate. Applying a low-pass filter as a post-processing step allows for direct comparison with original measurement data, allowing us to determine whether the applied smoothing is appropriate. The algorithm to implement the SG filter was written in Python and could be easily implemented on a microprocessor or FPGA device for real-time applications.

3.5 Verification of Simulated Results

This section aims to convey the accuracy of simulated results to verify their usefulness in predicting the sensor operation for different geometry or environments. As has been discussed in section 3.2, the sensor devices are not able to be accurately reproduced using the current, uncomplicated fabrication techniques. For this reason, this section aims to confirm that simulations follow the same trends and behaviour, though not necessarily absolute values, as fabricated and measured devices for air-filled pipes.

Slot Width

To assess the behaviour of the slot width, 9 sensors were fabricated, where $SL = 2.5$ mm and $0.2 \leq SW \leq 1.0$ mm. Five fabricated sensors of $SL = 2.5$ mm can be seen in Fig. 3.27, the slot width of each sensor shown is constant at 0.5 mm. A normalised comparison between measured and simulated results can be seen in Fig. 3.28, where four slot widths are shown. It should be noted that the plot is comparing the measured S_{21r} with simulated S_{11}, but the y-axis is labelled simply as ‘Norm. S-Parameter’ to avoid unnecessary confusion given the identical scale of both sets of results. There is generally a good agreement between measured and simulated values for the sensors shown in Fig. 3.28, where the tabulated comparison can be seen in Table 3.4. The percentages are given with respect to the measured values, calculated by dividing the absolute difference in frequency by the measured f_r for each slot width. It can be seen that the difference between results is no greater than 1.3%.

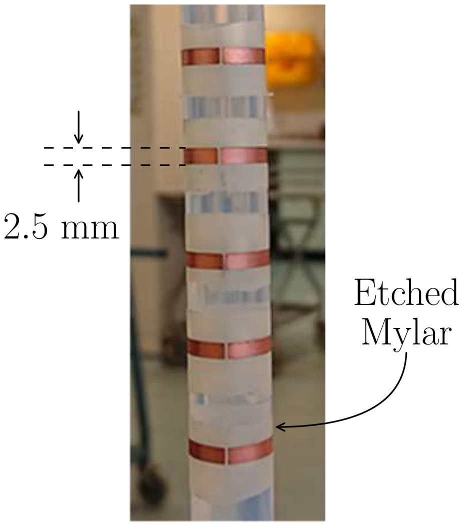

Figure 3.27: Example of 5 fabricated sensors, where $SL = 2.5$ mm and $SW = 0.5$ mm.

The inconsistency in the deviation between sensors displays the result of fabrication issues described in section 3.2, as perfectly reproducible sensors would be expected to display a more consistent offset from simulated results.

Table 3.4: Comparison of simulated f_s and measured f_m results from Fig. 3.28.

SW (mm)	f_s (GHz)	f_m (GHz)	$\lvert f_s - f_m\rvert$ (MHz)	%
0.2	2.446	2.478	32	1.29
0.3	2.508	2.520	12	0.48
0.4	2.555	2.564	9	0.35
0.5	2.592	2.586	6	0.23
0.6	2.624	2.596	28	1.08
0.7	2.654	2.642	12	0.45
0.8	2.680	2.656	24	0.90
0.9	2.704	2.700	4	0.15
1.0	2.725	2.724	1	0.04

Interestingly, only the three smallest slot widths result in a measured f_r greater than their simulated counterparts, where $SW = 0.2$ mm presents the largest differential. This is perhaps due to the tendency of the Mylar film to bend away from the pipe for smaller slot widths, as shown by the sensor in Fig. 3.7. However, the values are relatively small and it would be difficult to draw a conclusion of any great certainty. The complete family of non-normalised curves for the measured sensors can be seen in Fig. 3.29. It can be seen that as the sensor slot width increases there is a small but noticeable decrease in amplitude, and a qualitative assessment

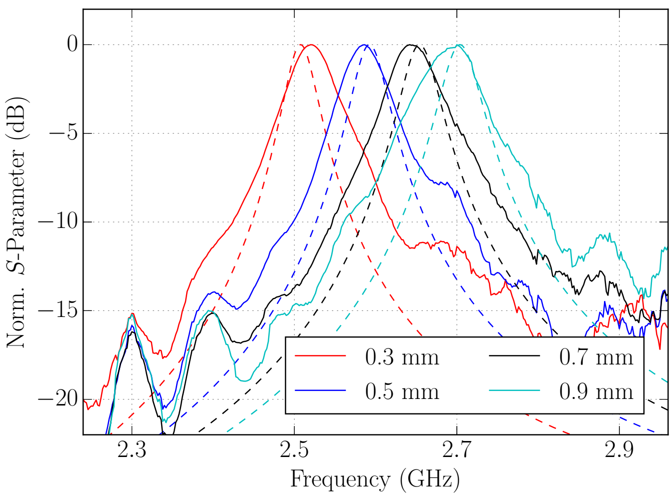

Figure 3.28: Normalised comparison of measured S_{21r} (solid) against simulated S_{11} (dashed) results for an air-filled pipe and varying slot widths, $SL = 2.5$ mm.

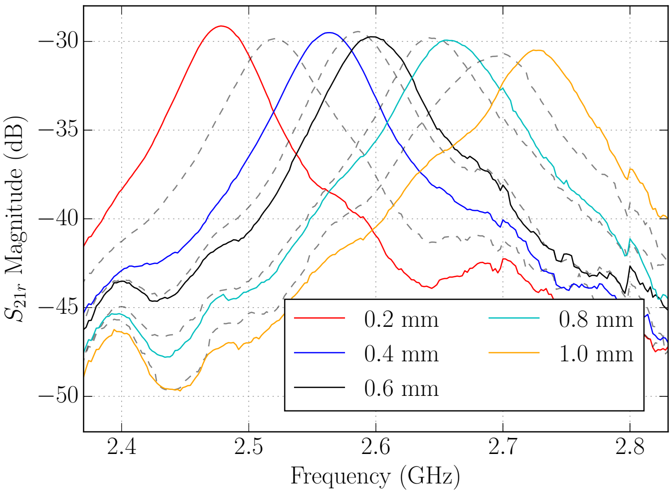

Figure 3.29: Measured S_{21r} magnitude for an air-filled pipe where $0.2 \leq SW \leq 1$ mm and $SL = 2.5$ mm.

would appear to show the small reduction in the Q-factor predicted by simulations in Fig. 2.30. This effect can be demonstrated more clearly by a larger slot width differential of $0.5 \leq SW \leq 3.0$ mm displayed in Fig. 3.30, where a set of longer sensors of $SL = 72$ mm were measured. The S_{21r} curves are first normalised and then arranged with respect to their respective resonant frequencies, allowing for a straightforward comparison in terms of percentage bandwidth. The smallest slot width $SW = 0.5$ mm displays superior resonance, with a bandwidth of approximately 13%, considerably smaller than the 27% observed when $SW = 2.0$ and 3.0 mm. It is also clear that the larger SW values show an increase in the level of noise present in measurements and therefore a reduction in SNR.

The measurements concerning slot width show that larger values of SW result

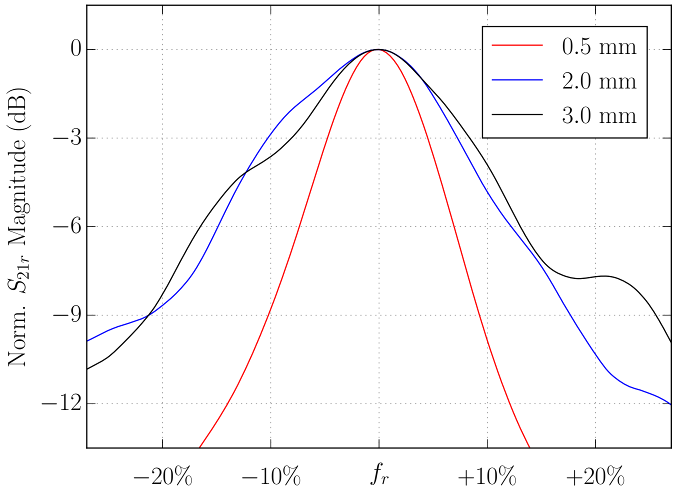

Figure 3.30: Comparison of normalised S_{21r} measurements for an air-filled pipe where $SW = 0.5$, 2 and 3 mm and $SL = 72$ mm.

in lower peak amplitudes, a reduced Q-factor and greater noise levels. However, as SW becomes very small, fabrication becomes more problematic due to Mylar bending and etching tolerances. This suggests there is a compromise to be found when selecting an appropriate slot width, as has been mentioned previously. Unless otherwise stated, it should be assumed that all subsequent measurements presented in this thesis use a slot width of 0.5 mm, where this value was found to produce acceptable results consistently.

Slot Length

The measured slot length was assessed through the fabrication of four smaller sensors of $SL = 2.5$, 5.0, 7.5 and 10 mm. Similarly to the slot width measurements, the normalised simulated and measured results can be seen in Fig. 3.31, using the same notation for the y-axis. Again the comparison is good, with no major deviation between measurement and simulation observed. The complete set of results is presented in Table 3.5, showing the percentage with respect to measured results.

There is a noticeably higher difference in results for the larger slot lengths, where $SL > 10$ mm, which may exist for reasons relating to simulation meshing. The larger model required to simulate longer sensors results in a high ratio of the largest to smallest dimension, for example, a slot length of 72 mm is very large compared to a 0.5 mm slot width. Adaptive meshing of a 2.5 mm sensor uses around 4000 cells, whereas a 72 mm sensor yields just over 12000, or three times the amount, despite a model which is significantly greater than three times the size. By increasing the number of mesh cells per wavelength, resulting in a total count of around 26000,

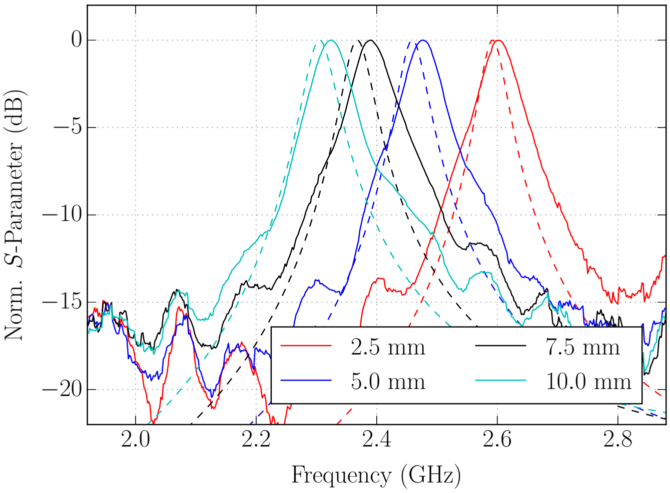

Figure 3.31: Normalised comparison of measured S_{21r} (solid) against simulated S_{11} (dashed) results for an air-filled pipe and varying slot lengths, $SW = 0.5$ mm.

the simulated f_r of the 72 mm sensor increased to 2.046 GHz thus reducing the percentage change to 0.39% from 3.21%. The Δf_r percentage was decreased similarly for $SL = 25$ and 50 mm to 0.69% and 0.93%, respectively. This would suggest that increasing the total mesh count is advisable for further simulations or in further work, and for larger sensors this is perhaps true. However, smaller sensors present little or no change with a finer mesh despite a significantly increased solver time, and fabrication issues mean that simulations will never be consistent with measurements regardless of their accuracy.

Table 3.5: Comparison of simulated f_s and measured f_m results from Fig. 3.31.

SL (mm)	f_s (GHz)	f_m (GHz)	$\lvert f_s - f_m \rvert$ (MHz)	%
2.5	2.593	2.602	9	0.35
5.0	2.459	2.476	17	0.69
7.5	2.367	2.390	23	0.96
10	2.305	2.324	19	0.82
25	2.141	2.166	25	1.15
50	2.053	2.096	43	2.05
72	1.988	2.054	66	3.21

The non-normalised slot length measurements are shown in Fig. 3.33, clearly displaying the impact of a larger effective aperture A_e, where a 7.5 mm increase in SL yields almost 3 dB in the peak amplitude. We also see that despite a relatively small size, a sensor of only 2.5 mm performs very well and suggests that the size could be reduced further still, if required. It is worth noting that Fig. 3.32 makes

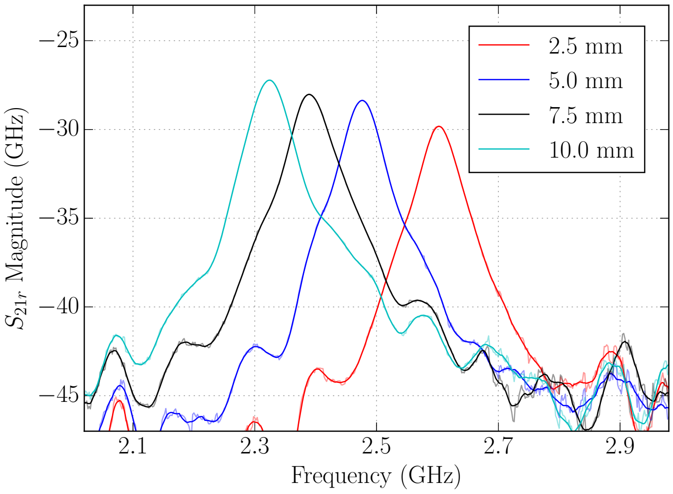

Figure 3.32: Measured S_{21r} magnitude for an air-filled pipe and varying slot lengths, $SW = 0.5$ mm.

use of SG filtering in contrast with the normalised measurements in Fig. 3.31, which shows original measurement data to reduce the number of curves.

As seen in Fig. 2.36, the simulated Q-factor decreases with sensor length, although a longer slot will also increase the size of the effective aperture, something which is important for more lossy materials. Three sensors of much larger lengths were fabricated and measured in Fig. 3.33, where $SL = 100, 150, 200$ and $SW = 0.2$ mm. Unfortunately, the long sensors were measured during an earlier experimental period where the antenna separation was 160 cm, or $d = 80$ cm as per section 3.3.2, thus explaining their reduced maximum amplitude. Fig. 3.33 shows that a total increase of 100 mm results in a maximum amplitude increase of around 4 dB, only marginally larger than the 3 dB improvement yielded by 7.5 mm of length displayed in Fig. 3.32, though admittedly this may also be affected by differences in antenna distance. Measurements of $SL = 2.5$, 10, 100 and 200 mm are compared in a similar manner to the process explained for SW measurements in Fig. 3.30, where the result can be seen in Fig. 3.34. The Q-factor is shown to worsen with increasing slot length as expected, though less significantly than for changes in SW displayed previously.

Despite the significantly larger dimensions there is not a satisfactory increase in performance given the additional fabrication complexity. The size of the fabricated films made them difficult to fix in place during the soldering process, as they had a tendency to unwrap from the pipe. Additionally, the positioning of the slot along the pipe axis was not particularly consistent across the sensor length and would require more considerable effort or advanced techniques. The sensors also tended to crease during installation and removal, perhaps due to their tighter fit resultant from the

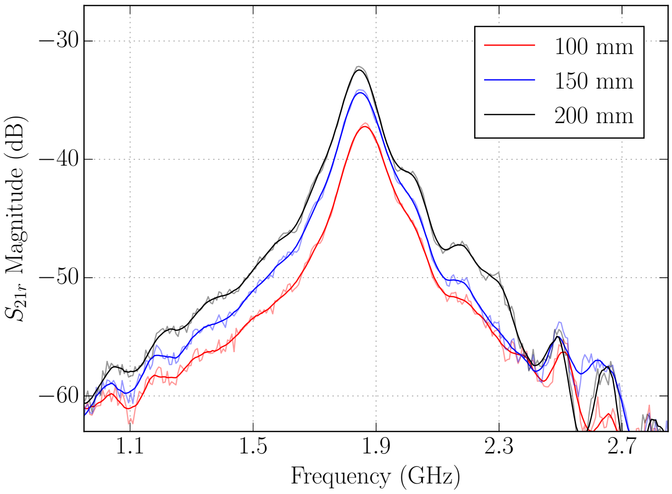

Figure 3.33: Measured S_{21r} for relatively long sensors, for an air-filled pipe and $SW = 0.2$ mm.

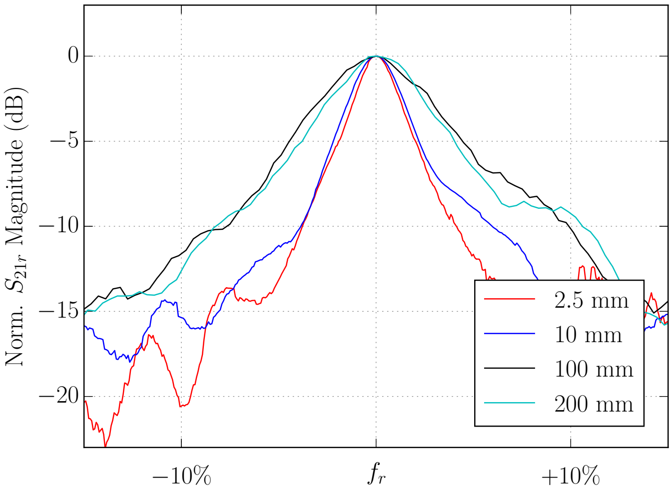

Figure 3.34: Comparison of the normalised S_{21r} measurements for $SL = 2.5$ to 100 mm.

need to hold them in place more firmly during soldering. It is for these reasons that the sizes of the sensors used for experimental work are below 100 mm.

3.6 Liquid Measurements

This section intends to present a variety of liquid measurement results, showing some comparisons with simulations, the effects of slot dimensions and a method to improve performance. Following the discussion of noisy data processing in section 3.4, Fig. 3.35 displays some examples of the SG filtering applied to actual measurement data, where each liquid was measured using a sensor of $SL = 25$ and $SW = 0.5$ mm. Both methanol and water display clear peaks, where the calculation of f_r from the original data would not lead to a large error, but butanol and ethanol show a significantly reduced SNR. The peak amplitude observed in the butanol measurement data certainly aligns very closely with that of the filtered result, but there is an undesirable noise level in the resonant region which would quickly worsen with less than ideal measurement conditions. The ethanol data shows a second peak around 200 MHz above the f_r of the sensor. Measurements of poor SNR, such as Figs. 3.35a and 3.35b, not only display the necessity of filtering, but also accurate simulation. The second peak in 3.35b could present a maximum even after filtering, but simulation data could be easily cross-referenced in real-time by a sensing system and ignore maxima which occur outside of a predetermined domain, or, for example, use such occurrences to signify an error in the industrial process being monitored.

It is worth restating that the sensors modelled in simulations were generally small to ensure reasonable simulation time and accuracy, while still allowing for parametric and sensitivity analysis. In a measurement environment however, slightly larger sensors give rise to improved performance due to a larger effective aperture A_e and RCS, with care taken not to reduce the Q-factor too greatly (see Fig. 2.36). As such, liquid measurements will tend to consider larger sensors in order to improve results, something particularly relevant for the alcohols used in all experimental work. Although there was an effort to maintain room temperature at 21°C, experimental sessions spanned many days and occurred months apart. Additionally, the lab available is used by a number of researchers [3] and so it is not reasonable to assume that the LUTs were always at the same temperature. It is, however, very likely that liquids grouped into a single figure were measured in a short space of time, and for these scenarios the temperature was presumably constant.

---

[3] Each with fierce independent thought as to what constitutes a ‘comfortable’ temperature.

The measured complex permittivity values presented in Fig. 3.3 were imported into CST to provide a comparison with measured data. The sensor geometry used for the measurements presented in Fig. 3.35 was modelled and simulated using the imported LUT permittivity data, where each result can be seen in Fig. 3.35. As the simulated results do not consider a relative measurement, the S_{21} data show dips, rather than peaks, at resonance, where the dashed lines represent the observed resonant frequency. Table 3.6 summarises the difference in the calculated f_r for each liquid, again displaying a relatively low disparity between results. Simulated and measured results are not likely to perfectly agree often due to the fabrication issues highlighted in section 3.2, but the comparisons in Fig. 3.35 and Table 3.6 are reasonably close. Therefore, the use of simulation data for cross-referencing noisy measurements, as mentioned previously, remains viable, and simulations still provide a valuable resource for predictions of sensor behaviour and performance. Although the shape of the curves makes analysis of Q difficult, a qualitative assessment of the broadness of the curves shows consistency between measured and simulated results. That is to say, the comparatively narrow curves observed in methanol and water simulations are also seen in their associated measured S_{21r} results, and the broadness of butanol and ethanol simulated responses are similarly mirrored in measurements.

Table 3.6: Measured f_m and simulated f_s for $SL = 25$ mm and $SW = 0.5$ mm.

Liquid	f_m (GHz)	f_s (GHz)	$\lvert f_m - f_s \rvert$ (MHz)	%
Butanol	1.795	1.838	43	2.40
Ethanol	1.550	1.582	32	2.06
Methanol	1.452	1.410	42	2.90
Water	1.242	1.262	20	1.61

The measured liquid results for the 25 mm sensor are plotted on the same axis in Fig. 3.36, providing a clearer comparison of relative performance. It is clear that the low loss tangent of water produces a superior SNR, where the maximum amplitude is well over 10 dB above the noise level, despite its high permittivity. Methanol provides a peak of much lower amplitude, but one which is still well-defined, particularly if the measurement frequency range was reduced to the area of interest. The lack of definition in the ethanol result is shown more clearly here without y-axis scaling, where an initial observation of the original measurement data without filtering could conclude it to be general noise. Finally, butanol displays a relatively flat peak, but one which certainly provides greater clarity than ethanol. The results in Fig. 3.36 correspond directly with the loss tangents of each liquid, where the liquids of higher

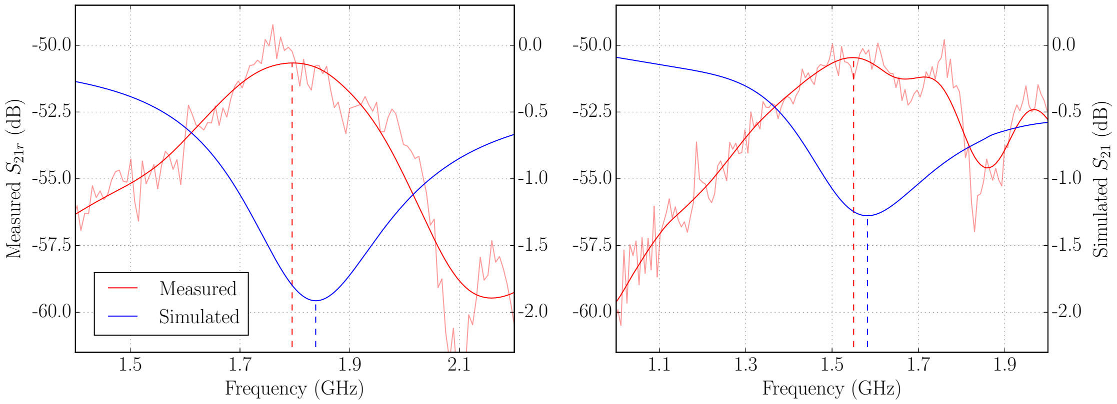

(a) Butanol (b) Ethanol

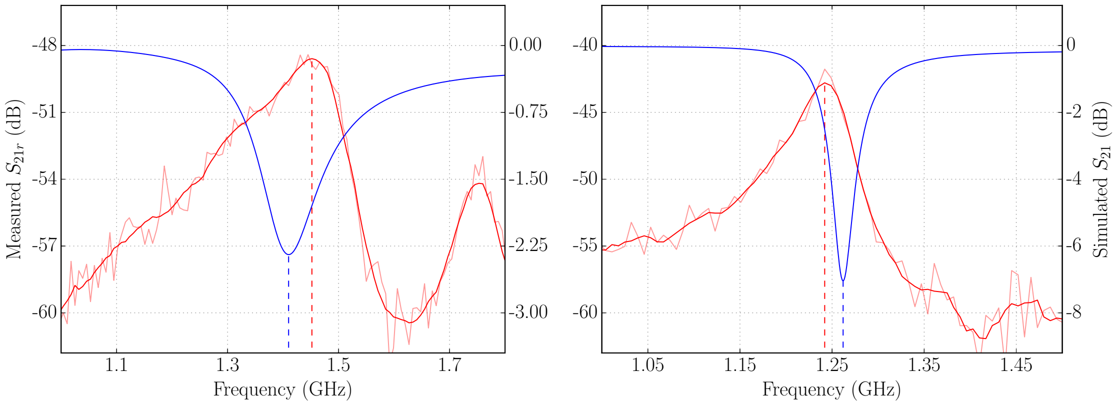

(c) Methanol (d) Water

Figure 3.35: Simulated S_{21} and measured S_{21r} magnitude for all liquids, where $SL = 25$ and $SW = 0.5$ mm.

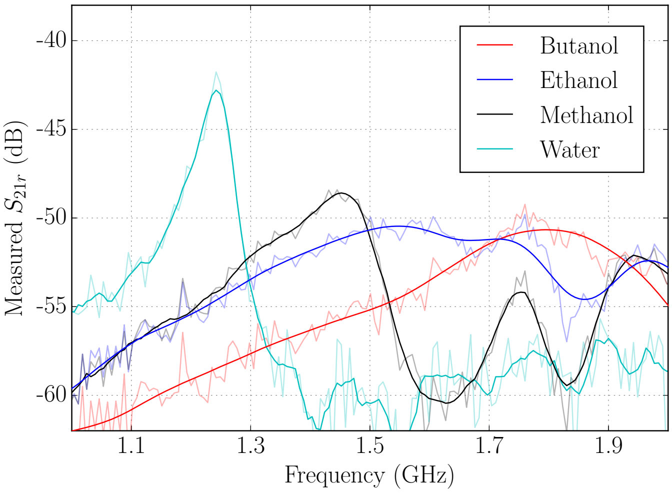

Figure 3.36: Measured S_{21r} magnitude for each liquid, where $SL = 25$ mm and $SW = 0.5$ mm.

loss display a less desirable measurement performance.

The 25 mm sensor was simulated for a number of ε_r samples in the range 1 to 80 in order to obtain enough data points for a satisfactory curve fit. Fig. 3.37 shows the relationship between ε_r and f_r for a simulated sensor of $SL = 25$ and $SW = 0.5$ mm, where the curve fit is of the form:

$$f_r = \frac{a}{\sqrt{c\left(\varepsilon_r\right)^b}} + d \tag{3.9}$$

and the parameters are shown in Table 3.7. Using this fit as a calibration curve, we can use the measured f_r values to return an estimated value for the LUT ε_r, as shown by the dashed lines in Fig. 3.37. The estimated values can be seen in Table 3.8 alongside the measured resonant frequencies and DAK results. These values are not taken to be particularly accurate, as there exists too much variance between measured and simulated results, but are instead intended to display a potential method for determining measured values of ε_r. Through improved reproducibility of sensors, and therefore greater agreement with simulation, a more accurate calibration curve may be possible. Nonetheless, the estimated values are not overly dissimilar to the DAK measured ε_r, where differing temperatures may also reduce the difference between sets of results.

Slot Width Measurements

The set of fabricated sensors used for slot width measurements in Fig. 3.30 provided satisfactory performance for an air-filled pipe, but lack the required A_e for lossy liquid

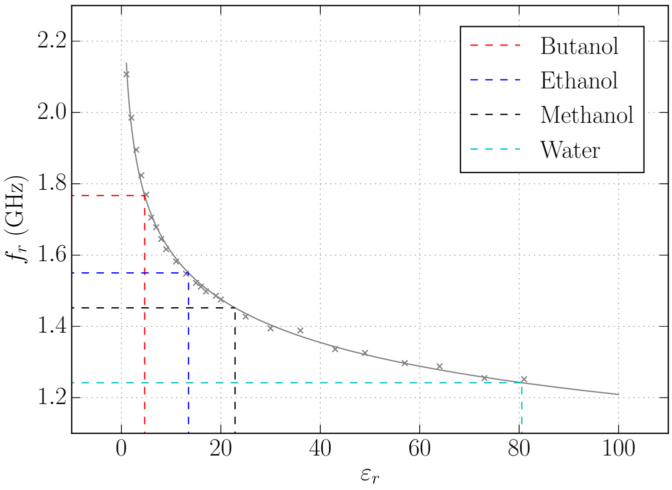

Figure 3.37: Simulated calibration curve showing relation between measured f_r and ε_r.

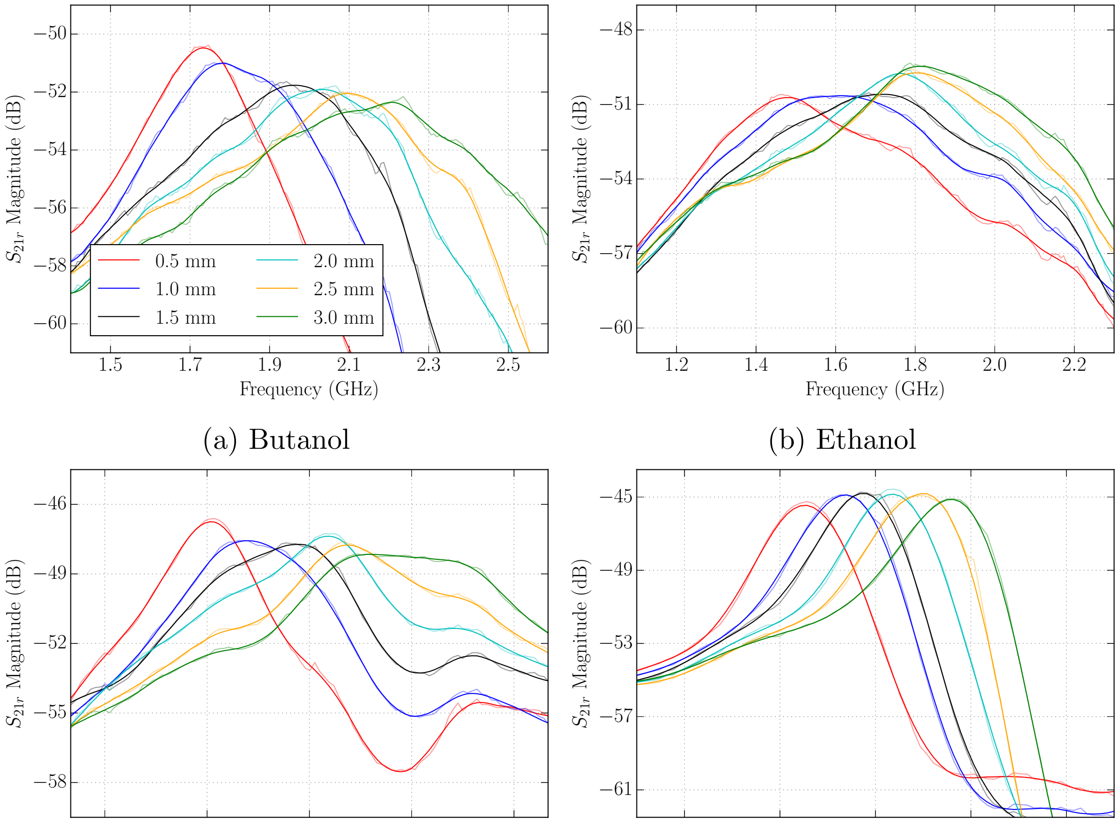

(a) Butanol

(b) Ethanol

(c) Methanol

(d) Water

Figure 3.38: Measured S_{21r} for all liquids for $0.5 \leq SW \leq 3$ mm.

Table 3.7: Parameters of Eq. 3.9 for $SL = 25$ mm and $SW = 0.5$ mm.

Parameter	Value
a	1.453
b	0.245
c	0.454
d	-0.019

Table 3.8: Estimated ε_r using measured f_r values with simulations, compared with DAK results.

Liquid	f_r (GHz)	Estimated ε_r	DAK ε_r
Butanol	1.767	4.68	3.92
Ethanol	1.550	13.49	10.10
Methanol	1.452	22.86	27.35
Water	1.242	80.53	79.60

measurements. Therefore, a set of 6 larger sensors of $SL = 72$ mm were fabricated, with slot widths ranging from 0.5 to 3 mm in 0.5 mm increments. The sensors were intended to be 75 mm long but required trimming due to a fabrication error, hence the somewhat arbitrary SL dimension. The measured S_{21r} magnitudes for each liquid are displayed in Fig. 3.38. It is seen that the majority of measurements display acceptable performance, with notable exceptions shown by some of the ethanol and methanol measurements. The S_{21r} of larger slot widths for ethanol are grouped relatively closely in frequency, and $SW = 1.0$ mm shows a poorly-defined peak. The $SW = 3.0$ mm methanol measurement shows a similarly flat peak, though still appears to have a maximum at a reasonable frequency. The resonant frequency identified by the maximum of each curve shown in Fig. 3.38 can be seen in Fig. 3.39. The liquids show the expected behaviour, where higher values of ε_r result in reduced sensitivity to changes in slot width. Butanol, ethanol, methanol and water showed a f_r percentage change of 27.5%, 21.7%, 17.1% and 12.5%, respectively, over the SW range relative to the $SW = 0.5$ measurement. It should be noted that the calculated resonant frequency of the $SW = 1.0$ mm butanol measurement appears somewhat erroneous, though a qualitative assessment of the corresponding S_{21r} response in Fig. 3.38 shows that the 'true' f_r may exist at a slightly higher frequency, as would be expected from the trends in Fig. 3.39.

Using the same normalisation procedure as Figs. 3.30 and 3.34, the result of each SW measurement is displayed in Fig. 3.40 for each liquid. The $SW = 0.5$ mm

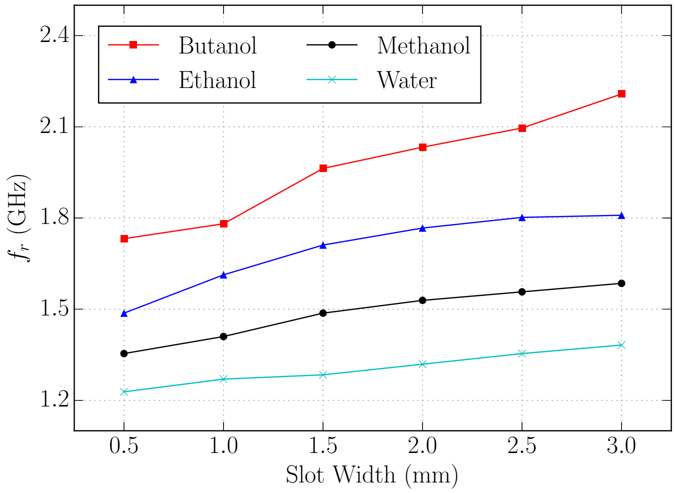

Figure 3.39: Measured f_r for each liquid and $0.5 \leq SW \leq 3$.

Table 3.9: Measured liquid f_r (GHz) for $SL = 72$ mm and $0.5 \leq SW \leq 3$ mm.

	f_r (GHz)			
SW (mm)	Butanol	Ethanol	Methanol	Water
0.5	1.732	1.487	1.354	1.228
1.0	1.781	1.613	1.410	1.270
1.5	1.963	1.711	1.487	1.284
2.0	2.033	1.767	1.529	1.319
2.5	2.096	1.802	1.557	1.354
3.0	2.208	1.809	1.585	1.382

sensor displays the best performance for butanol and methanol, and is near-optimal for ethanol and water, the latter of which is relatively consistent across the entire SW range. This study further compounds the decision to use a 0.5 mm slot width in all measurements not explicitly studying the SW dimension itself.

It is worth drawing attention to the scale of the y-axis used for each liquid, which correlates directly with the LUT loss tangents. The measured f_r for $SW = 0.5$ mm for each liquid was cross-referenced with the measured LUT electrical properties presented in section 3.1, and the approximate $\tan\delta$ values are displayed in Table 3.10. By taking the $SW = 0.5$ mm measurement for each liquid and again normalising, we see a direct comparison in Fig. 3.41. The plot clearly displays the effect of the LUT $\tan\delta$, where the percentage bandwidth is strongly correlated with those values listed in Table 3.10.

Through a study of various liquid measurements concerning the slot width, the lossy nature of the LUTs has been highlighted once more. Using a smaller slot width

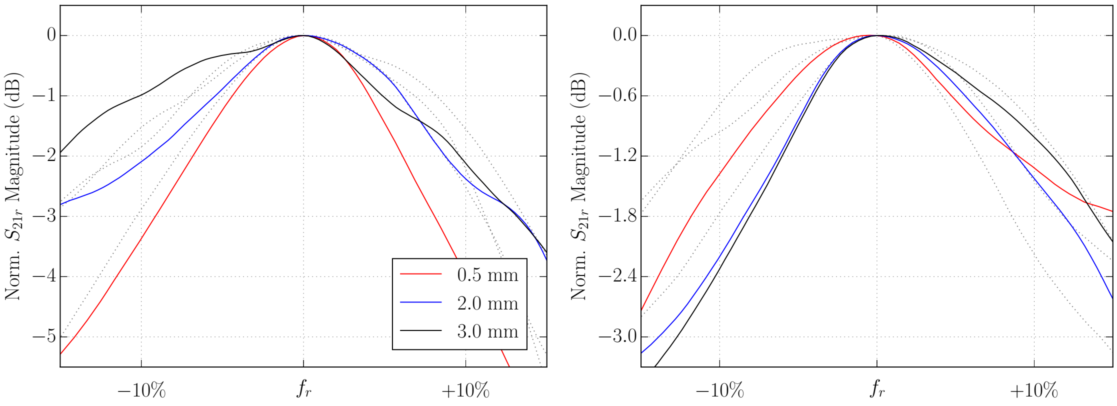

(a) Butanol (b) Ethanol

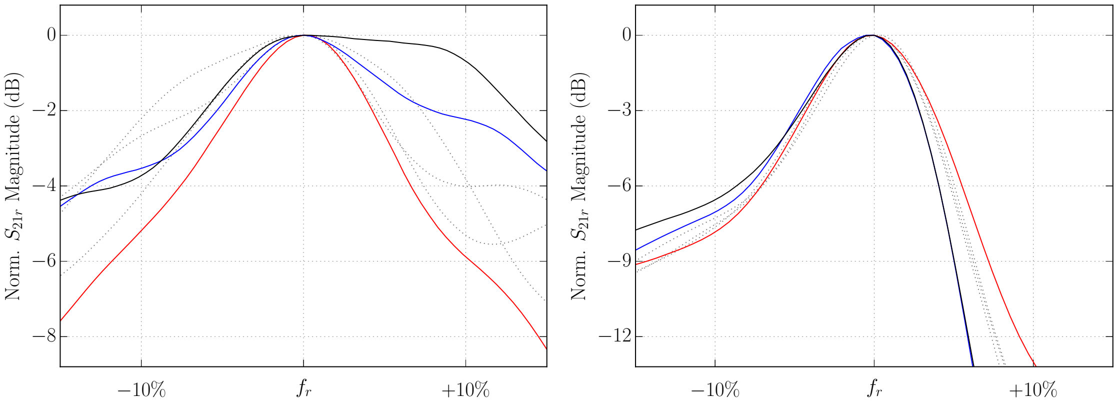

(c) Methanol (d) Water

Figure 3.40: Comparison of the normalised S_{21r} measurements for $0.5 \leq SW \leq 3.0$ mm.

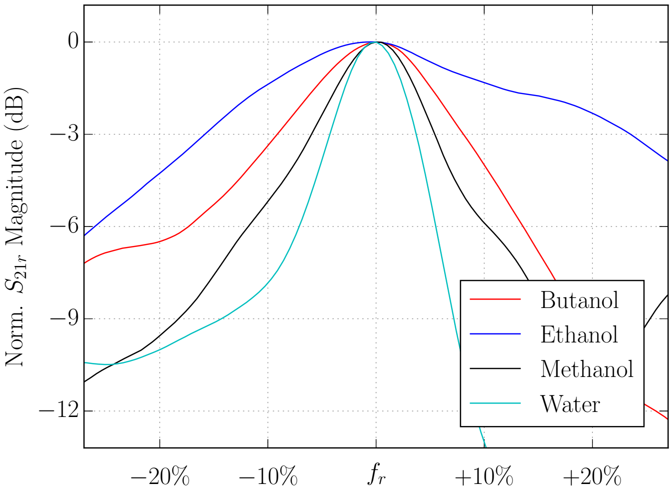

Figure 3.41: Normalised liquid S_{21r} measurements for $SW = 0.5$ mm.

Table 3.10: Approximate $\tan\delta$ at f_r for each liquid.

Liquid	f_r (GHz)	$\tan\delta$
Butanol	1.732	0.676
Ethanol	1.487	0.879
Methanol	1.354	0.385
Water	1.228	0.063

and slot length does improve the Q of the S_{21r} response, but sensors of small SL suffer from reduced amplitude when compared with larger devices, an effect worsened as $\tan\delta$ increases. However, the air measurements have shown that increasing the slot length has its disadvantages in terms of fabrication difficulty, which may compound the associated decrease in Q. It follows that a method to increase the amplitude of the response without the disadvantages of a longer sensor would be desirable. This thesis has so far considered only a single sensor *in situ*, but there is no requirement that this be the case, and multiple sensor measurements form the basis of study in the following section.

3.7 Multiple Sensor Measurements

A single sensor will interact with a portion of an incident wave proportional to its size, where larger sensors will therefore encounter greater amounts of the incoming signal than their smaller counterparts. However, it is possible to avoid the disadvantages of increasing SL too greatly while achieving some of the benefits by placing a number of sensors *in situ*. Ignoring mutual coupling effects and assuming each sensor as an independent resonator, we see that the effective aperture of the group of sensors is increased proportionally with the number present. An example of a 5 sensor configuration was shown in Fig. 3.27, where each sensor is placed some distance apart with the slots aligned. With reference to the field magnitudes shown in Fig. 2.7 it is clear that mutual coupling is likely to impact the resonant frequency of a multiple sensor configuration with respect to the f_r of its individual sensor components.

3.7.1 Effect of Coupling

The proximity of sensors will directly impact the frequency response due to mutual coupling, where we will refer to the edge-to-edge gap between sensors as g. Fig. 3.42 shows an example of two $SL = 25$ mm sensors placed a distance of g apart.

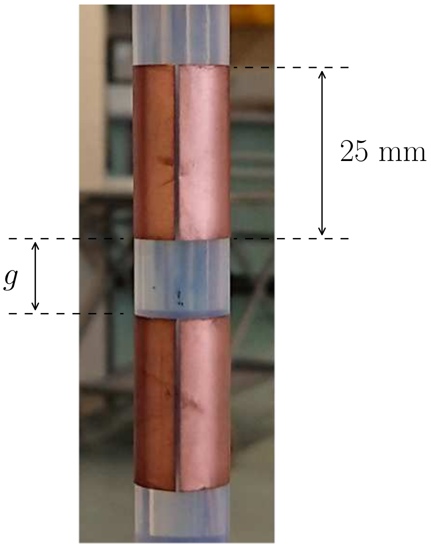

Figure 3.42: Two 25 mm sensors *in situ*, showing the edge-to-edge proximity, g.

To analyse the effect of coupling, two identical sensors of $2.5 \leq SL \leq 10$ mm were simulated for $2.5 \leq g \leq 20$ mm, where the result is displayed in Fig. 3.43. It is clearly seen that the combined resonant frequency of the sensors is decreased as they are moved closer together, and increases at a declining rate as g increases.This would suggest that for a large enough g the sensors would reach a constant f_r, as would be expected, and is presumed to be equal to the resonant frequency of a single sensor of equivalent dimensions, shown by the dashed lines in Fig. 3.43. However, there is a practical limit on the separation of the sensors, as it would not be feasible to continue to separate sensors beyond a certain point, particularly as the number of sensors increases. With reference to Fig. 3.22 we find that the peak amplitude of the response from an individual sensor decreases as its position moves away from the optimal LoS location on the pipe. It was shown by Table 3.2 that certain regions of the pipe receive different amounts of gain from the interrogating antenna based on the offset Δz from LoS. While the calculated Δz ranges appeared to be relatively large for a single sensor, they become more significant for multiple sensors with greater separation. This suggests that while increasing g will reduce mutual coupling, it may be more beneficial to limit the separation to within the ranges in Table 3.2 in order to take advantage of higher levels of received power near to the LoS position.

To assess the measured impact of g, two sensors of $SL = 25$ mm for an air and water-filled pipe were placed 1 mm apart and moved 1 mm further apart for each subsequent measurement. The movement of the sensors was difficult to perform accurately, though care was taken to attempt to remain consistent. Fig. 3.44 displays the normalised S_{21r} magnitudes for air and water, where $1 \leq g \leq 15$ mm.

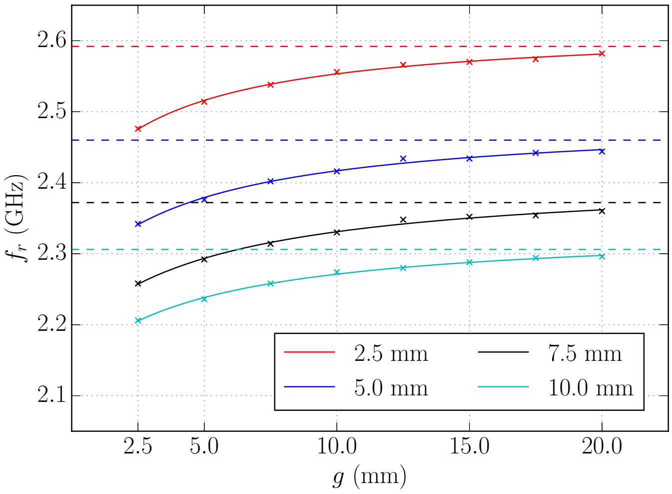

Figure 3.43: Effect of g on simulated f_r for $2.5 \leq SL \leq 10$ mm, where the dashed line shows the resonant frequency of a single sensor.

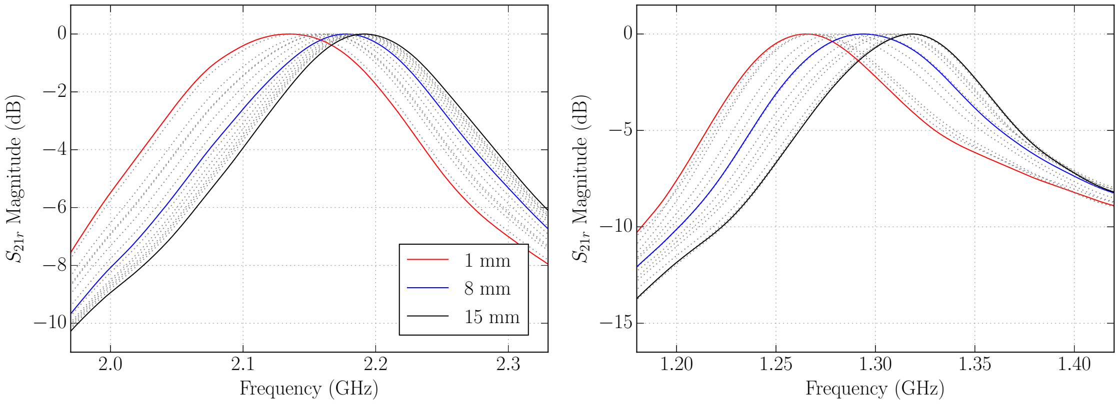

(a) Air

(b) Water

Figure 3.44: Measured S_{21r} of air and water for $1 \leq g \leq 15$ mm.

The increase in f_r with sensor separation is clearly shown for both measurements, confirming the simulated behaviour presented in Fig. 3.43. This measurement highlighted the difficulty in accurately positioning sensors, where a better solution would be necessary in order to use multiple sensors in a practical system requiring well-defined resonant frequencies. The issue is worsened as the number of sensors increases due to the resulting increase in the number of sensor-to-sensor distances which require assessment. One solution could be to etch all sensors in a system onto a single film where the gap between each is accurately controlled in CAD software, resulting in a very low error in g caused only by etching method tolerances. Nonetheless, the use of multiple sensors can still be assessed without any particular analysis of resonant frequencies in order to identify their usefulness in liquid sensing.

3.7.2 SNR Improvement

As has been previously discussed, longer sensors feature a larger A_e and are therefore capable of a greater SNR in measurements, but there exist some disadvantages in increasing lengths beyond a certain point. Increasing the number of sensors on the pipe should overcome these disadvantages, though potentially introduce issues regarding mutual coupling and inconsistencies in their positioning. Despite the difficulty in accurately placing a number of sensors, a separation of $g = 15$ mm was attempted for each result presented here, acting as a compromise between too rapid a change in f_r with Δz and a decrease in the response amplitude.

Five sensors of $SL = 25$ mm and $SW = 0.5$ mm were used for this experiment, where measurements were taken after each sensor was added to the pipe, Fig. 3.45 displays the S_{21r} responses for each liquid as the sensors are introduced. It is immediately clear that multiple sensors significantly improve the measured response for every liquid, with large increases in maximum amplitude and decreases in noise levels relative to the resonant peaks. Additionally, there is no major change in resonant frequency during the addition of sensors, with the notable exception being the initial water measurement. This may be a result of inadvertently deforming the sensor, as discussed in section 3.3.3 with regards to rotation measurements. The maximum amplitude of each measurement is shown in Fig. 3.46, displaying consistent behaviour across every liquid. Table 3.11 lists the maximum amplitude measured with 1 and 5 sensors in place, A_0^1 and A_0^5, respectively, along with the total change in peak amplitude ΔA_0. Again, we see that each liquid is displaying a significant rise in amplitude, where butanol in particular yielded a gain of over 10 dB.

Table 3.11: Change in maximum S_{21r} amplitude A_0 for a single A_0^1 and five A_0^5 sensor measurement.

Liquid	A_0^1 (dB)	A_0^5 (dB)	ΔA_0 (dB)
Butanol	-50.662	-40.471	+10.191
Ethanol	-50.597	-43.751	+6.846
Methanol	-48.656	-38.890	+9.766
Water	-40.020	-31.105	+8.915

The amplitude increase would not be particularly helpful if it occurred across the entire frequency range, as secondary peaks, such as the one seen in Fig. 3.45c for the methanol measurement, would still present the possibility of a peak-detection error. However, this does not appear to be the case, where for this example in particular we observe almost 10 dB of gain at f_r and less than 5 dB at the secondary peak,

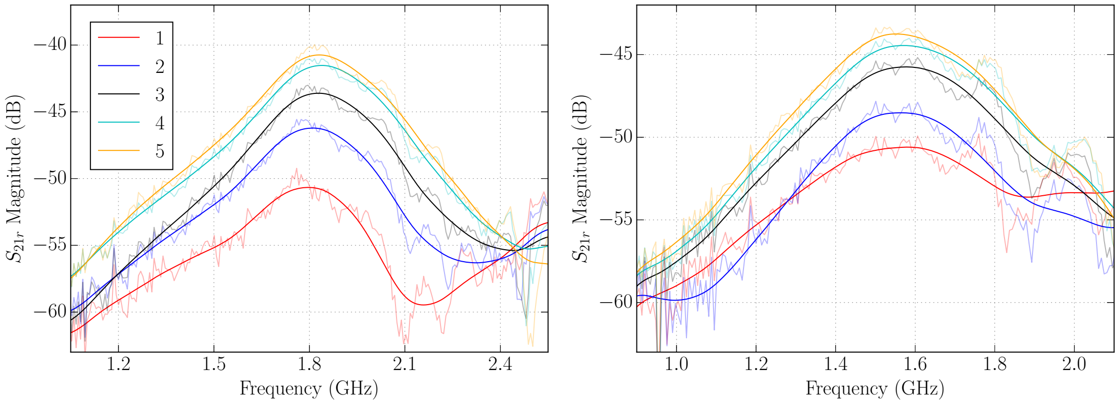

(a) Butanol

(b) Ethanol

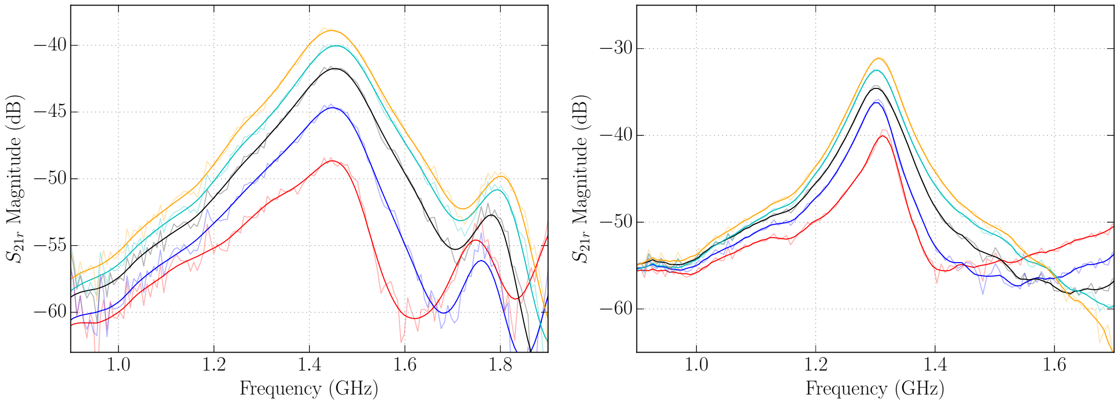

(c) Methanol

(d) Water

Figure 3.45: Measured S_{21r} magnitude for 1 to 5 sensors.

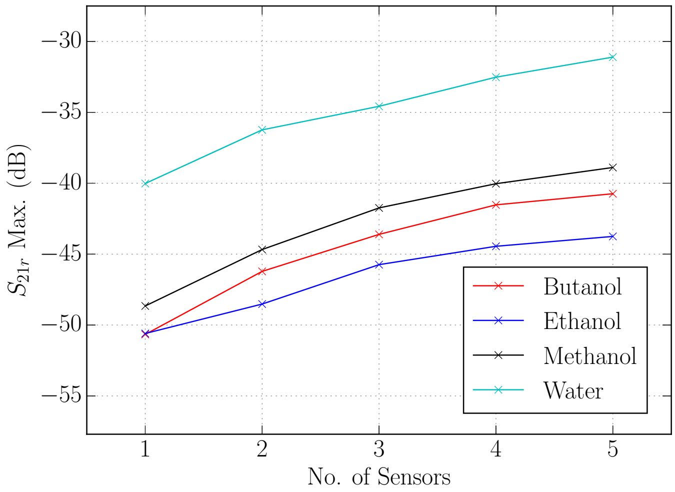

Figure 3.46: Increase in S_{21r} maximum amplitude with number of sensors.

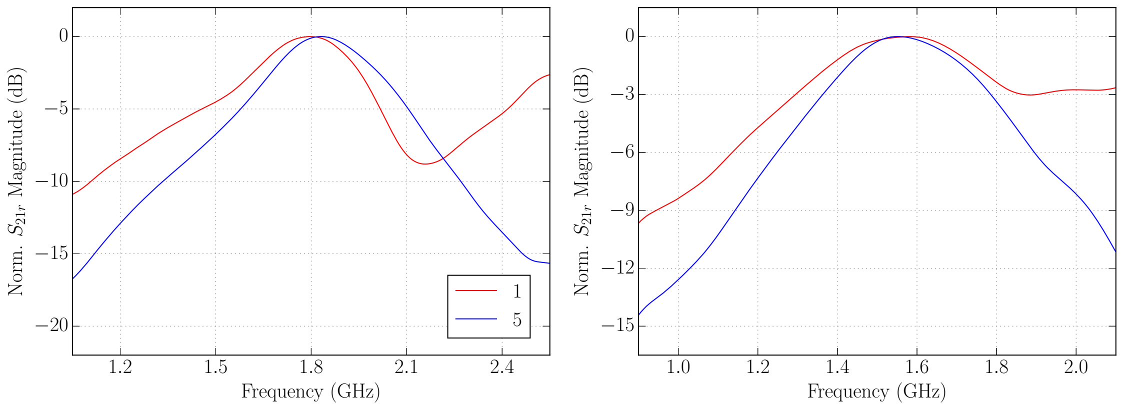

(a) Butanol (b) Ethanol

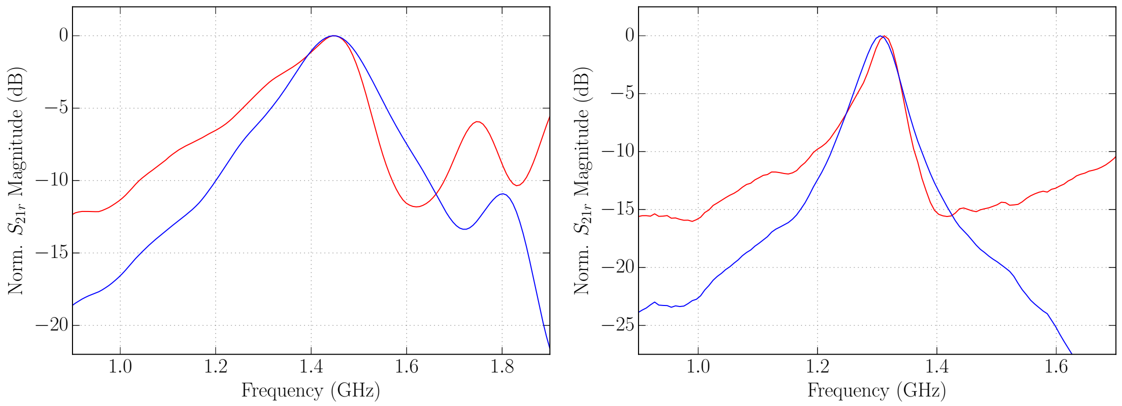

(c) Methanol (d) Water

Figure 3.47: Normalised S_{21r} magnitude for 1 and 5 sensors.

where the difference between the two amplitudes has approximately doubled when comparing five sensors with one. Fig. 3.47 shows the normalised S_{21r} magnitudes for the 1 and 5 sensor measurements of each liquid, highlighting the performance improvement perhaps even more clearly, where background noise and secondary peaks are reduced significantly. In every case, the measured response is markedly improved by adding multiple sensors, with significant increases in A_0 and more satisfactory curve profiles in general. There is no reason for limiting this experiment to five sensors other than the availability of fabricated devices, where increasing the number would almost certainly improve the measured response further. It is worth noting, however, that the antenna distance will impact the effectiveness of sensors as their position moves away from the LoS position, as discussed in section 3.3.4, where an example of the relative received power over different sections of the pipe was shown in Fig. 3.23.

Figure 3.48: Example of a multiple pipe measurement.

3.7.3 Simultaneous Measurement

The discussion of multiple sensors introduces the idea of simultaneous measurements making use of the same pair of antennas, provided the pipes and sensors are in reasonably close proximity. Fig. 3.48 shows a 3D modelled example of such a configuration, where three pipes are placed in the experimental frame, filled with different liquids and sensors. Provided that the resonant frequencies of the sensors do not overlap too closely, the S_{21r} magnitude measurement should display three distinct peaks, allowing the monitoring of three LUTs simultaneously.

The experimental frame shown in Fig. 3.15 was adjusted, with regular 5 cm holes, to allow for the fitting of multiple PTFE pipes of the same dimensions. Two pipes were placed into the frame, where one was filled with water and the other methanol. The experiment featured three sensor configurations, the results of which can be seen in Fig. 3.49. For the initial measurement (Meas 1), the water and methanol pipes were fitted with a single sensor of $SL = 72$ and $SL = 50$ mm, respectively. The result shows a relatively large difference in A_0 for the water and methanol resonances, as expected given the respective loss tangents of the LUTs. Measurement 2 improves the methanol amplitude by placing 3 × 50 mm sensors on the pipe, but also the water amplitude with 3 × 25 mm sensors. The resulting S_{21r} measurement reduces the frequency separation of the resonances, where the methanol peak could appear to be unwanted background noise. Finally, measurement 3 returns to a single 72 mm sensor on the water pipe, and 3 × 25 mm sensors on the methanol pipe. The result shows good frequency separation with well-defined peaks, along with an improved

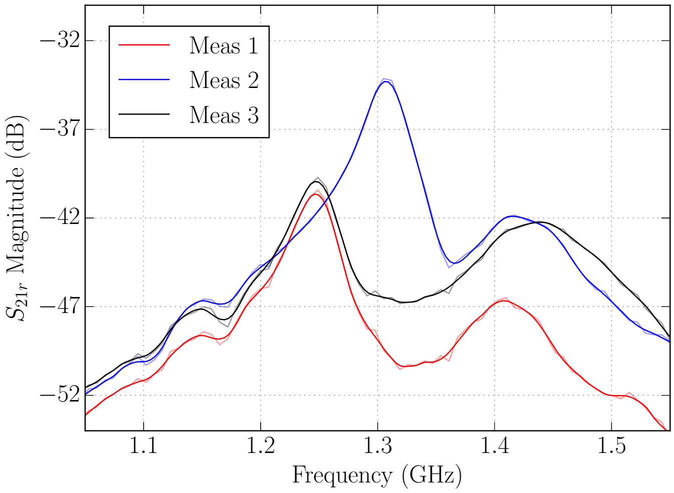

Figure 3.49: S_{21r} magnitude of two multiple pipe measurement configurations.

relative amplitude for each resonance. Fig. 3.49 is used to display the adaptability a multiple sensor, multiple liquid measurement configuration. Resonant peaks may be adjusted in frequency by using sensors of different SL or SW, and in amplitude by adding or removing sensors from each pipe. Provided that the LUTs are known, the f_r for each liquid can be easily determined for a given sensor configuration and monitored simultaneously in real-time.

In order to expand the concept of simultaneous measurements, two pipes filled with water and butanol were placed alongside an empty pipe in the frame. The water pipe was configured with 4 × 25 mm sensors, the butanol pipe with 3 × 50 mm, and the empty pipe with a single 25 mm sensor. The resulting S_{21r} measurement is shown in Fig. 3.50, displaying three clear resonant peaks corresponding to water, butanol and air. Naturally, the butanol resonance is of a lower Q-factor, though this result could be improved by the further addition of sensors onto the butanol pipe, and perhaps removal of some devices from the water pipe.

The adaptive nature of the sensor geometry allows for multiple simultaneous measurements across a wide frequency, ε_r and $\tan\delta$ range. For high-loss LUTs, the addition of sensors can improve the SNR of individual resonant peaks and increase their amplitude relative to neighbouring peaks resultant from liquids of lower loss, such as water. Additionally, for LUTs whose resonances occur relatively closely in the frequency domain such as water and methanol, different sensor geometry can adjust the measured f_r and ensure improved isolation. Due to available resources the study of further pipes was not assessed, but it would follow that additional LUT resonances are possible provided that all liquids present are of suitable permittivities to enable satisfactory peak separation in the S_{21r} result.

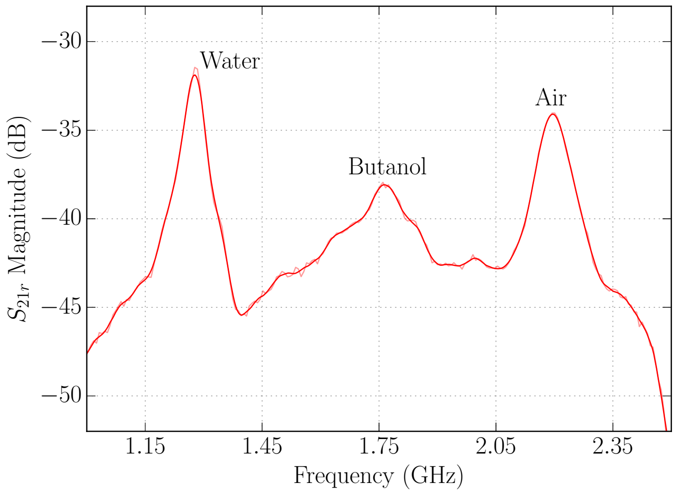

Figure 3.50: S_{21r} magnitude of a three pipe measurement.

3.8 Measurement Accuracy

This thesis has discussed issues of differences between measurement and simulation regarding fabrication issues, Mylar bending and *in situ* sensor movement, which have all shown to have a noticeable effect on the measured resonant frequency. This section attempts to quantify environmental effects on measurement uncertainty, for near-constant conditions, for each liquid. The impact is expected to be low, as we consider the main source of uncertainty to be related to movement of equipment, as studied in section 3.3.1, or deformation of the sensor itself. The LUT was added to the pipe and placed in the anechoic chamber with its sensor in place, where it was left for approximately one hour. During this time, the room temperature was held at 22°C, the VNA was operating along with the measurement antennas, and lights in the chamber remained switched on. The LUT was subsequently measured ten times over the course of ten minutes, where the sensor was not touched at any point prior to or during readings. These steps should ensure that remaining deviation in the measured f_r is a result of random or systematic uncertainty related to the environment and VNA, and not caused by reasons listed previously. Using the measured resonant frequencies for each set of results, the mean $\overline{q}$ can by calculated as:

$$\overline{q} = \frac{1}{n}\sum_{i=1}^{n} q_i = \frac{q_1 + q_2 + ... + q_{n-1} + q_n}{n} \tag{3.10}$$

where q_i is the measured f_r. Assuming the results are evenly distributed about $\overline{q}$, we can assume a Gaussian probability density function. Subsequently, the standard uncertainty, or standard deviation of the mean, can be determined as:

$$u = \frac{\sigma}{\sqrt{n}} = \sqrt{\frac{1}{n\left(n-1\right)}\sum_{i=1}^{n}\left(q_i - \overline{q}\right)^2} \tag{3.11}$$

where σ is the standard deviation. Therefore, the measurement may be expressed as $f_r = \overline{q} \pm u$ for a 68% confidence level, or $\pm 2u$ and $\pm 3u$ for a 95% and 99% confidence level, respectively. The estimated measurement uncertainty for each liquid for different confidence levels can be seen in Table 3.12. The figures, as expected, are not particularly high, where the uncertainty for a 95% confidence level represents a deviation of 0.16%, 0.22%, 0.15%, and 0.20% of the mean for the liquids in order of listing.

Table 3.12: Estimation of measurement uncertainty.

		u (± MHz)		
Liquid (cm)	$\overline{q}$ (GHz)	68%	95%	99%
Butanol	1.759	1.366	2.732	4.099
Ethanol	1.525	1.708	3.415	5.123
Methanol	1.413	1.067	2.134	3.201
Water	1.278	1.306	2.613	3.919

3.9 Conclusion

The liquids selected for measurements display a wide range of permittivity, both real and imaginary parts, allowing for a more comprehensive study of the sensor performance for different conditions. This chapter has presented an assessment of the robustness of the sensor with regards to various aspects of the practical measurement environment. It was shown to operate well over reasonable read distances, though practical limitations did not allow for the study of distances beyond 80 cm. Additionally, the rotational and vertical position of the sensor is non-critical and allows for the non-rigorous placement of devices, where performance may still be improved when the slot is facing directly towards the transmitting antenna in its line of sight. Changes in antenna polarisation induced relatively small differences in measured results, where only minor changes in resonant frequency were observed until the total rotation approached 45°. A brief discussion on data processing provides a potential real-time method to monitor lossier liquids in noisy environments without reducing measurement accuracy. Measurements of changes in slot width and length are provided to corroborate simulated and theoretical results, as well as an assessment of effects on sensor performance. Liquid measurements display the impact of lossy liquids on the quality of measured results, where butanol and ethanol results are seen to be significantly worse than methanol and water, where the latter LUT performs particularly well in every circumstance. It is shown that using multiple sensors on a single pipe provides a method to mitigate losses and significantly improve sensor performance, though there should be some consideration of mutual coupling effects. As well as multiple sensors, measurements using a single pair of antennas may monitor multiple liquids simultaneously, provided adequate separation in the frequency domain. A brief discussion on measurement uncertainty concludes that there is no major source of random or systematic uncertainty related to environmental effects, where results display only minor variations in resonant frequency. This chapter again shows that the proposed sensor is highly adaptable to various changes in environment and for different applications. The use of additional sensors provides an incredibly simple method to enable the measurement of high-loss liquids, and their spacing provides a further parameter with which we may tune resonance appropriately.

Chapter 4

Further Applications

This chapter will assess further potential applications of the sensor, exploiting its geometry and sensitivity for liquid level sensing, as well as temperature monitoring.

4.1 Use of Geometry as a Level Sensor

Results and simulations have thus far only considered a homogeneous dielectric region within the liquid cavity, that is to say, a pipe either entirely filled or empty. Consider the pipe placed vertically, with the LUT filling it from the bottom, where the liquid cavity now consists of two dielectric regions, the LUT and air. As the LUT travels further upwards, the liquid cavity within the sensor trends from air filled to entirely liquid filled, as displayed by Fig. 4.1. The resonant frequency of the sensor should consequently shift from the higher, air filled frequency f_0, to a lower frequency f_L which is dependent on the LUT. The level sensing application could be used in a number of ways. One example is as a low-cost liquid level meter, where the level in the sensor relates to a volume of some liquid in a processing tank in an industrial process. Should the tank drop below some threshold volume or pressure, an offshoot pipe fitted with a sensor would rise above a predetermined frequency response due to the decrease in liquid level. A second example is that of a Venturi flow meter as shown in Fig. 4.2. Fluid flowing through a pipe of cross-sectional area A_1 at a velocity V_1 reaches a tapered transition to a section of reduced size A_2, through which the velocity increases to V_2. The resulting difference in pressure caused by the velocity differential is measured *via* an attached manometer, which shows a difference in liquid level Δh used to calculate the initial flow velocity V_1. This thesis considers two level measurement configurations, using a single sensor for continuous level analysis, or multiple sensors for a discretised approach.

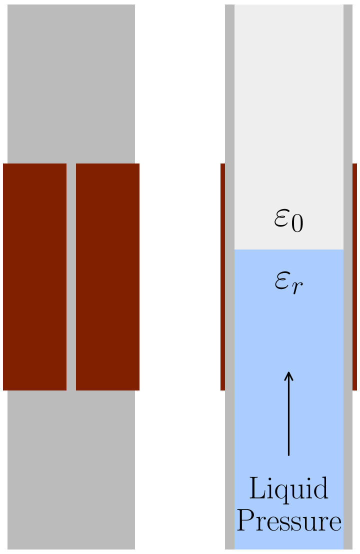

Figure 4.1: Diagram of a single sensor with liquid of permittivity ε_r filling from the bottom *via* external pressure.

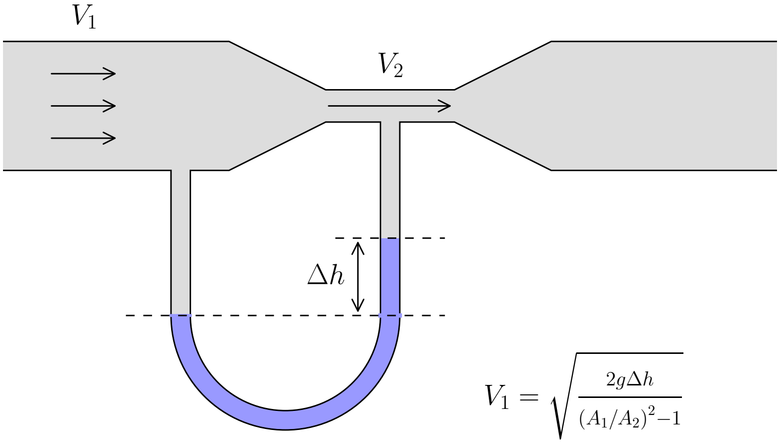

Figure 4.2: Example of a Venturi flow meter, where the difference in liquid level is used to calculate the flow velocity V_1.

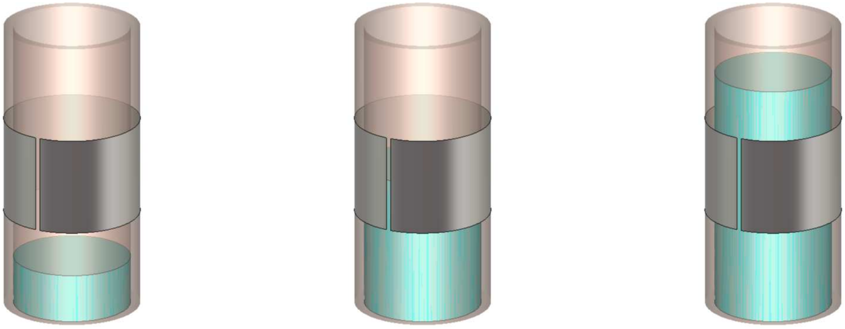

Figure 4.3: Model used for single sensor level simulations, showing three liquid levels.

4.1.1 Single Sensor

This section will study the use of a single sensor as a level measurement device, showing that there is a continuous decrease in resonant frequency as the LUT rises through the sensor. Simulations are slowed considerably with the introduction of modelled liquids, as a result of volumes of relatively high permittivity occupying large areas of the simulation domain. This problem is worsened as ε_r increases, and begins to become impractical when large numbers of simulation runs are necessary. This is the case, unfortunately, when attempting to model rising liquid levels, where the level must be simulated at regular height intervals necessitating a great number of simulations. For this reason, simulated liquids within this section will generally have relatively low ($\varepsilon_r < 10$) values of permittivity.

Simulation

An example of the simulated model for a sensor of $SL = 10$ mm is shown in Fig. 4.1, where the liquid level can be seen at three different stages. The level was simulated over the range of -10 to 20 mm, where 0 mm refers to the base of the sensor, for a permittivity range of $2 \leq \varepsilon_r \leq 8$. The result can be seen in Fig. 4.4, where the grey area signifies that the LUT level is inside the sensor cavity. It is shown that higher permittivities result in a greater change in f_r over the level change, as would be expected. The rate of change of resonant frequency is fastest as the LUT enters the sensor cavity, and also begins to change even prior to this point. It is clear that the fringing fields have a significant impact on the resonant frequency of the sensor, where for $\varepsilon_r = 8$ we see that f_r begins to decrease when the liquid level is around 5 mm below the base of the sensor, and similarly does not become constant until a similar level above the sensor is reached.

The inhomogeneous region inside of the pipe cavity, created as the LUT level rises, is comprised of a liquid of permittivity ε_r and the air above it, this can be

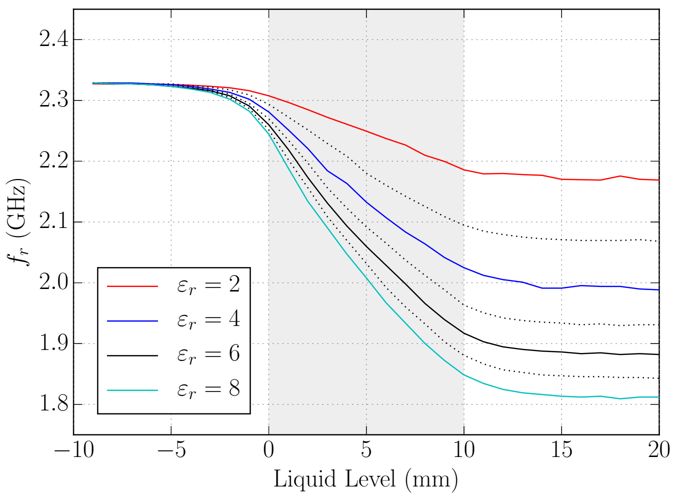

Figure 4.4: Simulated f_r as liquid level rises, where $2 \leq \varepsilon_r \leq 8$.

seen in Fig. 4.5. Therefore, the effective permittivity ε_e of the cavity is some function of ε_r and ε_0, which trends from $\varepsilon_e = \varepsilon_0$ to $\varepsilon_e = \varepsilon_r$ as the LUT rises through the sensor. By simulating a sensor filled with a liquid of varying ε_r, the effective permittivity of the cavity during a level rise can be estimated by comparing the resonant frequency observed at each level with the same f_r from the full-pipe simulation. Using this comparison we extract a range of effective permittivity values which represent different stages during a level rise.

The sensor in Fig. 4.3, $SL = 10$ mm, was used to simulate a rising level for LUTs of $\varepsilon_r = 2$, 4, 6 and 8, where the liquid level ranged from -5 to 15 mm. Additionally, the same sensor was filled with a liquid of $1 \leq \varepsilon_r \leq 8$ and simulated. The resonant frequencies observed at each point during the level simulations were cross-referenced with the full-pipe results to estimate a range of effective permittivities. For example, for a liquid level far below the sensor we would expect an effective permittivity of $\varepsilon_e = 1$, given that the LUT has yet to reach the sensor or significantly perturb fringing fields. Conversely, for a level far above the top edge of the sensor we would expect $\varepsilon_e = \varepsilon_r$, as the liquid fills the entire sensor and all fringing field areas. The results of the simulation are shown in Fig. 4.6. As the liquid level approaches the sensor, the effective permittivity is seen to be slightly greater than 1, where higher permittivities show a slightly increased ε_e. The effective permittivity rises as the level increases within the sensor cavity, and grows at a decreasing rate as the liquid level surpasses SL, trending towards ε_r. An effective permittivity of 1 would require an empty pipe, and to achieve $\varepsilon_e = \varepsilon_r$ an infinitely high liquid level is necessary, but Fig. 4.6 shows that levels of a few cm beyond either of the sensor edges would suffice. It would be expected that ε_e would behave relatively similarly for different

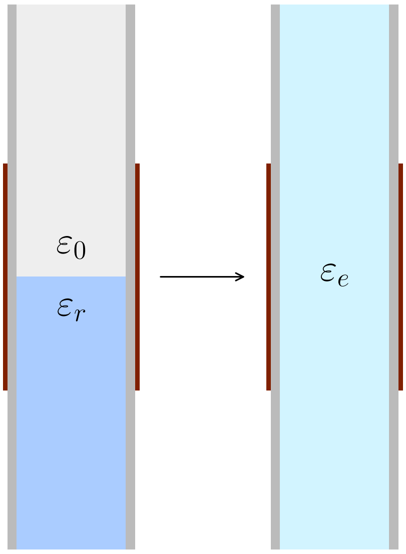

Figure 4.5: Diagram of an equivalent permittivity liquid representing an inhomogeneous sensor cavity.

sensor lengths albeit at different rates, as it must trend from 1 to ε_r. However, the difference in fringing field behaviour for different sensor geometry will affect ε_e in different ways, particularly for liquid levels outside of the sensor cavity.

Parametric Study on Level Sensitivity

The concept of replacing the inhomogeneous region with a homogeneous equivalent, as shown in Fig. 4.5 and assessed in Fig. 4.6, is potentially useful in understanding sensor behaviour during level measurements. Similarly to section 2.3.2, a parameter study is also important for modelling such measurements, as well as for aiding in the selection of appropriate sensor geometry suitable for the particular application.

Slot Length

The size of the sensor will have an obvious impact on its sensitivity to level changes, where a larger SL will be less sensitive than a smaller slot length per unit change in level. For example, if we take two sensors of $SL = 5$ and 10 mm, twice as much liquid is required to fill the larger sensor, but the total change in frequency will certainly not be doubled, resulting in a smaller change in resonant frequency Δf_r per unit level rise. Using these slot length dimensions, and $SW = 0.5$ mm, with a liquid of $\varepsilon_r = 9$, the approximate Δf for $SL = 5$ and 10 mm is 326 and 398 MHz, respectively, resulting in sensitivities of 65.2 and 39.8 MHz per mm. From this brief example it is clear that if high levels of sensitivity are required, and specifically for

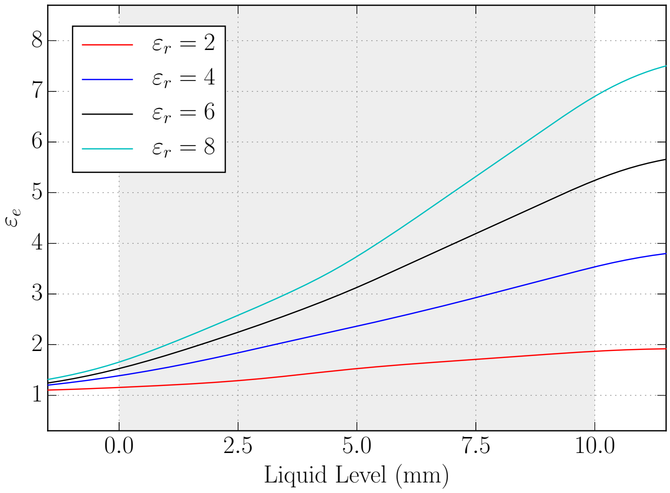

Figure 4.6: Effective permittivity of equivalent homogeneous liquid as level rises.

small dynamic level ranges, a smaller slot length is advised, and *vice versa*.

The effect of fringing fields at either end of the sensor was alluded to in discussion of Fig. 4.4, where it was seen that the resonant frequency begins to decrease before the level reaches the bottom edge of the sensor. It was also shown that the point at which this decrease is observed moves further away from the sensor as permittivity increases, but this distance will also change in relation to SL. As the sensor length decreases the effect of fringing fields will have a greater impact on f_r and general sensor behaviour, where the energy stored in these fringes at resonance becomes larger relative to the total energy stored for smaller sensors. This effect can be shown by comparing level simulations of sensors with different SL and observing the rate of change of f_r in the regions outside of the sensor. Fig. 4.7a shows the simulation of four sensors, $SL = 2.5$, 5.0, 10.0 and 20.0 mm, over a level range of -5 to $+5$ mm with respect to the sensor, for a liquid of $\varepsilon_r = 9$. For better comparison, the levels which are positioned within the sensor are omitted and replaced with a normalised level range, where the grey area denotes these regions. A qualitative assessment shows that the change in f_r within the sensor increases for larger sensors, suggesting that a greater portion of the frequency decrease occurs within the sensor cavity as SL increases, that is to say, larger sensors appear to be less sensitive to level changes which occur within the fringing field regions. The simulated data can be arranged such that the linear change in frequency from f_{-5} to f_{+5} is presented in terms of a percentage, where the total change $f_{-5} \rightarrow f_{+5}$ represents 100%, as seen in Fig. 4.7b. It should be noted that, despite the rising curves, this plot represents a decrease in resonant frequency. The result makes it immediately clear that the smaller sensors experience a larger amount of the total frequency change during level positions which

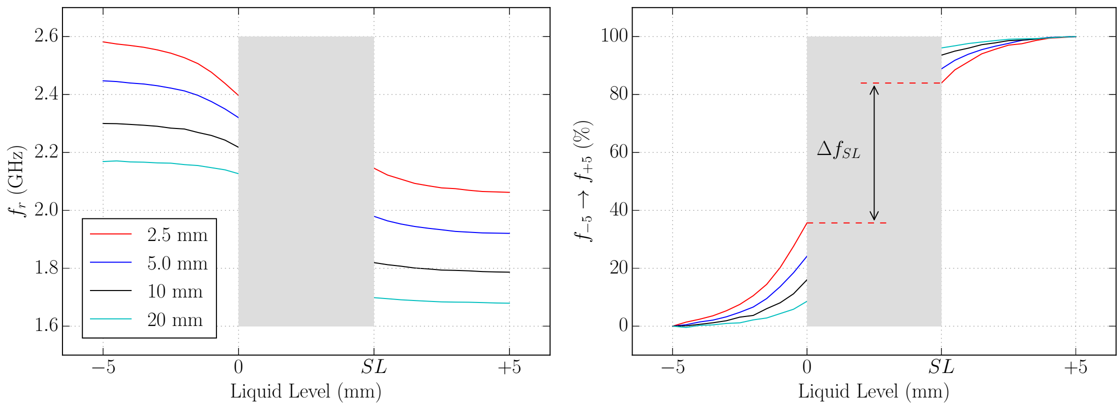

(a) f_r for different SL.

(b) Percentage change from f_0 to f_L.

Figure 4.7: Simulation of liquid level for sensors of different slot length, $\varepsilon_r = 9$.

are outside of the sensor cavity. Indeed, the change in f_r observed over the level range of 0 to SL for $SL = 2.5$ mm represents less than half of the total change, where $\Delta f_{SL} = 48.3\%$, compared with 87.5% for $SL = 20$ mm. Fig. 4.7 shows that the sensitivity to level changes within the fringing field regions above and below the sensor is significantly increased for smaller values of SL.

Slot Width

The effect of slot width on level sensitivity will simply reflect the behaviour displayed by Figs. 2.33 and 2.34, where larger slot widths slightly increase sensitivity to changes in permittivity within the pipe cavity. Fig. 4.8a shows the result of a level simulation, where the LUT level rose from 0 to 10 mm, for sensors of varying SW, and the resultant sensitivity values are plotted in Fig. 4.8b, where f_0 is taken to be f_r at level = 0 mm. We see the expected behaviour, where an increase in the slot width causes an increase in sensitivity.

Pipe Radius

Calculating the cylindrical volume, $V_c = \pi r^2 h$, for $5 \leq r \leq 11$ and $SL = 10$ mm, we are able to assess the sensor sensitivity versus radius. Fig. 4.9b plots the total frequency change observed for each sensor in Fig. 4.9a divided by the associated LUT volume required for a 5 mm level rise. The pipe wall width was set to 1 mm for each r. Though not intended to be scientifically rigorous, Fig. 4.9b provides a graphical representation of the vastly reduced volumes of liquid required to achieve significant changes in f_r. Of course, the reverse scenario is true, where a larger radius would provide reduced sensitivity to much greater volumes of liquid.

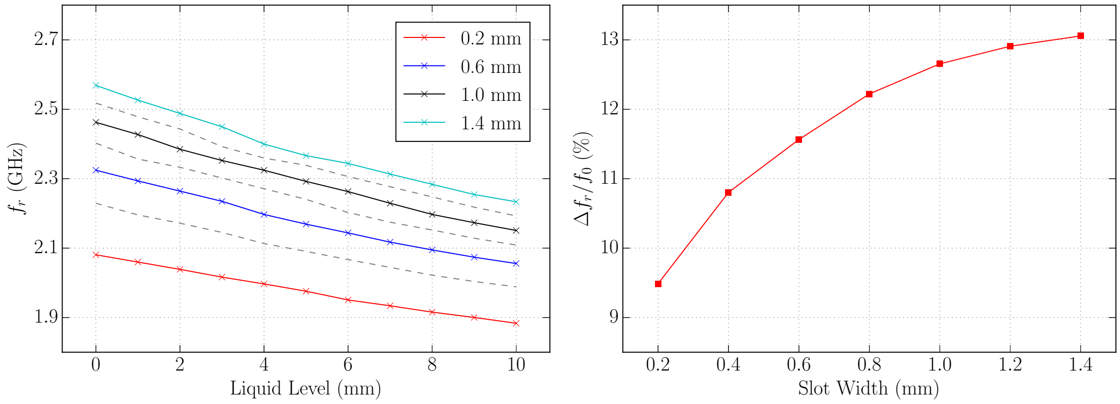

(a) f_r versus liquid level.

(b) Sensitivity to liquid level.

Figure 4.8: Simulation of liquid level for sensors of $0.2 \leq SW \leq 1.4$ mm, $\varepsilon_r = 4$. The change in frequency Δf_r is the difference between a level of 0 and 10 mm for each SW.

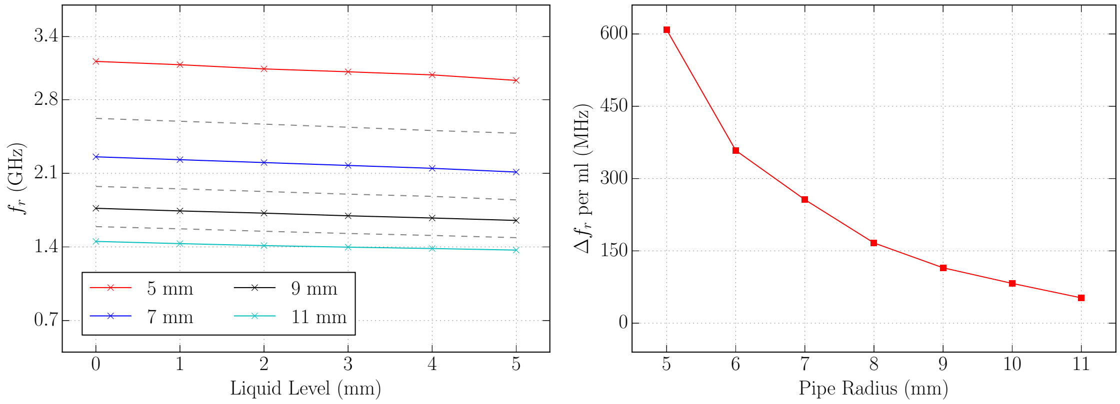

(a) f_r against level for different r.

(b) Sensitivity to liquid volume.

Figure 4.9: Simulation of liquid level for sensors of $5 \leq r \leq 11$ mm, $\varepsilon_r = 4$. The change in frequency Δf_r is the difference between a level of 0 and 5 mm for each r.

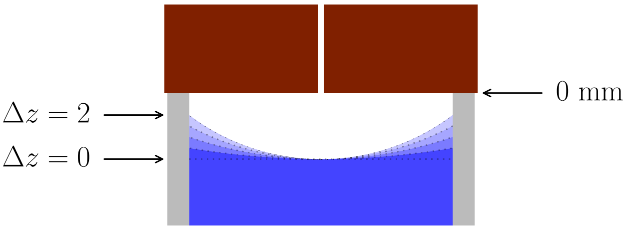

(a) Diagram of simulation.

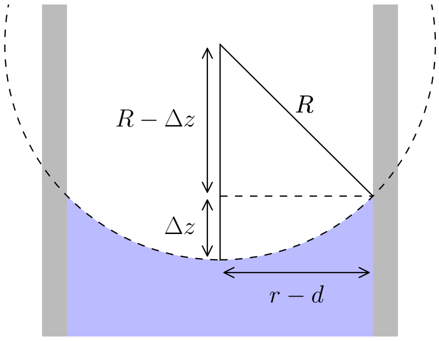

(b) Geometry of meniscus shape.

Figure 4.10: Method used to simulate a spherical meniscus.

Effect of Meniscus

Simulations have shown the sensor to be highly sensitive to very small changes in liquid level, where even fractions of a millimetre can be significant, especially as ε_r increases. As a result, it is worthwhile to study the effect of the meniscus which will form on the liquid surface, examples of which can be seen in Fig. 4.10a. It can be seen that the meniscus curvature causes a difference in liquid level between the edges and centre of the pipe, Δz, where $\Delta z = 0$ represents a flat surface. The outer regions of the liquid surface will exist Δz mm further into the sensor, and the electric field near the slot will encounter the liquid at a given height before the centre of the surface reaches it.

As with prior level simulations the bottom of the sensor is defined as a liquid level of 0 mm, shown in Fig. 4.10a, where the top of the meniscus is used as the level position reference. The shape was assumed to be a spherical cap, where a modelled sphere was geometrically subtracted from the liquid surface to create simulations for $0.5 \leq \Delta z \leq 2.0$ mm. The radius of the sphere was calculated as:

$$R = \frac{(r-d)^2 + (\Delta z)^2}{2\Delta z} \tag{4.1}$$

where the geometry is shown in Fig. 4.10b. The significance of the effect of the meniscus on f_r is expected to be small for low values of ε_r, indeed, inconsistencies

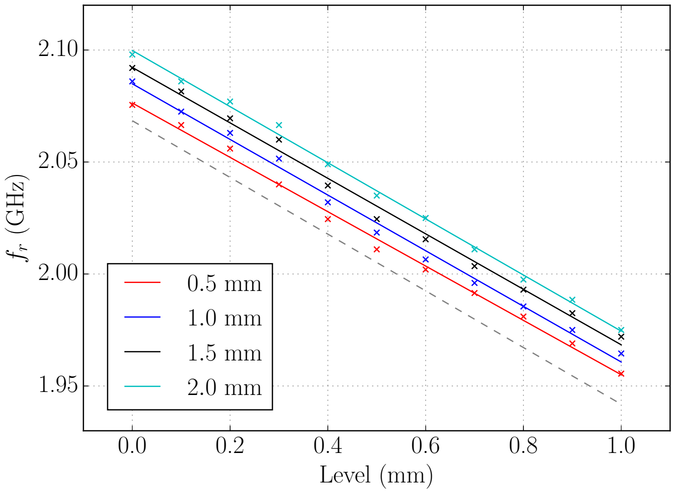

Figure 4.11: Simulated f_r over a 0 to 1 mm water level rise for varying Δz, with $\Delta z = 0$ mm (dashed) for comparison. $SL = 15$ mm.

resultant from increased meshing complexity slightly obscured any potential impact. However, the result of a water ($\varepsilon_r = 78.4$) level simulation for $0.5 \leq \Delta z \leq 2.0$ mm can be seen in Fig. 4.11, where the dashed line represents a completely flat surface. As mentioned, the added complexity of the geometry resulted in somewhat erratic results, where the change in resonant frequency was assumed to be roughly linear over the level range and the fit lines are subsequently of the form $y = ax + b$. The simulations show that there is a definite effect, where lower values of Δz result in a lower frequency response for a given liquid level. This is intuitive in that a greater volume of the LUT will be present inside of the sensor at a defined level as Δz decreases, where a flat surface $\Delta z = 0$ represents the maximum possible volume. The differences in simulated f_r values Δf between menisci of size Δz and a flat surface, taken at a liquid level of 0 mm, can be seen in Table 4.1, along with the associated percentage change in frequency from a flat surface at 0 mm f_0.

Table 4.1: Difference in f_r between each meniscus size Δz and a flat surface.

Δz (mm)	Δf_r (MHz)	$\Delta f_r/f_0$ (%)
0.5	8.02	0.38
1.0	16.55	0.80
1.5	23.87	1.15
2.0	31.39	1.52

This section does not provide a rigorous analysis of the phenomenon, and a more accurate model of the meniscus shape would be desirable for a variety of liquids. It does, however, present a point of consideration should the sensor find use in high accuracy applications, where errors on the order of tens of MHz become significant. It is also worth noting that the sensor used in this simulation has a length of 15 mm, and as discussed previously, smaller sensors are significantly more sensitive to small level changes in the regions around the sensor cavity. For sensor of $SL = 2.5$ mm and a liquid of $\varepsilon_r = 16$, much lower than water, the percentage change in frequency when compared with a flat surface at level = 0 mm is 1.76% for a meniscus of $\Delta z = 2$ mm. This difference is larger than any of the menisci in Table 4.1, suggesting that further study is needed to determine the impact of realistic meniscus effects for smaller sensors.

Measurement

It was not possible to create a system which accurately added liquid to the pipe *via* pressure from the bottom with the resources available. Instead, an alternative method was devised which involved carefully adding liquid from above with a syringe through a small aperture cut into the pipe, as shown in Fig. 4.12. This technique is not ideal, as small amounts of liquid cling to the inside walls of the pipe, see above the sensor in Fig. 4.12, an issue which is worsened with increasing viscosity. The total volume of liquid contained in such droplets is very small, but could become more significant for pipes of very small radii, see Fig. 4.9b. Additionally, it is unlikely that the amount of liquid added for each measurement was exact, simply as a result of human error in reading the syringe gradient. Nonetheless, this method provided a way of adding reasonably consistent volumes of liquid without removing the PTFE pipe from its frame and consequently disrupting the measurement environment between readings.

Simulations have shown that the resonant frequency of the sensor begins to decrease before the liquid level reaches the cavity as a result of fringing fields from the slot edges, sometimes in excess of 5 mm below the bottom of the sensor. Ideally, it would be sensible to begin level measurements at a point where the resonant fields are not perturbed by the LUT in any measurable way, thus providing a consistent initial resonant frequency for all level measurements to enable better comparison. However, this would necessitate a level which is at least 10 mm below the sensor, a pipe height which would take considerable time to fill if the liquid volumes of concern are small, as they are for most of the experimental work presented here. As such, the start point was defined as the bottom edge of the sensor, similarly to the 0 mm level used in previous simulations, though this point was still relatively difficult to reproduce accurately, partially as a result of the meniscus. Very small differences in liquid level are not of concern in the regions far above and below the sensor where

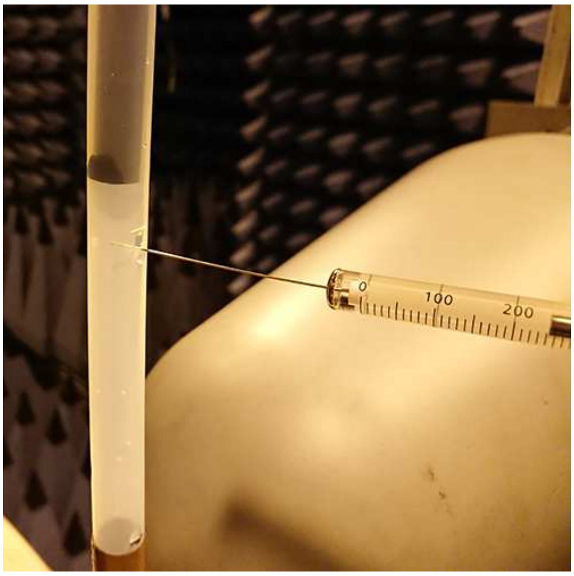

Figure 4.12: Method for adding liquid to the pipe for level measurements.

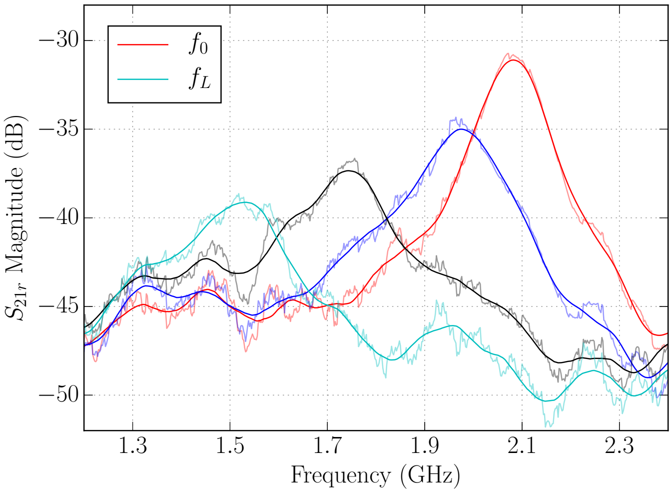

Figure 4.13: S_{21r} magnitude of four samples during a methanol level measurement.

perturbation is small. However, Fig. 4.4 shows that f_r is changing most rapidly in the lower regions of the sensor and around its bottom edge, where small changes in level will result in significant changes in f_r, as high as 200 MHz per mm in height for water. For all of the reasons stated above, the results presented here only intend to display the behaviour of the sensor in response to a rising liquid level, and are not used to correlate measured f_r values with exact levels. Despite the non-rigorous approach to level measurements, they present a strong proof-of-concept for future work, provided that results are as expected.

As shown in simulations, the level rise causes a continuous shift from f_0 to f_L, and a measured example of this can be seen in Fig. 4.13. The plot displays the measured S_{21r} magnitude at four stages during a level rise, f_0 when the methanol level is at 0 mm, f_L when the pipe is full, and two intermediate stages. It is seen that the initial resonant peak gradually shifts downwards in both frequency and amplitude until it is consistent with a standard methanol measurement. The measurements shown in Fig. 4.13 were not carried out with any particular accuracy, and are merely intended to display the sensor behaviour during a level rise. Although we refer to liquid level, it is very difficult, if not impossible without additional equipment, to accurately determine the location of the LUT within the sensor during an experiment. Instead, subsequent results will refer to the liquid volume in place of its level, as we are able to determine, approximately, the amount of LUT added per measurement using the process described in relation to Fig. 4.12. A sensor of $SL = 50$ mm was selected for all level measurements, which corresponds with a liquid volume of approximately $50\pi\left(r-d\right)^2 = 5654.9$ mm^3, or 5.65 ml.

Water was added to the pipe in 500 μL increments in Fig. 4.14a until the sensor was filled, where again the start point was defined at the bottom of the sensor, and the measured S_{21r} and associated f_r values are shown in Fig. 4.14a and Fig.4.14b, respectively. The result is as expected, and the sensor displays excellent performance, though this is largely attributable to the low-loss nature of water. Fig. 4.14a displays consistently defined peaks throughout the level experiment, allowing for accurate determination of f_r. Of particular interest is the sensitivity to very small volumes of liquid below 1 ml, where water displays a change of 200 MHz over this range as seen in Fig.4.14b. This region also has the advantage of low losses, where the pipe is still mostly filled with air, reducing the impact of high-loss LUTs on identifying resonant peaks. While it is possible to measure butanol and ethanol with a single sensor, Figs. 3.35 and 3.36 showed that these responses feature a large amount of noise, making these liquids, as well as other lossy LUTs, good candidates for multiple sensors as discussed in section 3.7. The relatively low SNRs resulted in somewhat erratic level measurements once enough liquid had filled the sensor, but remained acceptable below this level.

To exploit the rapid change in f_r and low-loss environment encountered when liquid levels are low inside of the sensor cavity, each liquid was added to the pipe in 50 μL increments, corresponding with approximately a 445 μm level rise. The experiment was stopped after the addition of 1000 μL due to the amount of time taken, though this volume is enough to display the behaviour of the sensor to a good degree of resolution. Fig. 4.15 shows the result for each liquid, and Fig. 4.16 compares the measurements in one plot. The initial measured resonant frequency is slightly different for each liquid due to the uncertainty in determining a 0 mm level,

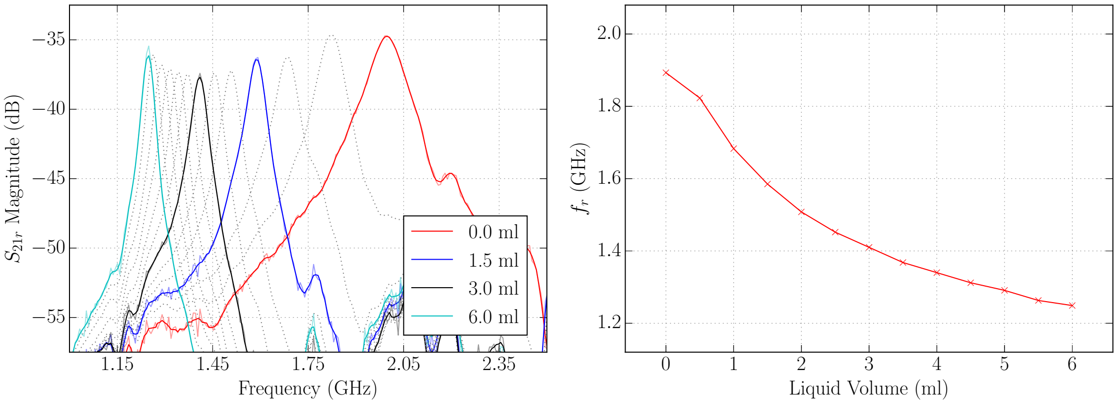

(a) S_{21r} (b) f_r

Figure 4.14: Measured S_{21r} and associated f_r values during a water level measurement up to 6 ml.

as discussed previously. We see that the change in f_r is reasonably linear with respect to level, or volume, over this region, with the exception of methanol and water at 600 - 700 and 750 - 800 μL, respectively. These points may be explained by incorrect addition of liquid, where a volume greater than 50 μL was added accidentally, as both appear to recover linearity following a more rapid decrease in f_r. It should be noted that these results cannot be compared directly, where the liquid volume is an approximation subject to human and systematic error, resultant from misreading of the syringe gradient or the 0 mm starting point and the effect of liquid adhering to the inner pipe walls. They do, however, display the expected behaviour and suitability of the sensor to perform highly-sensitive liquid level measurements, provided that LUTs are of a reasonably low-loss for measurements over the full range. High-loss liquids may still be measured, as displayed here, but potentially only for the lower regions of the sensor cavity.

4.1.2 Multiple Sensor

Using a single sensor for measurements allows for a continuous gradient of liquid level, limited only by the accuracy of the system. The previous section also showed that such measurements may also be impacted by the high levels of loss encountered in some liquids, such as butanol and ethanol. Section 3.7 presented the possibility of using multiple sensors to increase the SNR of measurements, particularly for lossy liquids, and this configuration may also be utilised to realise an alternative level sensing method based on amplitude rather than resonant frequency. Consider a number of sensors, of the same dimensions, positioned on an empty pipe and positioned equidistant from each other. With no liquid present and for a large enough separation,

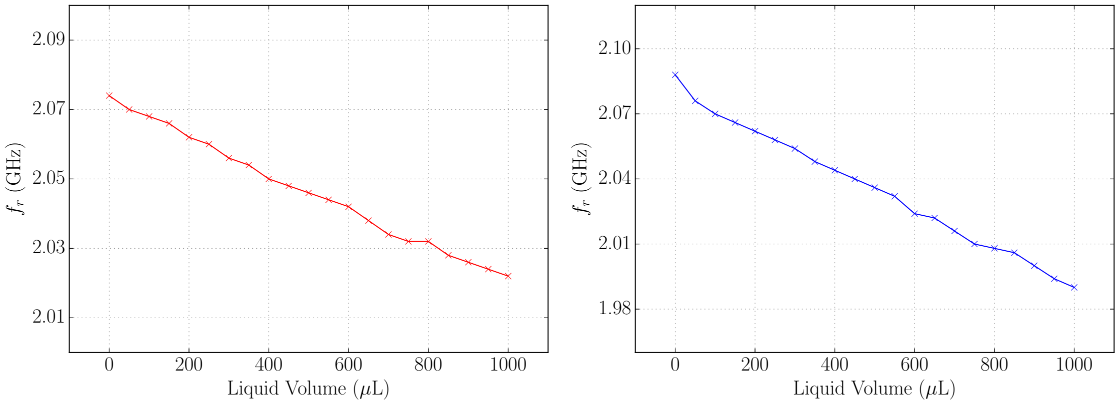

(a) Butanol (b) Ethanol

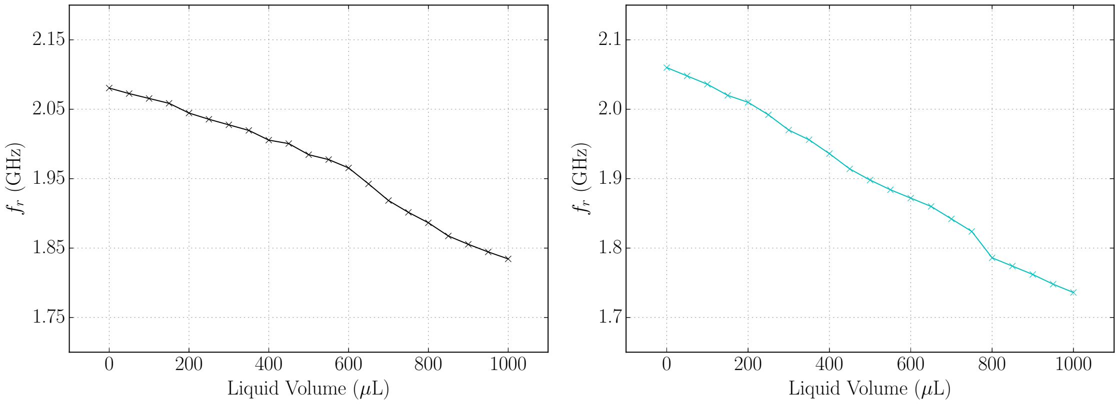

(c) Methanol (d) Water

Figure 4.15: Level measurements for each liquid for a total volume addition of 1000 μL.

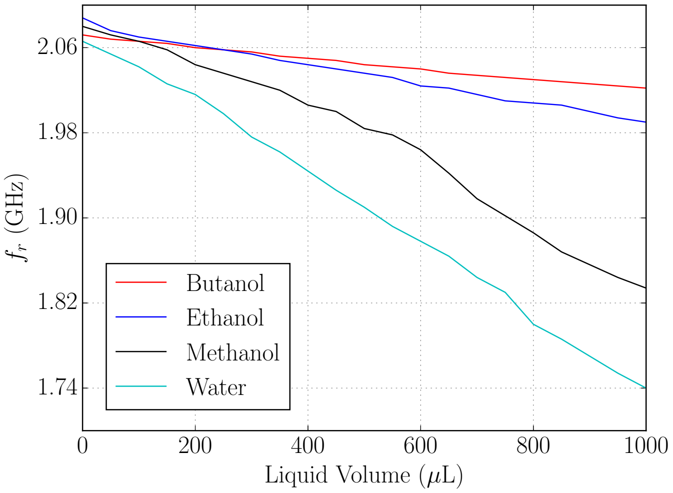

Figure 4.16: Level measurements for each liquid, up to 1000 μL.

each individual sensor resonates independently and acts to improve the SNR of a measurement which will respond with a resonant frequency associated with an air-filled pipe, f_0. As the liquid level rises, it will reach, and eventually fill, the sensor in the lowest position on the pipe, which will begin to resonate at the frequency corresponding to the liquid present, f_L. This will simultaneously decrease the S_{21r} amplitude observed at f_0 and increase it at f_L, an effect which is compounded as each successive sensor is reached by the LUT. Fig. 4.17 shows a five sensor configuration, where the arrows denote possible measurement sample intervals as the liquid level rises. When the liquid level is at a point within one of the sensors, the resonance of that individual sensor will change in accordance with the behaviour of a single sensor discussed in the previous section, where a continuous decrease in f_r will occur as level rises. At the sampling points indicated in Fig. 4.17, each sensor will resonate at either f_0 or f_L, resulting in peaks in the S_{21r} response at both frequencies, with the exception of points 0 and 5 which will only display a single peak at f_0 and f_L, respectively. By filling the pipe to each sample point and recording the measured amplitudes at either f_0 or f_L, or both, it is possible to determine at which point the level is currently positioned. This method essentially discretises the level range into the number of sensors in place, where resolution may be increased by using a greater number of smaller sensors with a lower SL, therefore increasing the amount of sampling points. Of course, it would be possible to detect a level which is between sampling points *via* peak-detection, though this would defeat the object of measuring liquid level by amplitude. For example, if the liquid was at a position between points 2 and 3 in Fig. 4.17, three peaks would be observed: f_0 corresponding with the top two air-filled sensors, f_L resultant from the bottom two liquid-filled sensors, and a third at a frequency between f_0 and f_L which can be used to determine the current level within the middle sensor. Using the amplitudes at f_0 and f_L, which provide information on the number of completely filled and unfilled sensors, along with the partially-filled sensor resonance, it is possible to approximate the liquid level. It is worth noting that this method relies on suitable frequency separation of f_0 and f_L, therefore allowing for the identification of resonances resultant from partially-filled sensors. Fig. 3.50 displayed a simultaneous measurement of water, butanol and air-filled sensors, which would be similar in form to the example scenario described, where the butanol peak represents the partially-filled sensor.

To display the multiple sensor level detection method, a sensor configuration of 5 × $SL = 25$ mm was used, as shown in Fig. 4.17. After an initial measurement with an air-filled pipe (sample 0), water was added to the next point above the adjacent

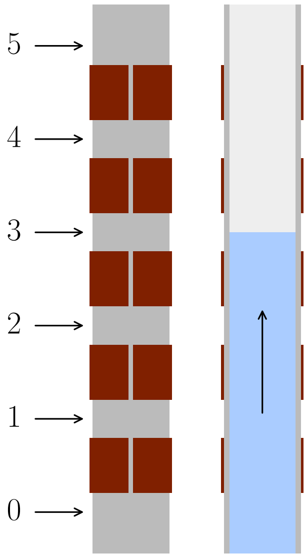

Figure 4.17: Diagram of the multiple sensor configuration used in Figs. 4.18a and 4.18b.

sensor and a sample taken (1), this was repeated until all five sensors were below the water level (5). The measured S_{21r} responses at sample 0 and 5 are shown in Fig. 4.18a, along with the intermediate results displayed by the dotted curves. The broadness of the peak at sample 0 is explained by the presence of multiple resonances in close proximity, perhaps resultant from incorrect positioning or issues relating to fabrication errors as discussed in section 3.2. It is also clear that the resonance around f_L gradually decreases in frequency as each sensor is filled, this is similar to coupling behaviour analysed in section 3.7.1 which suggests that the sensors were placed too closely to one another. From the curve profiles two suitable frequencies were selected for analysis, where $f_0 = 2.04$ and $f_L = 1.27$ GHz, and the measured S_{21r} amplitudes at these points are plotted in Fig. 4.18b. We see the expected result, where the amplitude at f_0 decreases as the water level rises, and *vice versa*. The amplitudes are displayed as discrete data points due to the non-linear behaviour between samples, where the amplitude at f_0 will decrease very rapidly as water approaches and enters a sensor, and a similar abruptness would be expected at f_L when water reaches the top of a sensor cavity. Although no measurements of the alcohols were undertaken, the amplitude rise observed at f_L would be very similar to the results presented in Fig. 3.46, which displayed the peak amplitude increase as additional sensors were added to the pipe.

Though not necessarily advantageous, it is trivial to make use of sensors of varying slot width within the multiple sensor level sensing method. The initial measurement would instead feature multiple resonant peaks, corresponding to each SW present,

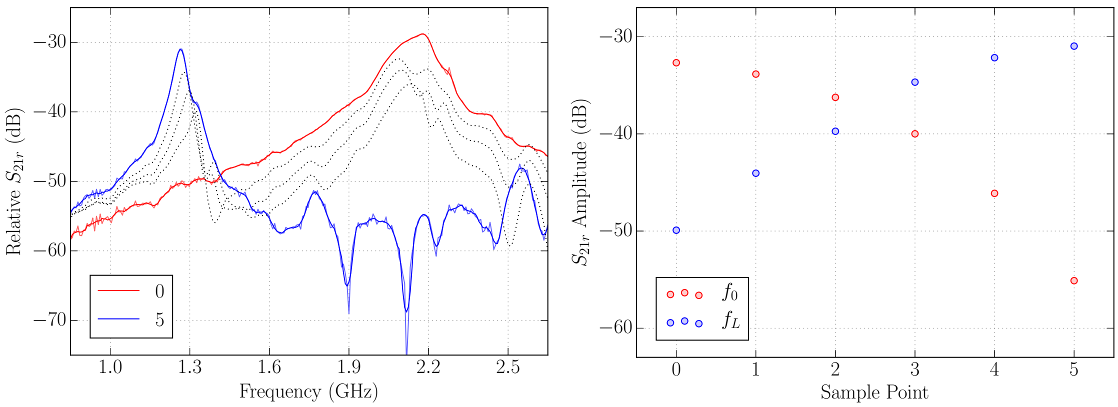

(a) S_{21r} at sample 0 and 5.

(b) Amplitude at f_0 and f_L.

Figure 4.18: Measured S_{21r} at sample points 0 and 5 and amplitudes at f_0 and f_L for each sample.

where each peak would move to f_L individually as the associated sensor is filled. This method could provide some defence against an electrically noisy environment, where the amplitude of S_{21r} measurements may be adversely affected. A multiple sensor level sensing system using one slot width for all sensors results in two single points of reference for f_0 and f_L, both of which may increase or decrease in amplitude as a result of the environment and potentially provide inaccurate level measurements. Using different slot widths, and therefore different f_r values, each discrete rise in level instead corresponds with a specific resonant peak. This method was assessed using three sensors of $SL = 50$ mm and slot widths of 0.5, 1 and 1.5 mm, where water was added to the pipe until it reached the base of the lowest sensor, $SW = 1.5$ mm. Water was added in roughly 500 μL increments, covering a total height range of 180 mm ($\approx$ 20 ml) consisting of 3 × 50 mm sensors and two gaps of 15 mm. The first and final measurements are compared in Fig. 4.19, where the initial measurement shows three distinct peaks corresponding with the three sensors. The points a), b) and c) are situated at 2.509, 2.243 and 2.012 GHz, respectively, and the frequency at w) is 1.249 GHz. The final measurement displays only a single resonance corresponding with water-filled sensors, where the peak is seen to be broader than similar water measurements in this thesis, resultant from the differing resonant frequencies of each SW.

The amplitude at each frequency sample was taken after every level rise, and these results are shown in Fig. 4.20. Here we see the naturally noisy nature of the measurements, where the amplitudes tend to fluctuate due to the level rise, although the trends are still very clear. The experiment begins with the water level at the base of the lowest sensor, $SW = 1.5$, and the corresponding resonant peak, a), experiences

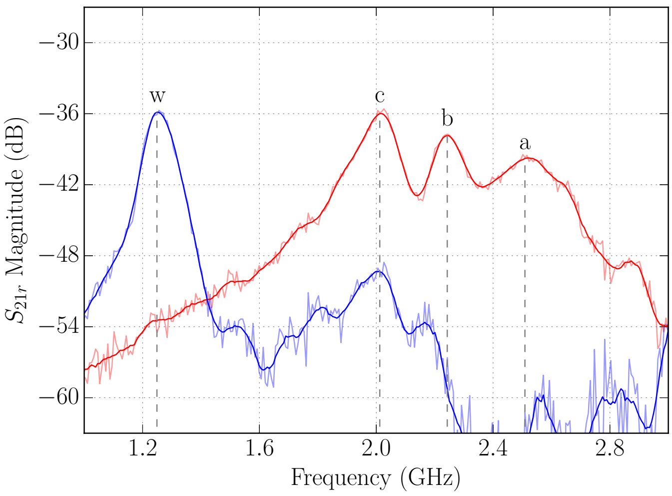

Figure 4.19: S_{21r} magnitude of the first (red) and final sample (blue) taken during the experiment.

a steep decline in amplitude immediately as water is added. Water reaches the second sensor, $SW = 1.0$, at around sample 12, where the amplitude at b) behaves identically, and following this the same happens for the resonance c) associated with the topmost sensor, $SW = 0.5$. Throughout the measurement we see a consistent rise in the amplitude measured at w), as the S_{21r} peaks a), b) and c) move to lower frequencies, before individual sensors become filled. The continuous rise in amplitude observed at w) is slightly unexpected, as it would have been perhaps more intuitive for the increase to occur only as the water level reaches the top edge of a sensor, thus moving that sensor's resonant frequency close to w) and contributing to the measured amplitude at this point. From analysis of the intermediate S_{21r} responses, not shown here, it is seen that the non-resonant regions contribute to amplitude increases at w) in a useful manner. One can imagine, for example, the profile of the initial measurement in Fig. 4.19 being transposed to the left, where the amplitude measured at w) would begin to rise immediately, long before the peak at c arrives. The amplitudes at a), b) and c) display a rapid change almost immediately after water reaches the associated sensor, allowing for the determination of level from a threshold amplitude. The threshold in this measurement could be set in the range of -43 to -48 dB, separating the amplitudes associated with filled and currently filling sensors from those of sensors which have not yet been reached by the liquid level. For example, if the amplitude at c) is above the threshold while a) and b) are below, as is the case at sample 20, an appropriate system can determine that the water level is very near to or above the base of the middle sensor, and not yet at the top sensor. Additionally, assessment of these amplitudes may be cross-referenced with

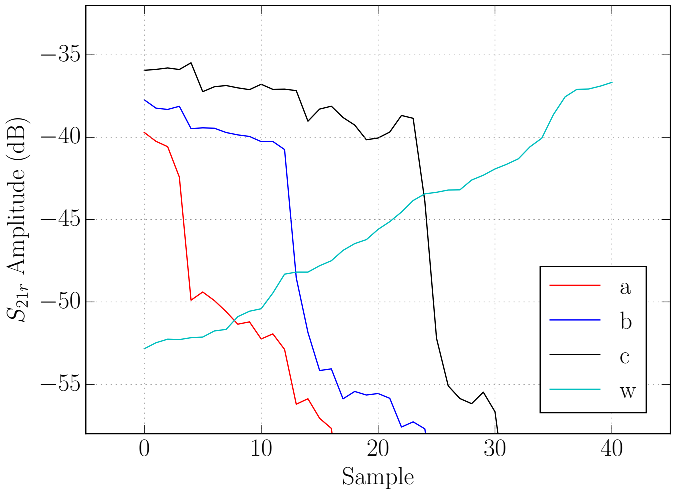

Figure 4.20: S_{21r} amplitudes of each frequency sample during the experiment.

w) to estimate a more accurate position, if required.

The configuration for this measurement could have been improved by reversing the sensor order, with the sensors operating at a higher frequency placed above those of a lower frequency. This would ensure that the the lowest frequency peaks move first and do not disrupt the amplitudes of other peaks associated with empty sensors as significantly. As water fills the $SW = 1.5$ mm sensor, the resonance a) in Fig. 4.19 will display a continuous decrease in frequency, see Fig. 4.16, which will superpose with resonances b) and c) as the peak moves to a lower frequencies, potentially distorting the measured amplitudes. However, the use of a threshold amplitude would not be affected by such an issue, which would be set appropriately depending on a given sensor configuration, certainly not at an amplitude susceptible to such errors.

Using sensors of different resonant frequencies requires the monitoring of additional frequency samples, something which is a disadvantage when compared with the configuration shown in Fig. 4.18a, which requires a maximum of two samples. However, using a number of slot widths increases the total amplitude change ΔA for each discrete rise in liquid level, due to the independent nature of each sensor. The lowest ΔA in Fig. 4.18a was 1.17 and 1.19 dB for the air and water sample, respectively, which could easily provide a source of error given a sufficiently noisy measurement environment. Additionally, any frequency-dependent noise which exists at frequencies close to the sample(s) chosen in Fig. 4.18a could cause interference, whereas the use of multiple frequency samples in Fig. 4.20 provide some protection against this, especially should a larger number of sensors be used. For example, if we presume the presence of destructive interference at c) which causes its amplitude to drop below a given threshold, samples a) and b) may be cross-referenced and used to determine whether the decrease is valid. There exists a number of possible configurations for level detection, including a single sensor, multiple devices of the same resonant frequency and multiple sensors resonant at independent frequencies. Each has its advantages and disadvantages, but again shows the sensor geometry to be adaptive and capable of meeting a wide range of requirements.

4.2 Temperature Sensing

The sensor geometry has shown to be highly sensitive to small variations in permittivity, and can be made more sensitive through appropriate design, such as a larger slot width (Fig. 2.34) or smaller wall width (Fig. 2.48). This sensitivity can be exploited to measure changes in the permittivity of the LUT caused by temperature variations, where a measurable difference will require a liquid for which ε_r is suitably temperature dependent. Simulations of temperature-based measurements will not be necessary, as they essentially repeat any results which studied the effect of ε_r on resonant frequency.

The alcohols used in this thesis were discussed in section 3.1, initially using models proposed by [60]. Fig. 3.1 shows the real part of the permittivity against frequency for each alcohol, modelled from 10 to 40°C . Ethanol and butanol both show good temperature dependency, which decreases with higher frequencies but is suitable below 3 GHz. The permittivity of methanol presents a more complicated scenario, where its behaviour in relation to temperature only becomes clearer above 2 GHz. This is unfortunate for two reasons, the first being that methanol has a relatively low loss tangent $\tan\delta$ in comparison with butanol and ethanol below 2 GHz, resulting in a greater SNR as displayed by Fig. 3.36. The second issue is that the PTFE pipes made available for all experimental work had a fixed radius, where $r = 7$ mm. Coupled with restrictions placed on the SW and SL dimensions related to performance considerations, all methanol measurements were below 2 GHz, usually around 1.45 GHz. It is in this frequency range that methanol has a more complicated relationship with temperature. Using the models in [60] for a temperature range of 10 to 40°C , a number of frequency samples were extracted and plotted against temperature in 5°C increments. Fig. 4.21 shows the result for each alcohol, where samples were taken at 1, 1.5 and 2 GHz, as well as a further frequency sample selected as the measured f_r for each liquid in a 5×25 mm configuration, see Fig. 3.46. Butanol and ethanol both display an increase in ε_r with temperature for

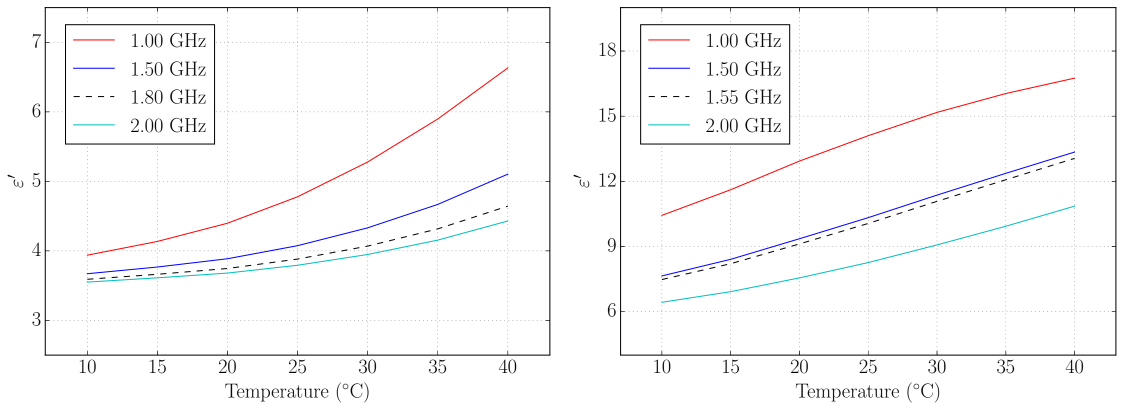

(a) Butanol (b) Ethanol

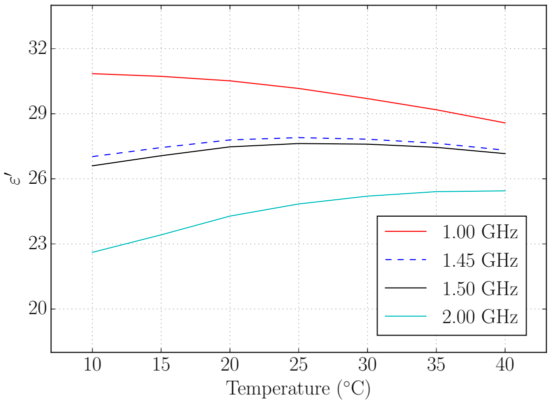

(c) Methanol

Figure 4.21: Real part of the permittivity for each alcohol against temperature at discrete frequency samples.

every frequency sample, where butanol shows a sharper rise as temperature increases and ethanol is relatively linear. Methanol presents more complicated behaviour, as discussed previously. The 1 GHz sample shows ε_r decreasing with a temperature increase, while at 2 GHz we see the opposite scenario, where both display a non-linear relationship. However, for the 1.45 and 1.5 GHz frequency samples, ε_r rises with temperature up to 25°C and then begins to decrease with further temperature increases. The results in Fig. 4.21 rely on [60] and measured results were not possible with the resources available, but would be a valuable resource for temperature sensing measurements.

The laboratory environment available did not allow for the heating of volatile alcohols, as the purchase of necessary equipment would have been costly and would not find a great deal of use outside of the measurements presented here. As such, temperature measurements rely on cooling the alcohols and allowing them to rise in temperature over a period of time. Additionally, accurate measurement of the liquid temperature was not easily achievable without disrupting the experimental

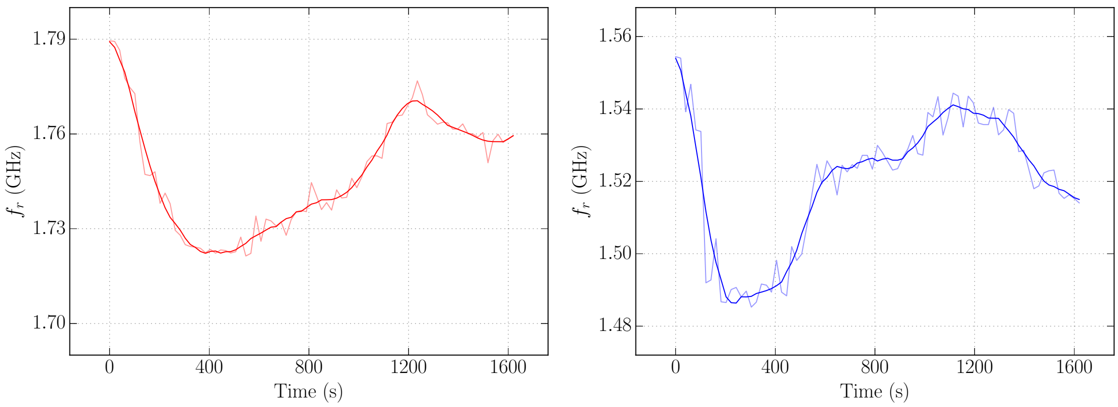

(a) Butanol (b) Ethanol

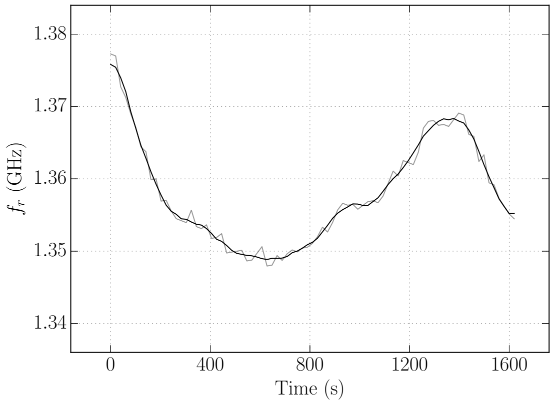

(c) Methanol

Figure 4.22: Measured f_r against elapsed time, where the liquid temperature is rising.

setup significantly between each reading. For this reason, results will be presented in terms of elapsed time rather than temperature, effectively showing the change in temperature over a certain region. This method, while not able to accurately determine f_r for a given temperature, provides a proof-of-concept for further temperature measurement methods based on the sensor geometry.

Three flasks of butanol, ethanol and methanol were placed into a freezer overnight for around 12 hours, where the melting point of each alcohol is on the order of -100°C ensuring that they do not freeze. Unfortunately, the freezer available was situated a short walk away from the anechoic chamber, requiring that the flasks be placed into a polystyrene thermal container to reduce heat rise during transit. Each flask was removed and transported individually, immediately added to the pipe and measured as quickly as was practically possible. From this point, a measurement was taken every 20 seconds for just under 27 minutes, or 81 samples. The calculated resonant frequency from each sample was extracted and the results can be seen in Fig. 4.22 for each alcohol.

The plots certainly display some interesting behaviour, where up to around 400 seconds the alcohols behave as expected, gradually increasing in temperature and permittivity, resulting in a decrease in f_r. However, after this point there is a large rise in the resonant frequency before once again decreasing, and it is not immediately clear why this occurs. One possible explanation is that the liquids are heating in a non-uniform manner, resulting in variations in temperature throughout the sensor. As the LUT is added to the pipe, outer regions may quickly cool the PTFE pipe walls and rise in temperature, while inner regions remain at a lower temperature. At this point the liquid near to the slot will have an increased ε_r thus the initial decrease in f_r shown in Fig. 4.22. The inner regions of the LUT may then begin to heat up, resulting in the outer regions lowering in temperature and therefore permittivity, causing a rise in the resonant frequency. As the outer regions warm for a second time f_r decreases once more, presumably settling at a constant value after sufficient time has elapsed, though unfortunately there is no experimental data beyond the time shown here. PTFE has a high thermal conductivity of around 0.25 W/mK, which is higher than each of the alcohols, potentially helping to explain the apparent oscillation of temperature between the PTFE and LUT suggested by Fig. 4.22. It is important to remember that the resonant electric field does not penetrate a great distance into the LUT, where Fig. 2.45 displayed the normalised field strength looking downward from the slot for a range of permittivities. A temperature variance within even the first couple of millimetres in the slotted region could have a significant and measurable impact on f_r. In order to compare the behaviour of each alcohol, the measured f_r was normalised against the initial frequency f_0 for each liquid and plotted in Fig. 4.23. It is interesting to note that permittivity does not vary as greatly with temperature for methanol as it does for butanol and ethanol, and this alcohol appropriately appears to oscillate much less during the experiment. Additionally, it should be mentioned that there is also the consideration of the vertical temperature distribution, where the liquid will be slightly warmer towards the top of the sensor that at its bottom edge, resulting in a permittivity differential along the length of the slot which will vary throughout the measured time period.

Freezing liquids and measuring the rise in temperature was feasible for each alcohol due to their low melting point, but this was not possible for water. Instead, a volume of distilled water was heated, transported to the lab and measured using the same temperature measurement sampling method. The experiment result is displayed in Fig. 4.24, where the measurement duration was unfortunately limited to ten minutes. The measured f_r shows a downward trend with elapsed time, and therefore

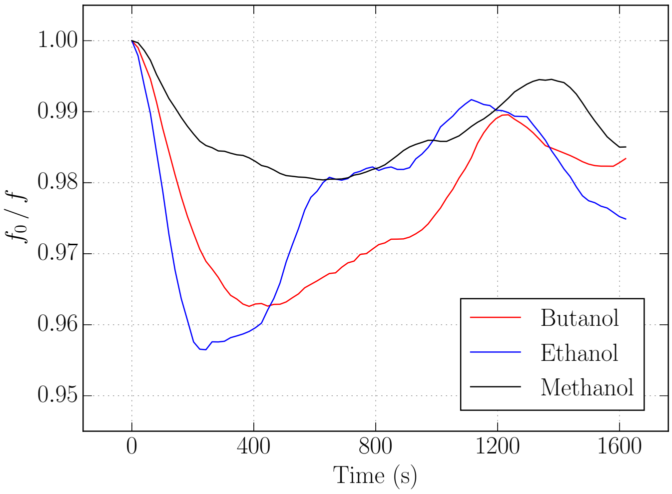

Figure 4.23: Comparison of results in Fig. 4.22, normalised against initial frequency f_0.

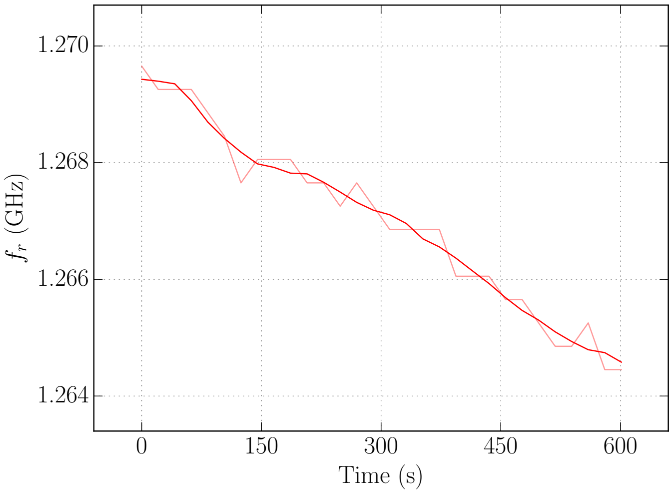

Figure 4.24: Measured f_r of water against elapsed time, where the liquid temperature is falling.

also with decreasing temperature, as the water was cooling to room temperature during the experiment, rather than rising as with the alcohols in Fig. 4.22. The permittivity of water is well-understood to decrease with increasing temperature, and this would agree with the change in resonant frequency displayed by Fig 4.24. The water was heated by a dispenser set to 70°C and added to an open beaker, then poured into the pipe within 60 seconds. During this process the water may have cooled significantly, where Fig 4.24 potentially shows only a very small temperature differential. Nonetheless, there is a definite trend and further measurements would be useful in determining the capability of the sensor in accurately determining water temperature given its low loss tangent and therefore improved SNR.

4.3 Conclusion

This chapter looked at potential applications of the split-cylinder geometry other than the monitoring and detection of liquid permittivities. Simulations have shown that as liquid level rises within the sensor cavity, the sensor responds as if an equivalent homogeneous medium is increasing in permittivity, allowing for the determination of level if the LUT is known. The geometry was shown to be highly sensitive to relatively small changes in level, where sensors of a smaller SL increase this sensitivity further. Additionally, the resonant frequency of smaller sensors is impacted considerably by level changes within the fringing field region, above and below the device. This may present a method to measure high-loss liquids without reducing Q too greatly, as the sensor cavity remains completely or mostly air-filled. The effect of changes within the fringing field regions is further displayed by a study of a spherical cap meniscus of varying size. The meniscus was shown to have a small but relevant effect, and becomes much more significant when SL decreases. A water measurement displayed sensor behaviour as the device was completely filled, and further measurements exploited the high sensitivities observed as liquid enters the sensor cavity. Each LUT was measured using a small volume (1 ml) of liquid, showing a consistent decrease in f_r with rising level. The method of using multiple sensors is revisited to detect discrete changes in level by monitoring amplitudes at appropriately selected frequency samples. As the liquid level rises the number of liquid-filled sensors increases, and amplitudes at frequencies associated with empty and full sensors decrease and increase, respectively. This method seeks to remove the requirement of frequency domain analysis, though assessment of the S_{21r} response would also determine the liquid level between sampling points. An adaptation of this method uses multiple sensors of different SW to provide a number of frequency samples. This technique provides a much greater drop in amplitude as liquid enters each sensor due to the independent nature of the resonances associated with each device, as well as increased resistance to noise and interference. This chapter also introduced the potential of performing temperature measurements with the split-cylinder geometry, although the experimental equipment was not sufficient to adequately perform such measurements. The unexpected results were possibly resultant from time-variant, non-uniform thermal distributions within the LUTs. The sensor did, however, at least display sensitivity to small changes in temperature, further exemplified by a measurement of cooling water. This chapter has shown that the sensor geometry may be applied to a number of different problems other than simple detection of permittivity. Various level sensing methods have been introduced, each with their own particular advantages for different applications.

Chapter 5

Conclusion & Future Work

This thesis has introduced a novel method for the wireless measurement of liquids within pipes using a slotted cylindrical resonator. The geometry allows for simple integration with existing, non-metal pipework used to transport or store liquids, resulting in minimal disruption to live processes. Additionally, the *in situ* nature of the sensor removes the requirement for samples, providing a non-contact method for the wireless assessment of liquids which may be hazardous or otherwise harmful. The sensor geometry is highly adaptable, where a number of parameters may be adjusted to suit a particular application, such as tuning the resonant frequency or configuring sensitivity. A comprehensive analysis of the device has been presented through theory, simulation and measurement, covering a wide range of relevant aspects of performance including sensitivity analyses and effects of the measurement environment. The sensor has been shown to be capable of measuring a relatively large range of permittivities as well as liquids of high loss, where the latter is made possible by the simple placement of additional sensors. Further applications were studied, where the device is highly sensitive to small changes in liquid level, and has shown to be capable of detecting temperature changes for liquids that display suitably temperature-dependent permittivities.

The proposed sensor presents a less-common approach to liquid measurements, as sensing occurs ‘on-pipe’ without the need for any external circuitry or support, other than a pair of antennas. The majority of the microwave or millimetre-wave sensors in the literature require that samples be taken and carefully added to a precise point within a resonant structure, or operate with the use of a microfluidic channel. Many of these sensors perform well and some are capable of accurately measuring permittivity, complex or either part, but do not always offer distinct advantages over established methods of liquid permittivity measurements, such as the open-ended coaxial probe discussed in section 1.4. It has been mentioned that the liquid measurement technique used in this thesis is not intended for high-accuracy applications, but instead seeks to present a simple method for the wireless detection of known liquids. That is not to say that there is not the possibility of more accurate characterisation in future work, where the calibration curve shown in Fig. 3.37 used simulated data to estimate the permittivity of measured liquids. Unfortunately, the fabrication method produced sensors which were not easily modelled in simulation software, as discussed in section 3.2, resulting in differences between measurement and simulation. A consistently reproducible geometry that agrees well with simulated data could certainly estimate ε_r using calibration curves, generated either from simulations or measurements of reference liquids.

When compared with sensors in the literature with similar applications, particularly devices which perform non-contact sensing using microfluidic channels, this work offers a number of advantages which make the split cylinder geometry a viable option for the real-time monitoring of liquids. The structure is incredibly low-cost as fabricated in this thesis, and it is not expected that improved fabrication techniques will result in an expensive device, due to the lack of active circuitry or high-performance substrate. Additionally, wireless excitation techniques remove the need for any cabling to the sensor, which greatly simplifies scenarios in which many liquids are being monitored simultaneously, as would presumably be the case in an industrial setting. The sensor is readily incorporated into such an environment, provided of course that there is appropriate spatial separation of the devices, where the simultaneous measurement of three sensors shown in Fig. 3.50 required only 5 cm between pipes. The ability to incorporate a number of sensors into a single measurement system, using the same antennas, is aided greatly by the sensitivity of the structure, which enables the separation of various monitoring processes in the frequency domain. Fig. 3.49 displays an example of how different sensor geometry and configurations can be used to optimise the measured response and improve peak detection when monitoring multiple liquids or devices. The comparatively high sensitivity of the sensor is made possible as a result of the significant perturbation of the excited electric field by the liquid cavity, as shown in Fig. 2.11 for a range of ε_r. This sensitivity may be increased further through the use of a thinner pipe wall, Figs. 2.47 and 2.48, or to a lesser extent by selecting a larger slot width, Figs. 2.33 and 2.34. In cases where it is desirable to reduce sensitivity in an effort to decrease the bandwidth necessary to measure a given range of permittivities, the opposite is true, where an example of this is shown in Fig. 2.49. The adaptability of the sensor is further displayed in section 3.7, which showed that the use of multiple sensors significantly improves the measured response. This result is of particular importance to measurements involving lossy liquids, which greatly degrade the performance of the sensor, as shown by the effect of LUT loss tangent on the simulated S_{11} in Fig. 3.12. By simple addition of multiple sensors this effect is mitigated, and the total number in place may be increased indefinitely until limited either by availability of space or effectiveness in improving the response, where the latter may be a function of the antenna read distance.

One objective of this work, discussed in section 1.5, stated that the sensor should be resilient to a practical measurement environment, given its intended application in an industrial setting. Section 3.3 considered four potential sources of poor performance or error, relating to the relative position or rotation of the antennas and sensor. The antenna read distance d was studied in section 3.3.2, where Fig. 3.18 showed that increasing d had the obvious impact of reducing the S_{21r} magnitude across the entire frequency range, but also decreased the SNR, seen by the noise level in the raw measurement data for $d = 80$ cm. However, the increase in noise appears most significant away from resonance, and the profile of the response does not worsen to any great extent. This suggests that, at least for low-loss liquids, the antenna read distance does not need to be very small for acceptable performance, where the total distance between antennas was generally 100 cm throughout this thesis. The rotational position of the sensor was shown to be non-critical in section 3.3.3, where the peak amplitude varied by approximately 3.5 dB and a relatively small variance in f_r was observed, though this was more likely a result of deformation of the Mylar film during rotations. Vertical positioning of the sensor was also assessed, where section 3.3.4 presented measured data of a water measurement as the device was moved away from LoS, showing reduced but still acceptable performance. Finally, the effect of changes in the polarisation of the transmitting antenna on the sensor response was studied in section 3.3.5 for an air and water measurement, see Fig. 3.24. In both cases, the measured resonant frequency did not deviate by a great deal until the antenna was rotated through almost 45°, and even up to this point for the water-filled pipe. Through a study on the impact of various practical issues on performance, the sensor displays relatively good resilience to changes in the measurement environment, a feature which is essential for applications in industry.

Chapter 4 moved beyond the simple measurement of liquid permittivity to assess other potential applications of the sensor geometry. It was shown through simulation that a rising liquid level within the sensor cavity causes a continuous decrease in the resonant frequency, proportional to the LUT ε_r, as seen in Fig. 4.4. Measurements of each liquid displayed very high levels of sensitivity to relatively small changes in level, shown in Figs. 4.15 and 4.16. The noise inherent in measurements of lossy liquids using single sensors presented a problem for the accuracy of level sensing over the full length of SL. The measured f_r tended to deviate slightly during measurements for butanol and ethanol, resulting in potential errors in determining the liquid level, although the trend remained valid. Such deviation was not observed for the measurements in Fig. 4.15 as a result of the sensor cavity containing mostly air, thus retaining a low loss tangent. Therefore, the level sensing of very lossy liquids may still be achieved with a single sensor by simply reducing the total range of consideration to the lower portion of the sensor, and extending to areas below. Indeed, a study of the sensitivity to liquid level within the fringing field region above and below the sensor concluded that a smaller SL can significantly increase the change in f_r per unit change in liquid height, as shown in Fig. 4.7. The sensitivity as liquid approaches the bottom edge of the sensor is emphasised in a study on the effect of a spherical cap meniscus of varying size. Though small, there is a definite change in simulated f_r in Fig. 4.11, and much more considerable change when using a smaller SL as a result of increased level sensitivity. An alternative method for discrete level sensing is realised by using a number of sensors, and observing the response amplitude at appropriate frequency samples, where a water measurement is shown in Fig. 4.18. A variation on this method uses sensors of different SW to associate a given liquid level with a drop in amplitude at a specific frequency sample, as discussed in relation to Figs. 4.19 and 4.20. This technique offers advantages over using the same SW related to resistance to errors caused by noise or interference, where multiple frequency samples may be cross-referenced to determine liquid level. The slotted cylindrical geometry presents a number of ways to sense level, each suitable for different applications, again displaying the adaptive nature of the sensor. An attempt was made to detect small changes in temperature in section 4.2, although the method used to induce the temperature differential was less than ideal. The measured f_r against elapsed time for each alcohol was shown in Fig. 4.22 and compared directly in 4.23. Unfortunately, the results exhibited some complicated behaviour which may be explained through time-variant, non-uniform temperature distributions within the liquid cavity. The results, in combination with Fig. 4.24, still show that the sensitivity of the sensor is adequate to respond to what are relatively small changes in permittivity, and the sensing of temperature remains a potential application.

The sensor geometry introduced and analysed in this thesis intended to satisfy a number of aims and objectives which were defined in response to a study of the relevant literature and work on liquid sensors, as well as in relation to the application of real-time, *in situ* monitoring of known liquids within non-metal pipes. This work has developed a sensor which is passive, excited wirelessly and conformal to the cylindrical geometry of pipes, requiring no additional circuitry, cabling or support for on-pipe placement. The sensor has been shown to be generally resistant to changes in the measurement environment, at least within the experimental configuration used in this thesis. Some measurements have lacked the desired consistency, though a large portion of this issue is considered to be a result of the simple fabrication techniques used, where it is not envisioned that a soldered thin-film would be used in practice. Aside from offering on-pipe measurement, the adaptive nature of the geometry is perhaps the most attractive feature of the sensor when compared with much of the literature. Assuming that the pipe dimensions and material are fixed for a given industrial process, the slot width and length still offer a method by which the resonant frequency of the sensor may be tuned as desired. If it is possible to adjust the pipe itself, then there exist further degrees of freedom with which the sensor behaviour and performance may be controlled. Aside from individual sensor geometric considerations, the combination of multiple devices provides an additional avenue of optimisation for a particular placement or application, where even the distance between sensors may be used to tune frequency. The slotted cylindrical resonator has largely achieved the specified aims and objectives of this thesis, and represents a viable option for the general-purpose sensing of liquids, along with a number of potential future applications.

5.1 Future Work

Incorporation of the sensor into a practical measurement system is ultimately the desired outcome of this work, and would require that a number of issues be resolved. Fabrication represents an area which would be central to future study, where inconsistencies between sensors, or even measurements of the same sensor, has been a problem throughout the presentation of measured data. The accurate reproduction of devices would be beneficial not only to measurement accuracy and precision, but also to the usefulness of simulations. By fabricating a sensor of more exact dimensions, we may create a simulated model which represents the physical device much more closely, enabling the generation of more useful data such as calibration curves. Additionally, forming the device as solid metal removes uncertainties associated with thin-films, including relatively poor structural integrity. A slot of approximately 2 mm was cut into a solid brass pipe of a radius slightly smaller than the experimental PTFE pipes, and from a very brief assessment the structure appeared to resonate very well, though unfortunately no measurement data is available. Once a consistently reproducible sensor is realised, there is the issue of reliance on relative measurements to consider. The work carried out in this thesis has shown various aspects of the behaviour and performance of the sensor through the use of S_{21r} measurements, which essentially exaggerate the effect of the resonator for the purposes of identifying resonant frequencies, amplitudes, and other aspects of the response. The same method may be possible in practice but would require a relatively static environment, possibly achieved by routing pipework through a controlled environment containing the sensor(s) and antennas, or alternatively, and less desirably, by taking reference readings periodically. However, the use of a higher gain antenna designed specifically for the range of expected f_r in combination with a circulator could represent a significant improvement in performance, potentially capable of directly measuring the backscattering from the sensor(s). Removing the use of relative measurements may also improve the general response profile by reducing noise associated with non-resonant differences between the current and reference reading, which can be emphasised in S_{21r} responses. There also exists the prospect of exciting the sensor *via* probes and measuring the radiated signal, or even the possibility of removing the wireless aspect completely. These solutions are not particularly attractive, as they remove a key advantage of the measurement method, as well as moving the sensor into a different category of liquid sensor in which it may not offer any advantages over established methods. However, if the geometry were to work very well when supplied with power it would still retain many of the advantages related to adaptability, as well as on-pipe operation, certainly warranting future study into active configurations.

The work undertaken on level sensing has provided a good proof-of-concept foundation which should be developed. The sensor is capable of detecting liquid level in a number of ways, and each of these methods presents a number of potential points of consideration and analysis for future research. An issue that proved problematic during level experiments was that of accurately determining the liquid level in terms of a vertical position within the pipe. It is possible to estimate this position to a good degree of accuracy through simple calculation if the liquid volume is known and the inner pipe radius is consistent. Using a small syringe allowed the general behaviour to be displayed, but is not sufficient for more accurate determination of liquid level. The level sensing method would benefit greatly from a system which can provide well-defined volumes of liquid from the bottom of the pipe, removing uncertainty surrounding the amount added and human-error in reading the syringe gradient, as well as removing the small amounts which adhere to the inner pipe wall. Analysis of the sensitivity of smaller sensors to level changes in regions outside of the sensor cavity introduced an interesting concept, where it may be possible to sense high-loss liquids without the LUT ever entering the cavity, or at least not significantly. This method would certainly constrict the measurable range of levels to a small region below the sensor, but could provide a way to sense lossy liquids while retaining a relatively high Q. Sensitivity of the fringing regions could be exploited to use the slotted cylindrical geometry as a general purpose, wireless proximity sensor which is also sensitive to the permittivity of the material under test. Any measurement which focuses on the fringing region should consider the effect of the meniscus for different liquids, where this thesis has only considered a spherical cap for all liquids. In practice the shape will change for different LUTs and pipe radii, and could have a significant impact on the measured f_r when measurements concern highly-sensitive sensors and relatively small level ranges. It may even be possible to detect differences in menisci shape for higher permittivity liquids, potentially as a method for the determination of viscosity. [1] A further simple use of the geometry is as a rotation or tilt sensor, using the distribution of a suitable liquid within the sensor cavity as a detector. With appropriate positioning of the slot, rotating the sensor about an axis perpendicular to pipe length will effectively produce similar results to a level measurement, as liquid will cover a given portion of the slot depending on the angle of rotation. Multiple sensor level sensing could benefit from further analysis as it would be interesting to investigate the limit on resolution, where the smallest detectable change in liquid level is limited by the size and separation of sensors. Similarly for the alternative method which uses different slot widths, further work could study the placement of a large number of sensors with a gradually increasing slot width.

Temperature sensing applications require a considerable amount of attention, where this thesis has merely proposed the possibility by displaying changes in the resonant frequency of the sensor over relatively small temperature ranges. A measurement of temperature effects in a more controlled environment would be essential for the assessment of the sensor as a suitable thermal sensor, where equipment capable of precisely controlling the temperature of the LUT would be required. Measuring temperature through small changes in permittivity is essentially making

---

[1] Though this may be considered a rather 'academic' venture.

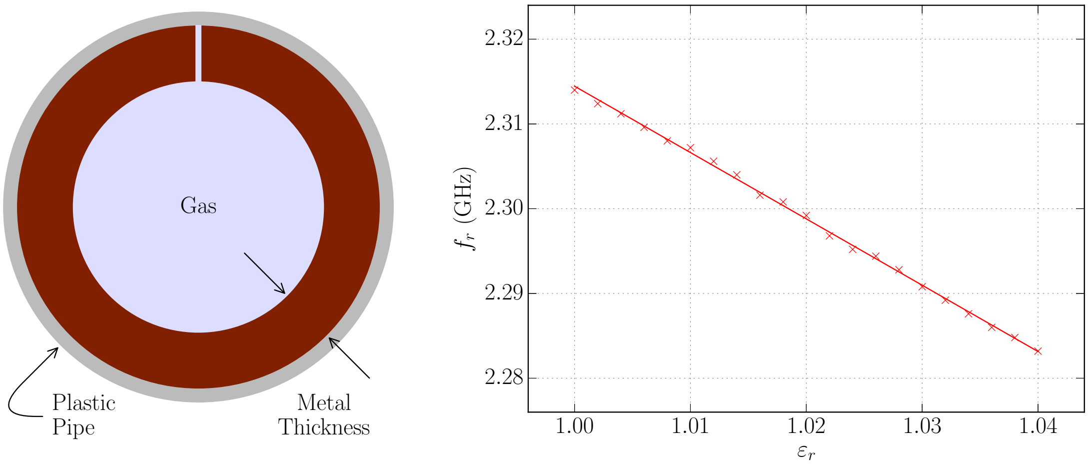

(a) Cross-section.

(b) Simulated f_r.

Figure 5.1: Cross-section of the proposed gas sensor and the simulated f_r for small values of ε_r.

use of the sensitivity of the sensor, and is reliant on the measured liquid ε_r having a suitably large temperature-dependency. There is also the possibility of exploiting the highest levels of sensitivity, which occur as permittivity approaches 1, to measure gases. Except for very high pressures, most gases feature ε_r values very close to 1, and in its current configuration, the resonant frequency of the slotted cylindrical resonator decreases by less than 10 MHz up to $\varepsilon_r = 1.1$, which would not be suitable except for very high-Q resonances. To increase sensitivity, the resonator may be placed inside of the PTFE pipe and made considerably thicker, as shown in Fig. 5.1a, where the entire region inside of the pipe is filled with gas, including between the slot faces. With these geometric changes, the simulated result of varying permittivity between 1 and 1.04 is shown in Fig. 5.1b, where it can be seen that a total change of 30.8 MHz in induced over a very small ε_r range. The change is still relatively small, but may be sufficient for the sensing of some pressurised gases provided the response is of a high enough Q-factor. Decreasing the pipe radius, slot width and slot length dimensions acts to increase Q, as well as increasing the thickness of the metal, where further study would be required to determine whether such small changes in f_r are consistently measurable in practice.

A final consideration is that of a sensor network, comprised of a number of individual or groups of sensors each independently responsible for monitoring the contents of a particular pipe. Using a central processor, such as an FPGA or microprocessor, integrated with the antenna(s), the real-time response from the entire measurement environment may be observed and analysed. It would be necessary to determine an upper limit on the number of sensors which may be monitored simultaneously using the same antenna(s), which would be impacted by a number of issues. The permittivities of the LUTs will affect the distribution of resonances in the frequency domain, where it would not be possible to monitor two liquids of very similar ε_r for example, as the system would not be able to distinguish their individual responses. This problem may be mitigated to some extent by adjusting sensor geometry to tune f_r, where the example of two LUTs of equal permittivity could be solved by increasing the slot width of one of the sensors, and decreasing the other, effectively separating the resonant peaks of each sensor despite both containing liquids of similar ε_r. Additionally, the operating bandwidth of the antenna(s) would define a hard limit on the measurable frequency range, and is an example of where actions may be taken to reduce sensor sensitivity. Finally, each pipe and its associated sensor(s) must be suitably separated from others to reduce mutual coupling effects, where at some distance from the transmitting antenna performance will be inadequate.

This thesis has presented a number of issues of consideration for future work on the topic of liquid sensing using a slotted cylindrical resonator. These may be broadly categorised as necessary steps in the development of a functional measurement system, capable of simultaneously monitoring a number of liquids, as well as level and temperature, in an industrial environment. Now that the sensor behaviour is well understood, through theory, simulation and measurement, it follows that its benefits and advantages be leveraged to solve a practical, real-world issue.

Bibliography

[1] Sensor. *Oxford English Dictionary.* Oxford University Press, 2017.

[2] N. A. Pantazis, S. A. Nikolidakis, and D. D. Vergados. Energy-efficient routing protocols in wireless sensor networks: A survey. *IEEE Communications Surveys Tutorials*, 15(2):551–591, Second 2013.

[3] P. Huang, L. Xiao, S. Soltani, M. W. Mutka, and N. Xi. The evolution of mac protocols in wireless sensor networks: A survey. *IEEE Communications Surveys Tutorials*, 15(1):101–120, First 2013.

[4] S. Li, L. D. Xu, and X. Wang. Compressed sensing signal and data acquisition in wireless sensor networks and internet of things. *IEEE Transactions on Industrial Informatics*, 9(4):2177–2186, Nov 2013.

[5] Simon Ramo, John R. Whinnery, and Theodore Van Duzer. *Fields and Waves in Communication Electronics*, chapter 1, page 8. Wiley, 1993.

[6] John D. Kraus. *Electromagnetics*, chapter 4, page 134. McGraw-Hill, 2007.

[7] John D. Kraus. *Electromagnetics*, chapter 4, page 138. McGraw-Hill, 2007.

[8] John D. Kraus. *Electromagnetics*, chapter 4, page 140. McGraw-Hill, 2007.

[9] David M. Pozar. *Microwave Engineering*, chapter 1, page 10. Wiley, 2013.

[10] Richard J. Collier. *Transmission Lines*, chapter 4, page 144. Cambridge University Press, 2013.

[11] T. Meissner and F. J. Wentz. The complex dielectric constant of pure and sea water from microwave satellite observations. *IEEE Transactions on Geoscience and Remote Sensing*, 42(9):1836–1849, Sept 2004.

[12] David M. Pozar. *Microwave Engineering*, chapter 3, page 113. Wiley, 2013.

[13] Constantine A. Balanis. *Antenna Theory*, chapter 11, pages 637–641. Wiley, 2005.

[14] Thomas L. Floyd. *Electronics Fundamentals: Circuits, Devices and Applications*, chapter 10, page 343. Merrill Publishing Company, 1987.

[15] Thomas L. Floyd. *Electronics Fundamentals: Circuits, Devices and Applications*, chapter 11, page 381. Merrill Publishing Company, 1987.

[16] David M. Pozar. *Microwave Engineering*, chapter 6, page 275. Wiley, 2013.

[17] A. P. Gregory and R. N. Clarke. A review of rf and microwave techniques for dielectric measurements on polar liquids. *IEEE Transactions on Dielectrics and Electrical Insulation*, 13(4):727–743, Aug 2006.

[18] Bob Clarke. Measurement of dielectric properties of the materials at rf and microwave frequencies. In Richard Collier and Doug Skinner, editors, *Microwave Measurements*, chapter 18, pages 439–442. The Institute of Engineering and Technology, Stevenage, 2007.

[19] L. F. Chen, C. K. Ong, C. P. Neo, V. V. Varadan, and V. K. Varadan. *Microwave Electronics: Measurement and Materials Characterization*, chapter 6, pages 256–258. Wiley, 2005.

[20] K. Saeed, R. D. Pollard, and I. C. Hunter. Substrate integrated waveguide cavity resonators for complex permittivity characterization of materials. *IEEE Transactions on Microwave Theory and Techniques*, 56(10):2340–2347, Oct 2008.

[21] D. Deslandes and K. Wu. Integrated microstrip and rectangular waveguide in planar form. *IEEE Microwave and Wireless Components Letters*, 11(2):68–70, Feb 2001.

[22] D. Deslandes. Design equations for tapered microstrip-to-substrate integrated waveguide transitions. In *2010 IEEE MTT-S International Microwave Symposium*, pages 704–707, May 2010.

[23] Y. Ding and K. Wu. Substrate integrated waveguide-to-microstrip transition in multilayer substrate. *IEEE Transactions on Microwave Theory and Techniques*, 55(12):2839–2844, Dec 2007.

[24] Z. Kordiboroujeni and J. Bornemann. New wideband transition from microstrip line to substrate integrated waveguide. *IEEE Transactions on Microwave Theory and Techniques*, 62(12):2983–2989, Dec 2014.

[25] F. Taringou, D. Dousset, J. Bornemann, and K. Wu. Substrate-integrated waveguide transitions to planar transmission-line technologies. In *2012 IEEE/MTT-S International Microwave Symposium Digest*, pages 1–3, June 2012.

[26] M. J. Hill, R. W. Ziolkowski, and J. Papapolymerou. A high-q reconfigurable planar ebg cavity resonator. *IEEE Microwave and Wireless Components Letters*, 11(6):255–257, June 2001.

[27] Y. Cassivi, L. Perregrini, K. Wu, and G. Conciauro. Low-cost and high-q millimeter-wave resonator using substrate integrated waveguide technique. In *2002 32nd European Microwave Conference*, pages 1–4, Sept 2002.

[28] H. Lobato-Morales, A. Corona-Chávez, J. L. Olvera-Cervantes, R. A. Chávez-Pérez, and José Luis. Wireless sensing of complex dielectric permittivity of liquids based on the RFID. *IEEE Transactions on Microwave Theory and Techniques*, 62(9):2160–2167, Sept 2014.

[29] J. D. Barrera and G. H. Huff. Analysis of a variable siw resonator enabled by dielectric material perturbations and applications. *IEEE Transactions on Microwave Theory and Techniques*, 61(1):225–233, Jan 2013.

[30] H. Lobato-Morales, A. Corona-Chávez, and J. L. Olvera-Cervantes. Planar sensors for rfid wireless complex-dielectric-permittivity sensing of liquids. In *2013 IEEE MTT-S International Microwave Symposium Digest (MTT)*, pages 1–3, June 2013.

[31] Humberto Lobato-Morales, Alonso Corona-Chávez, D. V. B. Murthy, and José L. Olvera-Cervantes. Complex permittivity measurements using cavity perturbation technique with substrate integrated waveguide cavities. *Review of Scientific Instruments*, 81(6):064704, June 2010.

[32] H. Lobato-Morales, D. V. B. Murthy, A. Corona-Chavez, J. L. Olvera-Cervantes, J. Martinez-Brito, and L. G. Guerrero-Ojeda. Permittivity measurements at microwave frequencies using epsilon-near-zero (enz) tunnel structure. *IEEE Transactions on Microwave Theory and Techniques*, 59(7):1863–1868, July 2011.

[33] S. Moscato, M. Pasian, M. Bozzi, L. Perregrini, R. Bahr, T. Le, and M. M. Tentzeris. Exploiting 3d printed substrate for microfluidic siw sensor. In *2015 European Microwave Conference (EuMC)*, pages 28–31, Sept 2015.

[34] G. Gennarelli, S. Romeo, M. R. Scarfi, and F. Soldovieri. A microwave resonant sensor for concentration measurements of liquid solutions. *IEEE Sensors Journal*, 13(5):1857–1864, May 2013.

[35] David M. Pozar. *Microwave Engineering*, chapter 3, page 147. Wiley, 2013.

[36] M. H. Zarifi, S. Farsinezhad, K. Shankar, and M. Daneshmand. Liquid sensing using active feedback assisted planar microwave resonator. *IEEE Microwave and Wireless Components Letters*, 25(9):621–623, Sept 2015.

[37] M. Abdolrazzaghi, M. H. Zarifi, and M. Daneshmand. Sensitivity enhancement of split ring resonator based liquid sensors. In *2016 IEEE SENSORS*, pages 1–3, Oct 2016.

[38] A. Ebrahimi, W. Withayachumnankul, S. Al-Sarawi, and D. Abbott. High-sensitivity metamaterial-inspired sensor for microfluidic dielectric characterization. *IEEE Sensors Journal*, 14(5):1345–1351, May 2014.

[39] N. Meyne, C. Cammin, and A. F. Jacob. Accuracy enhancement of a split-ring resonator liquid sensor using dielectric resonator coupling. In *2014 20th International Conference on Microwaves, Radar and Wireless Communications (MIKON)*, pages 1–4, June 2014.

[40] M. H. Zarifi and M. Daneshmand. Monitoring solid particle deposition in lossy medium using planar resonator sensor. *IEEE Sensors Journal*, 17(23):7981–7989, Dec 2017.

[41] T. Chretiennot, D. Dubuc, and K. Grenier. A microwave and microfluidic planar resonator for efficient and accurate complex permittivity characterization of aqueous solutions. *IEEE Transactions on Microwave Theory and Techniques*, 61(2):972–978, Feb 2013.

[42] D. J. Rowe, S. al Malki, A. A. Abduljabar, A. Porch, D. A. Barrow, and C. J. Allender. Improved split-ring resonator for microfluidic sensing. *IEEE Transactions on Microwave Theory and Techniques*, 62(3):689–699, March 2014.

[43] C. Arenas-Buendia, F. Gallée, A. Valero-Nogueira, and C. Person. Rf sensor based on gap waveguide technology in ltcc for liquid sensing. In *2015 9th European Conference on Antennas and Propagation (EuCAP)*, pages 1–4, May 2015.

[44] Lu Guirong and Chen Shuyue. A capacitive liquid level sensor with four electrodes. In *2010 3rd International Conference on Computer Science and Information Technology*, volume 4, pages 628–632, July 2010.

[45] C. Mariotti, W. Su, B. S. Cook, L. Roselli, and M. M. Tentzeris. Development of low cost, wireless, inkjet printed microfluidic rf systems and devices for sensing or tunable electronics. *IEEE Sensors Journal*, 15(6):3156–3163, June 2015.

[46] B. S. Cook, J. R. Cooper, and M. M. Tentzeris. An inkjet-printed microfluidic rfid-enabled platform for wireless lab-on-chip applications. *IEEE Transactions on Microwave Theory and Techniques*, 61(12):4714–4723, Dec 2013.

[47] W. Su, B. Cook, M. Tentzeris, C. Mariotti, and L. Roselli. A novel inkjet-printed microfluidic tunable coplanar patch antenna. In *2014 IEEE Antennas and Propagation Society International Symposium (APSURSI)*, pages 858–859, July 2014.

[48] Dibin Mary George, Aanandan Chandroth, C C H Ng, and P R Young. High-gain narrow-band slotted antenna based on enz siw structure. *Journal of Physics D: Applied Physics*, 51(13):135102, 2018.

[49] David M. Pozar. *Microwave Engineering*, chapter 3, page 129. Wiley, 2013.

[50] Goodfellow. Polytetrafluoroethylene (PTFE) Material Information. `http://www.goodfellow.com/E/Polytetrafluoroethylene.html`, 2018. [Online; accessed 21-March-2018].

[51] Oleksiy Sydoruk, E Tatartschuk, E Shamonina, and L Solymar. Analytical formulation for the resonant frequency of split rings. 105:014903 – 014903, 02 2009.

[52] J. B. Pendry, A. J. Holden, D. J. Robbins, and W. J. Stewart. Magnetism from conductors and enhanced nonlinear phenomena. *IEEE Transactions on Microwave Theory and Techniques*, 47(11):2075–2084, Nov 1999.

[53] R. Marques, F. Mesa, J. Martel, and F. Medina. Comparative analysis of edge- and broadside- coupled split ring resonators for metamaterial design - theory and experiments. *IEEE Transactions on Antennas and Propagation*, 51(10):2572–2581, Oct 2003.

[54] A. Radkovskaya, M. Shamonin, C. J. Stevens, G. Faulkner, D. J. Edwards, E. Shamonina, and L. Solymar. Resonant frequencies of a combination of split

rings: Experimental, analytical and numerical study. *Microwave and Optical Technology Letters*, 46(5):473–476, 2005.

[55] Simon Ramo, John R. Whinnery, and Theodore Van Duzer. *Fields and Waves in Communication Electronics*, chapter 4, pages 192–193. Wiley, 1993.

[56] J. E. Allen and S. E. Segre. The electric field in single-turn and multi-sector coils. *Il Nuovo Cimento (1955-1965)*, 21(6):980–987, Sep 1961.

[57] Constantine A. Balanis. *Antenna Theory*, chapter 2, pages 96–104. Wiley, 2005.

[58] Arthur von Hippel. *Dielectrics and Waves*, chapter II 22, page 176. Wiley, 1954.

[59] Arthur von Hippel. *Dielectrics and Waves*. Wiley, 1954.

[60] A. P. Gregory and R. N. Clarke. Tables of the complex permittivity of dielectric reference liquids at frequencies up to 5 GHz. Technical report, National Physical Laboritory, UK, 2012.

[61] Rohde & Schwarz. *R & S HL050 Log-Periodic Antenna*, August 2017.

[62] Rohde & Schwarz. *R & S ZVL Vector Network Analyzer*, July 2017. V 10.00.